UNIVERSITY OF OKLAHOMA

GRADUATE COLLEGE

CONSTRAINING THE COMPOSITION AND PHYSICS OF ACTIVE GALACTIC NUCLEI WITH COMPUTER MODELING

A DISSERTATION

SUBMITTED TO THE GRADUATE FACULTY

IN PARTIAL FULFILLMENT OF THE REQUIREMENTS FOR THE

DEGREE OF

DOCTOR OF PHILOSOPHY

By

DARRIN ALAN CASEBEER
Norman, Oklahoma
2007

UMI Number: 3261098

UMI Microform 3261098

ProQuest Information and Learning Company
300 North Zeeb Road
P.O. Box 1346
Ann Arbor, MI 48106-1346

CONSTRAINING THE COMPOSITION AND PHYSICS OF ACTIVE GALACTIC NUCLEI WITH COMPUTER MODELING

A DISSERTATION APPROVED FOR THE
HOMER L. DODGE DEPARTMENT OF PHYSICS AND ASTRONOMY

By

Karen M. Leighly, Chair

Edward Baron

David Branch

Ronald Kantowski

Susan Postawko

Acknowledgments

I would first like to thank my family: my father and mother Darwin and Linda Casebeer, my two sisters Melissa Taylor and Melinda Cornelsen, my brother Dustin Casebeer, my father in law and mother in law Ron and Pat DeCost.

In addition I would like to thank my various brothers and sisters in law for all of their support; Matt Taylor, Lance Cornelsen, Ralph and Sue Wimp, Les and Dawn Landes, and Ronnie DeCost.

I would like to thank my friend Larry Maddox for his help with the thesis template and for all kinds of other help throughout the years. Also I must include Darko Jevremovich, for his help with `PHOENIX` modeling.

I would like to thank my friends for their support over the years, Thushari Jayasekara, Aida Nava, Jim Hicks, Sebastian Bongard, Dean Richardson, Rollin Thomas and Dianna LaFerry, Justin Theissen, Myra Blaylock, Robert Meyer, Mike Engel, and others too numerous to mention here.

I would like to thank Neil Shafer-Ray for convincing me to study physics.

I would very much like to thank my Doctoral Committee: Susan Postawko, Ron Kantowski, David Branch, Eddie Baron, and Karen Leighly. Thank you for your support and advice throughout my graduate study.

Finally I would like to thank my wife Denise DeCost. Without her encouragement and support, I would have never had the courage to start, let alone finish.

Contents

List of Tables

List of Figures

Abstract

The following dissertation consists of a report of the main body of work that I have completed as a graduate student.

We present analysis from simultaneous *FUSE*, *ASCA*, and *EUVE* observations, as well as a reanalysis of archival *HST* spectra, from the extreme Narrow-line Seyfert 1 Galaxy RE 1034+39 (KUG 1031+398). RE 1034+39 has an unusually hard spectral energy distribution (SED) that peaks in the soft X-rays. Its emission lines are unusual in that they can all be modelled as a Lorentzian centered at the rest wavelength with only a small range in velocity widths. In order to investigate whether the unusual SED influences the emission line ratios and equivalent widths, we present three complementary types of photoionization analysis. The *FUSE* spectrum was particularly important because it includes the high-ionization line O VI. First, we use the photoionization code *Cloudy* and the SED developed from the coordinated observations to confirm that the emission lines are consistent with the observed hard SED. The best model parameters were an ionization parameter $\log(U) \approx -2$ and a hydrogen number density $\log(n_H) = 9.75$ [cm^{-2}]. Second, we present a Locally Optimally-emitting Cloud model. This model produced enhanced O VI as observed, but also yielded far too strong Mg II. Third, we develop a series of semi-empirical SEDs, run *Cloudy* models, and compare the results with the measured values using a figure of merit (FOM). The FOM minimum indicates similar SED and gas properties as were inferred from the one-zone model using the RE 1034+39 continuum. Furthermore, the FOM increases sharply toward softer continua, indicating that a hard SED is required by the data in the context of a one-zone model.

We present detailed radiative transfer spectral synthesis models for the Iron Low Ionization Broad Absorption Line (FeLoBAL) active galactic nuclei (AGN) FIRST J121442.3+280329

and ISO J005645.1-273816. Detailed NLTE spectral synthesis with a spherically symmetric outflow reproduces the observed spectra very well across a large wavelength range. While exact spherical symmetry is probably not required, our model fits are compelling and thus very large covering fractions are strongly implied by our results. We constrain the kinetic energy and mass in the ejecta and discuss their implications on the accretion rate. Our results support the idea that FeLoBALs may be an evolutionary stage in the development of more "ordinary" QSOs.

Chapter 1

Introduction to Dissertation

1.1 Dissertation Overview

This dissertation is divided in the following way: The first chapter provides introductory material that may be useful to the reader regarding the later chapters. The second chapter is based in its entirity on Casebeer et al. (2006), The third chapter is taken from Casebeer et al. (2007) , Finally I sum things up in chapter 4. and have provided a brief appendix.

1.2 Background and Motivation

Computer simulations can be useful to the scientist in many ways, from the calibration of instruments to physical simulations of large-scale structure in the universe. These models grow more and more sophisticated as computing power increases. Much of the work that I have done for my thesis involve the use of very sophisticated models.

The computer models which I use are specifically designed for analysis of the spectra of astronomical objects. This is typically an inversion problem. For example, one set of environmental and physical parameters is used as input to a computer model and the output of this model is compared with the reduced data from the observation. Then the input is changed and the results are compared again. This can result in the calculations of large grids of computer models to be sure that the "correct" solution is calculated, which is usually determined by the experience of the modeler or possibly by some goodness-of-fit indicator. Once the "correct" solution is calculated We can then, with some confidence, say that the input environmental and physical parameters correctly describe the observed object. The

sheer complexity of the models, and the number of models calculated may require the use of supercomputers.

The following computer models were used in this dissertation: *Cloudy*, `SYNOW`, and `PHOENIX`. *Cloudy* is a photoionization spectral emission line code which was originally developed for the study of low-density optically thin gas and has been extended to handle the higher-density gases of active galactic nuclei with, for the most part, good results. `SYNOW` is a physical model with parameterized optical depths which is very useful for line identification in outflows (primarally supernovae). `PHOENIX` is a physical model created for the analysis of higher density optically-thick gases and outflows both optically thin and thick; it has many applications from stars to supernovae. I include a brief explanation of how `PHOENIX` works in the Appendix.

In the following sections I will provide a background for each of the objects which I modeled in this dissertation.

1.3 Introduction to RE 1034+39

1.3.1 Background on Emission Lines

The broad emission lines in Active Galactic Nuclei (AGN) are powered primarily by photoionization (Osterbrock, 1989). There is copious evidence leading to this conclusion. For example, the emission lines are observed to vary in response to variations in the continuum. Also, the flux in strong lines is correlated with the continuum flux. Knowing that photoionization powers the emission lines, we can easily predict which lines will be strong. Photoionization removes electrons from hydrogen atoms; therefore, recombination products such as Lyα should be strong. The free electrons collide with ions from other elements, exciting those from abundant elements that are isoelectronic with lithium, such as C^{3+},

because the excitation potential of their first excited states is low. Many of these excited states are short-lived; the ion returns to ground state with emission of a photon which then escapes the gas, cooling it. Thus, we expect lines such as C IV λ1549 to be strong as well.

For this cooling channel to be effective, three-times ionized carbon atoms must be present in the gas. Therefore, the line emission should be governed by the photoionization parameter $U = \Phi/nc$ where Φ is the photoionizing flux, generally in units of photons $\mathrm{cm}^{-2}\,\mathrm{s}^{-1}$, and n is the gas density in units of cm^{-2}. The ionization parameter is the ratio between the photon density, which drives photoionization, and the gas density, which controls recombination. Thus, since C IV being strong implies the presence of C^{3+} in the gas, it also implies a particular value or range of values for the ionization parameter (more specifically, the ratios of Lyα to C IV and of C IV to C III). A typical value of the ionization parameter inferred is around $\log(U) = -1.5$ (Kwan & Krolik, 1981).

But does the presence of C IV really imply a particular ionization parameter? Perhaps it really is telling us that gas with a range of ionization parameters, corresponding to a range of photon fluxes and densities, is present, but gas with the ionization parameter suitable for C IV production happens to emit most efficiently, due to the easy excitation of the C^{3+} ion. This would cause the integrated line emission to be weighted toward gas with copious C^{3+} present, but would not preclude the presence of less effectively-emitting gas. These ideas were proposed by Baldwin et al. (1995) as the Locally Optimally-emitting Cloud model.

This simple conceptual picture of photoionization in AGN provides a zeroth-order understanding of why the line emission is similar in all objects, and why the same strong lines are usually seen. However, there are some significant trends in the emission line properties that cannot be explained directly using this zeroth-order understanding. Furthermore, there are numerous examples of objects or classes of objects whose emission lines differ from that

of the average quasar. These trends and the presence of classes of unusual objects require more sophisticated models than the zeroth-order picture presented above. This is a good thing; there are many fundamental things we don't know about the broad-line region even after years of study, including the geometry, the dynamics of the gas, and the origin of the gas. With such a large number of potentially variable parameters, our task may seem hopeless. That is far from the case, and in fact, the potential for solving this problem is orders of magnitude higher than it was when the first models were being developed due to the availability of powerful computers, increasingly-sophisticated models, and large samples of high-quality spectra from, e.g., the Sloan Digital Sky Survey.

1.3.2 Spectral Energy Distribution

One of the factors that may affect the emission lines in AGN is the shape of the spectral energy distribution (SED). AGN are known to have broad spectral energy distributions, with almost equal power emitted per logarithmic frequency range between the infrared and X-ray bands (Peterson, 1997). Their emission lines are powered largely by the bandpass from $\sim$ 4 eV through the soft X-rays, although the regions of the spectrum outside this range can contribute through heating. This part of the spectral energy distribution is thought to be primarily the emission of the accretion disk, with the higher energies above $\sim$ 1 keV or so emitted by a Comptonizing corona. Theoretically, the continuum emitted by the accretion disk should depend on the mass and accretion rate (Frank et al., 2002; Ross et al., 1992) the accretion disk geometry (Zdziarski & Gierliński, 2004), and inclination (Laor & Netzer, 1989; Puchnarewicz et al., 2001). In the simplest thin disk models, accretion onto smaller black holes, and accretion at a higher rate relative to the Eddington value predicts hotter disks (Shakura & Sunyaev, 1973), and correspondingly overall harder

spectral energy distributions. The X-ray emission arising from Comptonization by a hot optically-thin component may also be affected by the accretion rate as the power for the hot component must ultimately come from accretion. In some models, all of the accretion energy is deposited initially into the corona and then a fraction is reprocessed by the disk (Svensson & Zdziarski, 1994). Other models propose an accretion/evaporation scenario in which the disk and corona are coupled (Różańska & Czerny, 2000a,b). In these models, the amount of emission from the corona relative to that from the disk depends on the accretion rate relative to the Eddington value, with the coronal emission becoming less important at high accretion rates (Bechtold et al., 2003). In addition, at very low accretion rates, the accretion should have a different geometry (Ho, 2003); a hot, optically-thin thermal plasma may dominate the inner region, producing a much different spectral energy distribution that lacks a big blue bump.

Thus, there is a clear theoretical expectation that the spectral energy distributions in AGN should take on a range of shapes. What is the observational evidence that such a range exists? First, it is worth noting that there are difficulties in measuring the intrinsic spectral energy distribution. Since AGN vary at all wavelengths, observations in different wavebands should in principle be at least contemporaneous. Absorption and reddening in the host galaxy or in the AGN itself poses another serious complication. Finally, because of absorption, the portion of the observed-frame spectrum between 13.6 and ~ 100 eV cannot be observed at all.

Nevertheless, there is some solid evidence AGN are not characterized by a single spectral energy distribution; a range in shapes exists. For example, studies of samples of objects shows a range of SEDs (Elvis et al., 1994). In addition, α_{ox}, the point-to-point slope between 2500Å and 2 keV, has been repeatedly observed to depend on the UV luminosity

(Wilkes et al., 1994; Bechtold et al., 2003; Vignali et al., 2003). Among objects in a sample of soft X-ray selected AGNs, a correlation between the optical/UV continuum slope and the X-ray photon index has been found, such that objects with bluer optical continua have steeper X-ray spectra (Grupe et al., 1998). Also, a *FUSE* composite spectrum is observed to be harder than an *HST* composite over the same rest bandpass; as the *FUSE* spectra are from relatively lower luminosity objects, this result is attributed to luminosity-dependent evolution of the spectral energy distribution (Scott et al., 2004).

Indirect evidence for a range of spectral energy distributions among AGNs is provided by the observation that the ratio of optical depth of He II Lyα to that H I Lyα in the era of He II reionization fluctuates on small redshift scales. This is inferred to be caused by the response of these ions to a range in continuum shapes due to the difference in ionization potentials (Shull et al., 2004). However, at least part of this range in continua may certainly be caused by reddening/absorption.

Emission lines in AGNs, while broadly similar, clearly show trends and dependencies that are plausibly dependent on the spectral energy distribution. The first trend discovered was the Baldwin effect, which is the empirical inverse relationship of emission line (e.g., C IV) equivalent width with luminosity (Baldwin et al., 1977; Osmer & Shields, 1999). Initially, several models were proposed for this effect. For example, Mushotzky & Ferland (1984) posited a luminosity-dependent ionization parameter; a luminosity-dependent covering fraction was also thought to be possibly important. More recently, observational evidence has been repeatedly found that the slope of the Baldwin effect is steeper for high-ionization lines than for low-ionization lines (Osmer et al., 1994; Green, 1996; Espey & Andreadis, 1999; Wilkes et al., 1999; Green et al., 2001b; Dietrich et al., 2002; Shang et al., 2003; Warner et al., 2004). This is interpreted appealingly as evidence that, as the luminos-

ity increases, the spectral energy distribution softens, resulting in a more rapid decrease in the highest ionization lines. Further evidence supporting this view comes from observed correlations between continuum shape indicators such as α_{ox} and line equivalent width (Zheng et al., 1995; Wang et al., 1998; Green, 1998; Wilkes et al., 1999; Scott et al., 2004). Thus, it appears that the Baldwin effect is a phenomenon that depends principally on the shape of the spectral energy distribution, and its corresponding dependence on luminosity.

Interestingly, it has been found that Narrow-line Seyfert 1 galaxies show a Baldwin effect that is offset from that shown by other Seyferts and quasars (Wilkes et al., 1999; Leighly & Moore, 2004, 2006). This might be related to the fact that the cores of the lines show a stronger Baldwin effect than the wings of the lines (Osmer et al., 1994; Shang et al., 2003; Warner et al., 2004). It is possibly an indication of a different BLR geometry for this class of objects (Leighly, 2004a).

Theoretical confirmation of this model for the Baldwin effect is promising but not yet completely firm. Korista et al. (1998) use an LOC model and find that the slope dependence of the data is consistent with an evolving spectral energy distribution. On the other hand, Korista et al. (1997b) show that there may be difficulties explaining the strength of the He II line using continua developed from composite spectra.

The second important trend for line emission in AGN is the Eigenvector 1 dependence. Boroson & Green (1992), in a principle components study of spectra from PG quasars, discovered that much of the variance among optical emission lines is correlated such that narrow lines are associated with strong Fe II and weak [O III] emission. Later work shows a relationship with the steepness of the X-ray spectrum (Brandt & Boller, 1999), and an extension to the UV spectra (Wills et al., 1999). The physical driver for Eigenvector 1 is thought to be the accretion rate relative to Eddington (Leighly & Moore, 2004). Precisely

how this works has not been yet clearly delineated, but it could be mediated by the spectral energy distribution. For example, Wandel & Boller (1998) propose that the steeper soft X-ray spectrum seen in NLS1s translates to a more powerful extreme UV excess that would cause the emission lines to originate from a larger radius where velocities are smaller. Kuraszkiewicz et al. (2000) attribute the characteristic UV emission line ratios to higher densities in the broad-line region. They examine a two-phase BLR model, and suggest that the higher densities arise naturally in this model due to the hotter big blue bumps. Wills et al. (1999) infer high densities in the BLR as well, from the Si III]/C III] ratio. However, as shown in §2.7.3, this ratio can depend on the spectral energy distribution, because in some regions of the U–SED-shape parameter space, Si III] will dominate the cooling.

The spectral energy distribution can influence the line properties in another way. Leighly & Moore (2004) and Leighly (2004a) show that in a sample of Narrow-line Seyfert 1 galaxies, the degree of blueshift of C IV is correlated with α_{ox}, such that objects that are relatively weak in X-rays have more highly blueshifted lines. This makes perfect sense in the context of radiative-line driven wind models (Proga et al., 2000), because the way that the UV and X-rays play competing roles in the formation of such winds. Specifically, the UV accelerates the wind, while the X-rays tend to impede the wind because they can overionize it, destroying the ions that scatter the UV emission. So, even though objects with relatively strong X-rays can have winds, due to self-shielding, or preabsorption of soft X-rays before reaching the wind gas (Murray et al., 1995; Proga & Kallman, 2004), objects with relatively strong UV emission and weak X-ray emission will always drive faster, more massive winds.

Leighly (2004a) also notes that the spectral energy distribution can influence the strengths of the emission lines indirectly via the wind. It has long been suspected that low- and intermediate-ionization lines are produced in a different region than high-ionization lines.

The evidence for this comes from modeling of the line emission (Collin-Souffrin et al., 1982, 1988; Wills et al., 1985), and from the difference in profiles (Collin-Souffrin et al., 1988; Baldwin, 1997). One of the puzzling features in quasar spectra is the observed trend for objects with strong high-ionization line emission such as N V to have strong low-ionization line emission such as Si II (Wills et al., 1999). Leighly (2004a) show that low-ionization line emission can be enhanced if the continuum illuminating that emission region is first filtered through the wind. Such a continuum is deficient in helium-continuum photons, as they are all absorbed by the wind, and thus can only excite relatively low-ionization species.

1.4 A Self-Consistent NLTE-Spectra Synthesis Model of FeLoBAL QSOs

Spectroscopic observations of quasars show that about 10–20% have broad absorption troughs in their rest-frame UV spectra (Trump et al., 2006). These absorption lines are almost exclusively blueshifted from the rest wavelength of the associated atomic transition, indicating the presence of an outflowing wind in our line of sight to the nucleus. The line-of-sight velocities range from zero to up to tens of thousands of kilometers per second (e.g., Narayanan et al., 2004).

While understanding these outflows is of fundamental interest for understanding the quasar central engine, it is also potentially important for understanding the role of quasars in the Universe. The observation that the black hole mass is correlated with the velocity dispersion of stars in the host galaxy bulge (e.g., Magorrian et al., 1998; Ferrarese & Merritt, 2000; Gebhardt et al., 2000) indicates a co-evolution of the galaxy and its central black hole. The close co-evolution implies there must be feedback between the quasar and the

host galaxy, even though the sphere of gravitational influence of the black hole is much smaller than the galaxy. Energy arguments, however, show that is quite feasible that the black hole can influence the galaxy; as discussed by Begelman (2003), the accretion energy of the black hole easily exceeds the binding energy of the host galaxy's bulge.

The nature of the feedback mechanism that carries the accretion energy to the galaxy is not known. Since AGNs are observed to release matter and kinetic energy into their environment via outflows, it is plausible that these outflows contribute to the feedback in an important way. One of the difficulties in using quasar outflows in this context is that they are sufficiently poorly understood that there are significant uncertainties in such basic properties as the total mass outflow rate and the total kinetic energy.

What is the kinetic luminosity of the broad absorption line quasar winds? That turns out to be very difficult to constrain. While the presence of the blueshifted absorption lines unequivocally indicates the presence of high-velocity outflowing gas, the other fundamentally important properties of the gas, including the density, column density, and covering fraction are very difficult to constrain.

The density is difficult to constrain because the absorption lines are predominately resonance transitions, and their strengths are not very sensitive to density. Without knowing the density, the distance of the gas from the central engine cannot be constrained; the same ionization state can be attained by dense gas close to the central engine, or rare gas far from the central engine. Density estimates are possible when absorption lines are seen from non-resonance transitions, but even then, they can differ enormously. For example, de Kool et al. (2001) analyzed metastable Fe II absorption lines in FBQS 0840+3633, and inferred a electron density $< 1000 - 3000\,\mathrm{cm}^{-3}$ and a distance from the central engine of several hundred pc. In contrast, Eracleous et al. (2003) analyze the metastable Fe II absorption

in Arp 102B with photonionization models and infer a density of at least $10^{11}\,\mathrm{cm}^{-3}$ and a distance of less than $7 \times 10^{16}\,\mathrm{cm}$.

The global covering fraction is also difficult to constrain directly from the quasar spectrum; we know the gas, at least, partially covers our line of sight, but we have little information about other lines of sight. Covering fraction constraints are generally made based on population statistics. In a seminal paper, Weymann et al. (1991) showed that for most BALQSOs, the emission line properties are remarkably similar to non-BALQSOs. Thus, the fact that 10–20% of quasar spectra contain broad absorption lines is interpreted as evidence that there is a wind that covers 10–20% of sight lines to all similar quasars, and whether or not we see absorption lines depends on our orientation. Alternatively, some BAL quasars have notably different line emission than the average quasar; examples are the low-ionization BALQSOs studied by e.g., Boroson & Meyers (1992). These objects may instead show an evolutionary stage of quasars, as the quasar emerges from the cloud of gas and dust in which it formed (Becker et al., 1997).

While it seems that the column density should be easy to constrain, more recent work has shown that it can be very difficult to measure. It was originally thought that non-black absorption troughs indicated a relatively low column density for the absorbing gas (equivalent hydrogen column densities of $10^{19-20}\,\mathrm{cm}^{-2}$, e.g., Hamann, 1998). But it has now been found that the non-black troughs indicate velocity-dependent partial covering, where the absorption covers part of the emission region, and the uncovered part fills in the trough partially (e.g., Arav et al., 1999). Thus, the column density appears to be high, but it is very difficult to constrain directly from the data except in a few very specialized cases (see for example Gabel et al., 2006; Arav et al., 2005).

How can we make progress on this problem? It is becoming clear that because of the

difficulties described above, the traditional techniques for analysis of troughs (e.g., curve of growth) and modeling (e.g., photoionization modeling to produce absorption line ratios and equivalent widths) are limited. An approach that may be profitable is to construct a physical model for the outflow, and constrain the parameters of the model using the data.

Our first foray into constructing physical models for quasar winds was performed by Branch et al. (2002). In that paper, the FeLoBAL[1] FIRST J121442+280329 was modeled using SYNOW, a parameterized, spherically-symmetric, resonant-scattering, synthetic spectrum code more typically used to model supernovae (Fisher, 2000). The difference between this treatment and a more typical one applied to the same data by de Kool et al. (2002) is that SYNOW assumes that emission and absorption are produced in the same outflowing gas. In contrast, the approach taken by de Kool et al. (2002) assumes that absorption is imprinted upon a typical continuum+emission line quasar spectrum; that is, the absorbing gas is separated from the emission-line region. In fact, based on the analysis of the Fe II metastable absorption lines, they find that the absorber is 1–30 parsecs from the central engine, much farther than the quasar broad emission-line region. Note that FIRST J121442+280329 is not the only object that can be modeled using SYNOW; Casebeer et al. (2004) present a SYNOW model of another FeLoBAL, ISO J005645.1−273816.

The SYNOW model is attractive because it is simple; only one component is needed to model both the emission and absorption lines. However, this model is limited. The primary purpose of the SYNOW program is to identify lines in complicated supernova spectra. Thus, individual ions can be added to a SYNOW run at will in order to see if features from emission and absorption from those ions is present. It does not solve the physics of the gas,

[1]FeLoBALs are distinguished by the presence of absorption in low-ionization lines such as Al III and Mg II as well as absorption by excited states of Fe II and Fe III.

so physical parameters beyond the existence of a particular species and its velocity extent, cannot be extracted from the results.

Chapter 2

FUSE Observation of the Narrow Line Seyfert 1 Galaxy RE 1034+39: Dependence of Broad Emission Line Strengths on the Shape of the Photoionizing Spectrum

2.1 Introduction

In this installment, we present an analysis of spectra from a Narrow-line Seyfert 1 galaxy RE 1034+39 ($z = 0.043$). This object is well known for its unusual spectral energy distribution. Puchnarewicz et al. (1995, 1998, 2001) have reported optical, UV and X-ray observations of this object. While the optical and UV spectra of the typical AGN rises toward the blue, forming the big blue bump, RE 1034+39's optical/UV spectrum is rather red. The big blue bump appears instead in the X-ray spectrum: it appears to peak at $\sim 100\,\mathrm{keV}$, and the high energy turnover toward long wavelengths appears to be in the soft X-rays (Puchnarewicz et al., 1995). This unusual spectral energy distribution was confirmed by the *BeppoSAX* observation conducted in 1997 and reported by Puchnarewicz et al. (2001). The unusual spectral energy distribution has been modeled as an edge-on accretion disk (Puchnarewicz et al., 2001) and as an irradiated accretion disk (Soria & Puchnarewicz, 2002).

Given RE 1034+39's hard spectral energy distribution, one might expect that there would be strong high-ionization line emission in its UV spectrum, assuming that the line emitting gas sees the same continuum that we do. To test this hypothesis, we obtained a *FUSE* observation of RE 1034+39, along with coordinated *EUVE* and *ASCA* X-ray observations. We present the analysis of these spectra here, as well as a reanalysis of the archival

HST spectrum (§2.2). In the next three sections, we present three complementary types of photoionization analysis. First, using the spectral energy distribution constructed from the coordinated observations, we ran *Cloudy* (Ferland, 2000b) photoionization models to determine the conditions of the line emitting region, and ascertain whether the line equivalent widths and ratios are consistent with the extreme spectral energy distribution for a single-zone model (§2.3). We then look at how well the lines could be modeled in the LOC scenario (§2.4). Third, we consider a range of semi-empirical spectral energy distributions presented in (§2.7) , and compare the predicted line emission as a function of SED (and other parameters) with that of RE 1034+39 (§2.5). We discuss the results in §2.6, and present auxiliary material in §2.7.

2.2 Multiwavelength Observations and Data Analysis

2.2.1 *FUSE* Observation

The *Far Ultraviolet Spectroscopic Explorer (FUSE)* [1] was launched 1999 June 24. *FUSE* provides unprecedented sensitivity and resolution over the 905–1187Å bandpass, which contains rest wavelength transitions from many important atoms and molecules (Moos et al., 2000; Sahnow et al., 2000). The *FUSE* observation of RE 1034+39, coordinated with observations using *ASCA* and *EUVE*, was approved as part of the Cycle 1 Guest Investigator observing program.

The observing log for the *FUSE* observation is given in Table 2.1. The raw *FUSE* data were downloaded and reprocessed. At the time that the analysis was done, CALFUSE v2.0 had not yet been released, and the Beta version was not fully functional; therefore, we used CALFUSE v1.8.7 with some enhancements from v2.0 as described below. We

[1] http://fuse.pha.jhu.edu/

recently re-ran the pipeline using CALFUSE v2.4 and confirmed that the resulting spectra are indistinguishable from the ones that are presented here. RE 1034+39 is a faint object for *FUSE*; therefore, we used only the data obtained during the time that *FUSE* spent in the earth's shadow. To reduce the background, we only used data within PHA channels 4–16 (Brotherton et al., 2002). This choice approximately halved the value of the constant background component, but decreased the source flux by only $\sim 5\%$.

CALFUSE v1.8.7 approximated the background using a uniform image; however, the real detector background has considerable structure. In CALFUSE v2.0 and subsequent versions, this is accounted for by using real images of the background. In order to utilize this improvement in CALFUSE v1.8.7, we extracted the night-time background image from the v2.0 calibration files and used it instead of the v1.8.7 background image. We then ran the pipeline again. We adjusted the scaling and offset of the background image to the background level of the observation. To do this, we extracted spectra from two source-free regions of the detector in the observed image and the background image. A linear regression between the background and source vectors produced the scale and offset necessary to match the background file to the data. The background was suitably scaled and offset, and the pipeline script modified to use this background image.

We examined the two-dimensional images after background subtraction. The spectral trace was clearly visible for all telescope systems except SiC2. We take this as evidence that the image of the galaxy was not in the the slit for this telescope system, and we do not consider it further. The background subtraction appeared to be successful for most of the telescope/detector segments; however, we were unable to obtain a satisfactory background subtraction for the LiF2b spectrum, and we do not consider it further. The SiC1a spectrum was not used in the composite spectrum, due to low signal-to-noise ratio compared to the

LiF1a spectrum which samples the same wavelength interval.

We examined the flux calibration between overlapping detector segments. The most noticeable difference was between LiF2a and LiF1b segments longward of 1140 Å. We expect that this difference may be due to the "worm" or shadowing of the detector by the grid wires above it in LiF1b. Therefore, we exclude data longward of 1140 Å for that segment, and average the two segments over the remainder of the overlapping interval.

Wavelength calibration V10 was used. The remaining spectra (LiF1a, combined LiF1b and LiF2a, SiC1b) were rebinned using an algorithm similar to the IRAF `trebin` script. The spectra were then concatenated, and the result is shown in Fig. 2.1, after having corrected for the redshift (z = 0.043), and Galactic reddening $E(B-V) = 0.015$ mag, estimated from the infrared cirrus (Schlegel et al., 1998a) , using the Cardelli et al. (1989) reddening curve.

Uncertainties in spectra are rarely shown for *FUSE* spectra of AGN (Shang et al., 2005; Romano et al., 2002). This is possibly because the error column in the pipeline spectra aren't very useful; the spectra contain only several photons per bin at full wavelength resolution. However, uncertainties on the spectra are useful to have for faint objects such as AGN, so we developed a method to evaluate them. First, we ran the pipeline, outputting the intermediate products which include the "total" image (*_img.fit*) and the scaled background image (*_bkgd.fit*). The spectra at full wavelength resolution were extracted from these images using the nominal extraction regions (calibration files *spex1a009.fit*, etc) and collapsing in the y direction. The wavelength scale was obtained from the pipeline output spectrum. The total counts spectrum and background counts spectrum were rebinned to the desired binsize (in this case, 0.5Å) by summing the counts within each bin. Then the error counts spectrum was obtained by propagation of errors assuming Poisson statistics in each bin of the rebinned total and background spectra. The error spectrum was then "fluxed" using the

appropriate calibration flux file (calibration files *flux1a008.fit*, etc.). The error spectrum is shown by the thick line in Fig. 2.1. This shows that no continuum flux was detected below ~ 960Å where only the SiC1b spectrum is available.

The shorter wavelength component of the O VI λ1034 doublet (1031.93Å) is clearly detected, but the longer wavelength component (1037.62Å) is absent (Fig. 2.1). We suspect that the longer wavelength component does not appear because of residual background subtraction problems. Fig. 2.2 shows a section of the 2D LIF1 image after screening and before background subtraction. The spectral trace is clearly seen, and an enhancement corresponding to the 1037Å component is apparent. Fig. 2.2 also shows that the background is higher near the edge of the detector; the effective area is lower as well. Thus it proved to be impossible to tease the longer wavelength component of O VI from the noise. We note that there is an enhancement in the low signal-to-noise ratio Sic1a spectrum at 1037Å (shown as an inset in Fig. 2.1). Therefore, we base our analysis on the 1032Å component.

C III λ977 was also detected, as well as Lyβ (see Section 2.6); however, N III and He II, low equivalent width lines sometimes seen in other FUV spectra from AGN (e.g. Brotherton et al., 2002; Hamann et al., 1998) are were not detected.

2.2.2 *ASCA* Observation

An *ASCA* observation was conducted simultaneously with the *FUSE* observation (Table 2.1). A standard configuration was used during the observation. The GISs were operated in PH mode throughout the observation. The SISs were operated in 1 CCD Faint and Bright mode at high and medium bit rate, respectively. The SIS energy gain was reprocessed using the latest calibration file (sisph2pi_290301.fits).

We used the same criteria as the rev 2 standard processing for our data selection [2]

[2]http://adfwww.gsfc.nasa.gov/asca/processing_doc/proc/rev2/la test/screen.html

, except for the ANG_DIST (angular distance from the nominal pointing) criterion. The pointing accuracy was poor during this observation; therefore, we used a looser angular distance selection criterion. The sensitivity change due to the pointing error of 1.0 arcmin is about 10%; this is accounted for in the spectral fitting by the ancillary response file.

The source was detected at R.A.= $10^{\rm h}34^{\rm m}36^{\rm s}$ and Decl.= $39^\circ38'56"$ (equinox 2000.0) in good agreement with the optical position within the *ASCA* position accuracy of $\sim 1'$. We accumulated the source photons from the circular regions centered on the source with radii of 4.0, 3.5 and 6.0 arcmin for the SIS-0, SIS-1 and GISs, respectively. The background data were accumulated from source-free regions on the detector. The average count rates from the source regions are 0.096 c s^{-1} and 0.059 c s^{-1}, and the background fractions are estimated to be ∼13% and ∼33% for each SIS and GIS, respectively.

We fitted each of the four spectra separately with a model consisting of a power-law with Galactic absorption ($N_H = 1.43 \times 10^{20}\,{\rm cm}^{-2}$; Murphy et al. 1996) in the whole energy band. The statistics were rather poor in this short observation; thus, this model is not rejected at 90% confidence level for any of the spectra. Then, we added a blackbody to the model to represent the soft excess component commonly seen in NLS1 spectra, and previously seen in this object (Pounds et al., 1995; Leighly, 1999). The fits were acceptable for all four spectra and χ^2 values were improved significantly (F-test confidence levels of 99 and 97% for SISs and GISs, respectively). All parameters are consistent among the four detectors. We also confirmed that the results from the faint and bright mode are consistent with those only from the faint mode data (which have better energy resolution). Finally we fit the SISs and GISs data simultaneously with a model of a power-law plus a black body attenuated by Galactic absorption. The best-fit parameters are summarized in Table 2.2.

The divergence of the SIS spectra at low energies has been reported, especially for

observations performed near the end of the mission. An empirical correction for this has been proposed by Yaqoob et al. (2000) [3] . We applied this correction by introducing a fixed neutral absorption $N_H = 7.3 \times 10^{20}\,\mathrm{cm}^{-2}$, appropriate for the date of this observation, and discarding the SIS-1 data below 1 keV. The best-fit parameters from this fit are also listed in Table 2.3.

2.2.3 *EUVE* Observation

An EUVE observation was conducted simultaneously with the *ASCA* and *FUSE* observations (Table 2.1). A description of the standard reduction for the *EUVE* Deep Survey Instrument is given in Halpern et al. (2003). RE 1034+39 is a reasonably bright target for *EUVE*. However, the observation was conducted during Solar Maximum, which strongly enhanced the background and resulted in noisy data. While the resulting light curve was formally significantly variable (χ^2_R for a constant hypothesis was 1.99 for 53 degrees of freedom), we believe that the origin of the variability may be less-than-perfect background subtraction. We note that the average count rate observed ($0.036\,\mathrm{count\,s}^{-1}$) during the coordinated observation is consistent with the rate observed ($0.037\,\mathrm{count\,s}^{-1}$) during a quieter period three years earlier and is therefore consistent with the general lack of variability in this object (Puchnarewicz et al., 2001).

We use PIMMS (Portable, Interactive Multi-Mission Simulator; Mukai 1993) to estimate the flux. We assume that the spectrum is a power law with Galactic absorption of $N_H = 1.43 \times 10^{20}\,\mathrm{cm}^{-2}$. For a range of photon indices between 2.5–4.5, we predict an intrinsic flux at 0.15 keV observed frame of between 0.75–0.83 $\mathrm{photons\,cm}^{-2}\,\mathrm{s}^{-1}\,\mathrm{keV}^{-1}$.

[3] http://heasarc.gsfc.nasa.gov/docs/asca/calibration/nhparam.html

2.2.4 Archival *HST* FOS spectra

Our proposal for coordinated *HST* observations was not successful, so we analyzed the archival data from this object, previously presented by (Puchnarewicz et al., 1998). We applied the most up-to-date calibration to the archival data. We used the Galactic absorption lines to check the wavelength calibration of the spectra and shifted them appropriately.

The *HST* data were obtained more than three years before the *FUSE* observations. Thus, variability between the observations was a concern; are we justified in using these archival data? We believe that we are, for two reasons. First, the *FUSE* and *HST* continua are separated by a gap of less than 20 Å, and the *FUSE* continuum appears to be consistent with an extrapolation of the *HST* continuum. Second, RE 1034+39 is well known for its general lack of variability (Puchnarewicz et al., 2001).

2.2.5 Analysis of the Emission Lines

In this section, we describe our extraction of the emission line parameters from the spectra, and discuss some features of the results. The spectra were fitted using the `Specfit` module in IRAF (Kriss, 1994). The results are given in Table 2.3 and Fig. 2.3.

Puchnarewicz et al. (1998) found no evidence for intrinsic absorption lines in the *HST* spectra; our reanalysis did not uncover any either. The high resolution and good sensitivity obtained in the *FUSE* spectrum revealed a number of weak absorption features on O VI (Fig. 2.4). The wavelengths of all of these features were consistent with Galactic molecular hydrogen absorption. Thus, we find no evidence for intrinsic O VI absorption in RE 1034+39.

Preliminary examination showed that the spectra consisted of a smooth continuum and narrow lines that are generally not strongly blended. Also, RE 1034+39 lacks the

strong Fe II multiplets frequently found in Narrow Line Seyfert 1 galaxies that can interfere with spectral fitting. Therefore, we modeled the continuum locally using a linear function around each line or blend. The line profile of the permitted and semi-forbidden lines could be modeled well with a Lorentzian profile and there appeared to be little evidence for a difference in shape between the high and low-ionization lines such as has been observed in some Narrow Line Seyfert 1 galaxies (e.g. Leighly & Moore, 2004). In fact, we found that we could obtain an acceptable fit if the wavelength of each line were fixed to the laboratory wavelength, allowing only the width and flux to vary. Widths of doublets and multiplets were constrained to be equal. Doublet and multiplet intensities of some lines were constrained as follows. The relative line intensities for O IV λ1402 multiplet were constrained using the treatment described by Nussbaumer & Storey (1982). Lines emitted from the same upper levels depend only on relative transition probabilities; this is the case for the λ1399.77 and λ1407.39 lines where a ratio of 1 was calculated, the λ1397.20 and λ1404.81 lines where a ratio of 0.13 was calculated. The density dependent components of O IV λ1402 were taken from Nussbaumer & Storey (1982). The emission line features are consistent with a density of $n_H = 10^{10}\,\mathrm{cm}^{-3}$ given a temperature of the gas of $1.5 \times 10^5 K$. We point out however that this feature is very weak and blended, and we cannot use it to constrain the density of the emitting gas.

Fig. 2.3 demonstrates that our assumption that the line profile is uniformly Lorentzian is well justified, in most cases. There are a few discrepancies. As discussed in Section 2.1, the O VI line is near the edge of the Lif1a detector, so that the only the 1032Å component is measured. We also found that the blue component is weaker than the red component of the Mg II doublet. This is not expected physically, because the statistical weight of the blue component is twice that of the red component. We investigated the possibility that the

profile was affected by bad diodes or Galactic absorption lines, but were unable to find the reason for this discrepancy. Also, we found that the He II λ1640 line displays a blue wing; this was also reported by Puchnarewicz et al. (1998). This is the only line in the spectrum that displays such a feature. It is possible that it originates in recombination in optically thin, highly ionized gas.

In Fig. 2.5, we plot the velocity width of the brighter ($F_\lambda > 1.5 \times 10^{-14}\,\mathrm{erg\,cm^{-2}\,s^{-1}}$ for the multiplet), and least-blended emission lines as a function of their ionization potential (O VI, Lyα, N V, C IV, Si III], C III], Mg II). We find that most of the higher-ionization lines have slightly larger velocity widths than lower-ionization lines. Such trends have been seen before (Baldwin, 1997), and they are consistent with our understanding based on reverberation mapping results (Peterson, 1997) that the broad-line region is typically radially stratified. The exception is He II. This line is different than the other high-ionization lines in that it has a blue wing; it is possible that deblending the blue wing artificially narrowed the line core. RE 1034+39 is unusual in that the line profiles have the same shape and are all centered at their rest wavelength; in other objects, high ionization lines are not only broader but sometimes strongly blueshifted (Leighly & Moore, 2004). RE 1034+39 is also unusual in that the range of velocity widths of lines of different ionization is small.

The measured equivalent width of the 1031.9Å component of the O VI line is 29Å. As noted in §2.2.1, we could not measure the 1037.6 Å component because of high background. If we assume that the gas is very optically thick, these two emission lines will have the same equivalent width, and the equivalent width of the doublet would be 58Å. Alternatively, in the optically thin regime, the 1037.6 Å component should have half the flux of the 1031.9Å component, and the total equivalent width would be 43Å. In either case, given the low luminosity of $\log L_{2500} = 28.3$ [$\mathrm{ergs\,s^{-1}}$], we find that it is roughly consistent with the O VI

Baldwin effect presented by Kriss (2001).

In Table 2.4, we present a comparison of the bright emission line fluxes with that of Lyα for RE 1034+39 and the same quantities obtained from three composite spectra: the LBQS composite (Francis et al., 1991a) , the radio-quiet composite from *HST* spectra (Zheng et al., 1997) , and a composite spectrum from the FIRST Bright Quasar Survey (Brotherton et al., 2001). We find that the biggest difference is in the measurement of O VI: the value from RE 1034+39 is much larger with respect to Lyα than from any of the other composites. It should be noted, however, that the LBQS and FIRST composites are made with observed-frame optical spectra, where Lyα forest absorption could reduce the flux of O VI. However, this does not explain the difference with respect to the *HST* composite. RE 1034+39 also has stronger He II and weaker Mg II than the composites.

2.2.6 The Spectral Energy Distribution of RE 1034+39

The spectral energy distribution (SED) of RE 1034+39 constructed from the *HST*, *FUSE*, *EUVE* and *ASCA* data is shown in Fig. 2.6. For comparison, we show the *Cloudy* AGN continuum. The strong soft excess peaking in the EUV first reported by Puchnarewicz et al. (1995) is clearly seen.

The shape of the SED is frequently roughly parameterized by α_{ox}, the point-to-point power law slope between 2500 Å and $\sim 2\,\mathrm{keV}$. We infer $\alpha_{ox} = 1.22$ for RE 1034+39. Wilkes et al. (1994) find that this parameter is correlated with the log of the luminosity at 2500 Å. For an object with $\log_{10}(l_{opt}) = 28.3$ (for $H_0 = 50$, $\Lambda_0 = 0$), their regression predicts $\alpha_{ox} = 1.29$. It should be noted that there are only 5 objects with lower optical luminosity than RE 1034+39 in the Wilkes et al. sample; these objects cluster around $\log L_{2500} \approx 28$, and their α_{ox}'s are ~ 1.6. This suggests that RE 1034+39 has a markedly flat α_{ox} compared

with other AGN of its luminosity.

Puchnarewicz et al. (1995) reported that the optical/UV continuum could be described by a power law [4] with index $\alpha_{opt} \sim 0.9$. This is somewhat steeper than that of the typical quasar (0.33 with rms dispersion of 0.59; Natali et al. 1998). Our reanalysis of the *HST* spectra, in combination with the *FUSE* spectrum, shows that the spectrum subtly steepens at short wavelengths, and is consistent with a flatter slope of $\alpha_{opt} = 0$ shortward of 2200 Å up to O VI. The subtle upturn is seen in the inset in Fig. 2.6. Shortward of O VI the slope appears to become flatter in the *FUSE* spectrum. We have no explanation for this; it is possible that the object is not in the slit for all detectors at all times, creating a flux misalignment between the separate segments of the spectrum. Because the continuum is not detected in the SiC1a detector (Fig. 2.1), we cannot use that spectrum to check and repair the flux alignment (Brotherton et al., 2001). Regardless, we observe, as did Puchnarewicz et al. (1995), that the optical/UV spectrum does not extrapolate to the flux in the soft X-rays.

2.3 One-zone Photoionization Models using the RE 1034+39 Continuum

A primary goal of this paper is to see whether RE 1034+39's emission line equivalent widths and ratios are consistent with with its unusual spectral energy distribution. To do this, we perform photoionization modeling using the photoionization code *Cloudy* (Ferland, 2000b). In this section, we first attempt to model the lines with a one-zone model, making the simplifying assumption that the gas emitting the lines is described by a single photon flux and density. This assumption is partially justified by the similar profile and velocity width

[4] α_{opt} defined by $F_\nu \propto \nu^{-\alpha_{opt}}$

of the emission lines (§2.2). In §2.4, we relax this assumption, and compute a Locally-Optimally emitting cloud model for RE 1034+39.

Cloudy requires as input the spectral energy distribution, the photon flux, the hydrogen number density, and the column density of the gas. To compute the line equivalent widths, a covering fraction is required. Gas metallicity can also be specified; we found reasonably good results with solar metallicity, so we did not vary this parameter.

To obtain the spectral energy distribution, we used the observations shown in Fig. 2.6. The region between the *FUSE* spectrum, which extends to 960Å in the rest frame, and the *EUVE* point at 0.156 keV is not observable, and we simply extrapolate using a power law over this region. Outside of the observed band pass, we used the *Cloudy* AGN SED. Specifically, we assumed that the spectrum continues toward longer wavelengths to 10 microns before dropping sharply toward the radio. Also, as there is no spectral information above 10 keV for this object, we extrapolate the hard X-ray power law to 100 keV before requiring it to drop off sharply toward higher energies. Compared with the *Cloudy* AGN continuum, that of RE 1034+39 begins to increase toward the UV at shorter wavelengths, and is much stronger in the soft X-rays.

The photon flux, Φ, expressed in photons $\mathrm{cm}^{-2}\,\mathrm{s}^{-1}$, and the hydrogen number density, n_H, expressed in cm^{-3}, were the parameters that we sought to constrain with the simulations. To do so, we computed grids of models over a range of Φ ($16.0 < \log(\Phi) < 20.75$; $\Delta \log(\Phi) = 0.125$) and n_H ($8.5 < \log(n_H) < 11.5$; $\Delta \log(n_H) = 0.125$). Thus, we examined gas conditions over a large range of ionization parameter ($-4.0 < \log(U) < -0.5$).

For the column density, we use the parameter $\log(N_H^{max})$, which is defined as $\log(N_H) - \log(U)$, where N_H is the column density (see also Leighly, 2004a). This parameter is a convenient one for studies of photoionized gas because it adjusts the column density to

account for the ionization parameter. Therefore, for a particular value of N_H^{max}, we probe to the same depth in terms of hydrogen ionization fraction regardless of the ionization parameter. Initially, we tried a model that is optically thin to the hydrogen continuum, in which $\log(N_H^{max})$ was set equal to 21.5. This model was not able to produce the line equivalent widths and ratios; this is not surprising, because observed low-ionization lines such as Mg II are produced near the hydrogen ionization front. Ultimately, we used $\log N_H^{max} = 26$ because the slab is then sufficiently thick to produce observed low-ionization lines such as C II. Emission line fluxes and ratios for models that are optically thin to the hydrogen continuum can be very sensitive to the column density (Leighly, 2004a); optically-thick models are much less sensitive, and therefore we fix this parameter.

The similar line profiles for the high-, intermediate-, and low-ionization lines in this object suggest that all the lines are produced in gas with similar or uniform properties. Even though this may not be a precisely accurate physical description of the emission line region, as a first step, we investigate whether one region of the Φ – n_H parameter space can produce all the lines. To do this, we plot the contours for which the model equivalent widths equal the measured equivalent widths for all of the most prominent emission lines (Baldwin et al., 1996). The equivalent width of a line depends on the gas covering fraction. We varied this parameter, and determined that we could obtain a solution in which the most contours overlapped in the smallest region for a covering fraction of 0.1. The results are shown in Fig. 2.7 for the high-ionization lines (O VI, N V, C IV, and He II), and for the intermediate- and low-ionization lines (C III λ977, C II λ1335, O III] λ1666, Si III], C III], and Mg II). Lyα was not plotted. We found that the predicted value of Lyα equivalent width was $\sim$ 1.9–3.1 times higher than the observed value in the box-enclosed region. This may indicate that a slightly enhanced metals abundance may be appropriate.

We also plot the ratio of C III] λ1909 to Si III] λ1892. This ratio is useful for constraining the density because these lines are produced under roughly the same physical conditions (Hamann et al., 2002), yet they have different critical densities ($3.4 \times 10^9\,\mathrm{cm}^{-3}$ and $1.04 \times 10^{11}\,\mathrm{cm}^{-3}$). As seen in Fig. 2.7, there seems to be some dependence on the flux (and therefore ionization parameter) as well.

For the high-ionization lines, seen in Fig. 2.7, we find that there is a region in which the contours of all of the lines are close to one another near $\log(\Phi) = 18.5$, and $\log(n_H) = 9.7$, which corresponds to $\log(U) \approx -1.7$. The contours show that the peak of the C IV emission lies in this region, while O VI, N V and He II peak at higher photon fluxes.

For the intermediate- and low-ionization lines, seen in Fig. 2.7, there is a region in which contours of all of the lines are close to one another near $\log(\Phi) = 18.2$, and $\log(n_H) = 9.7$, which corresponds to $\log(U) = -2$. The contours show that the peak of the C III] λ1909 and C III λ977 emission lies in this region, while C II, O III], Si III], and Mg II peak at slightly lower fluxes.

The rectangles showing the location of the best solutions for strongest high-ionization lines (Fig. 2.7) and the strongest intermediate- and low-ionization lines overlap in a region in which the ionization parameter lies in the range $-2.35 < \log(U) < -1.65$, and in which the density is $\log(n_H) = 9.75$. Thus, we demonstrate that the line emission in RE 1034+39 is consistent with emission from gas with uniform properties, as is suggested by the similar line profiles, and is consistent with illumination of that gas by the observed extreme spectral energy distribution.

2.4 Locally Optimally Emitting models

AGN monitoring campaigns have shown that emission line fluxes vary in response to continuum flux changes, with different lag times that depend primarily on the ionization potential of the line. This means that the broad-line region is in general radially stratified. Baldwin et al. (1995) proposed that perhaps the quasar emission line region is filled with clumps of gas of differing densities and distances from the source of the ionizing continuum. If this were the case, emission lines would naturally be produced over an extended region, peaking where the conditions for their emission are optimal. This is known as the Locally Optimally Emitting Cloud model, or LOC model. We note that there is evidence in some cases that the emission region is truncated in extent, ionization, or column density. For example, double-peaked broad line radio galaxies require truncation at the outer edge of the disk to create double peaks (Eracleous & Halpern, 2004). In addition, the lack of intermediate- and low-ionization line emission in the broad blueshifted lines in some NLS1s required truncation of the column density in the wind component (Leighly, 2004a). Nevertheless, the LOC presents an arguably more physically realistic scenario than the one-zone model presented above.

In this section, we present our second photoionization analysis: an LOC model for RE 1034+39. At the same time, we recompute the LOC model using the parameters from Baldwin et al. (1995) for comparison. We first describe the assumptions of the model, and our scheme for integration, before describing the results.

2.4.1 Setting up the LOC model

Individual clouds are modeled with the same parameters used by Baldwin et al. (1995). Specifically, each single cloud has a hydrogen column density of $N_H = 10^{23}\,\mathrm{cm}^{-2}$, and is

characterized by a single value of hydrogen density n_H and photon flux Φ. In order to reproduce Baldwin et al. results, we do not use N_H^{max} for the column density, as described above. A single column density for all clouds is a good assumption as long as all clouds are optically thick to the continuum. Following Baldwin et al., we discuss the results in terms of line ratios, and therefore the covering fraction does not enter into our calculations. We use solar abundances.

We ran the LOC models for two spectral energy distributions. We use the one we inferred for RE 1034+39, described in §2.2.6. For comparison, we also compute models for the one used by Baldwin et al. (1995) that has a bump that peaks at 48 eV [5] . We computed a grid of models for each continuum over the same range of parameters used by Baldwin et al. (1995): density $8 < \log n < 14$ with $\Delta \log n = 0.125$ (cm^{-3}); photon flux $18 < \log \Phi < 23$ with $\Delta \log \Phi = 0.125$ ($\mathrm{photons\,cm^{-2}\,s^{-1}}$).

2.4.2 Distribution Function and Integration

We follow Baldwin et al. (1995) to construct our LOC models. The emission line strengths in LOC models are computed by first assuming a function for the distribution of clouds in the density/photon flux plane, then using this as a weighting function to integrate over the line emission obtained from the grid with the following integral, which gives the luminosity of each line L:

$$L = \int r^2 F_{line}(r, n) \Psi(r, n) dr dn. \tag{2.1}$$

The *Cloudy* models yield the line flux at each value of (n_H, Φ). The photon flux is related to the radius by $r \propto \Phi^{-1/2}$, and $F_{line}(r, n)$ is the line flux from the *Cloudy* models.

[5] In the *Cloudy* parameter file, this model is specified by "AGN T=800000,−1.4,−0.3,−1.0"

$\Psi(r, n)$ is the distribution function. It is assumed to be a separable function of radius and density, so that $\Psi(r, n) = f(r)g(n)$. We use a power law for the distribution functions, so that $f(r) = r^{\alpha}$ and $g(n) = n^{\beta}$. Because the *Cloudy* grids are a function of Φ rather than of r, it is convenient to express $f(r)$ as a function of Φ instead. Using the assumption that $r \propto \Phi^{-1/2}$, $dr \propto \Phi^{-3/2} d\Phi$, and $d(\log \Phi) \propto d\Phi/\Phi$, we find that $f(\Phi) \propto \Phi^{-(\alpha+1)/2}$.

In order to obtain the integrated line emission, we use a two-dimensional integration scheme employing the trapezoidal method over the grid that is uniform in $d(\log n)$ and $d(\log \Phi)$. This method requires us to determine a weight for each grid point from the distribution functions. The result is $w_{ij} = C \times \Phi_i^{-(\alpha-1)/2} n_j^{\beta+1}$, where $C = 1$ for the interior of the grid, is 1/2 for the edges, and is 1/4 for the corners.

For each line, F_{ij} is the line flux from the *Cloudy* model, and C_{ij} is the monochromatic continuum flux under Lyα at every grid point (i, j). Thus, the value F_{ij}/C_{ij} is proportional to the equivalent width. To compute the integral, we sum the weights over the grid as follows:

$$L \propto \sum_i \sum_j \frac{F_{ij}}{C_{ij}} w_{ij} d\log n d\log \Phi. \tag{2.2}$$

Using these values of the line luminosity L for each line we can compute the ratio of each line with Lyα.

2.4.3 LOC results

The ratios of the line fluxes to Lyα are given in Table 2.5 for both the RE 1034+39 and the *Cloudy* AGN continuum. We adopted the distribution functions used by Baldwin et al. (1995) in order to compare explicitly with their results ($f(r) = r^{\alpha}$ with $\alpha = -1$; $g(n) = n^{\beta}$ with $\beta = -1$). Note that Baldwin et al. (1995) erroneously report that they used $f(r) =$

constant and $g(r) \propto n^{-1}$ (p. comm. Korista)

We first verify that we can reproduce the Baldwin et al. (1995) results. The results taken directly from Baldwin et al. (1995) are given in column 2, and our re-creation of those results is given in column 3. We find slight differences due to the difference in versions of *Cloudy*; their computations were carried out with Version 90.02d, while ours were done with Version 94.00.

In column 4 we give the results from the RE 1034+39 SED, and, for comparison, the measured values from the spectra in column 5. While we are not able to match the line ratios exactly, the trends that we find are encouraging. That is, lines that are stronger with respect to Lyα in the RE 1034+39 LOC model compared with the AGN continuum LOC model are also stronger in the data. These include O VI+Lyβ, N V, O IV]+Si IV, C IV, and O III]+He II. It is notable that the highest ionization line that we measure, O VI, is much stronger in both the data and the RE 1034+39 SED model than in the AGN LOC model. This fact verifies our expectation that the extremely hard SED should yield strong high ionization lines. Generally speaking, an extremely hard SED should create stronger collisionally-excited emission lines, because each ionizing photon carries more energy on average.

The largest differences between the ratios predicted by the LOC model for RE 1034+39 and the measured ratios are for C IV, for which the model predicts about twice the observed value, and in both cases, the values are larger than those from the AGN continuum. A very large discrepancy is found for Mg II, where the model predicts about five times the observed value, and the observed value is less than that predicted from the AGN continuum. This discrepancy might have been larger had we integrated to lower flux values in the LOC computation, as Mg II is optimally emitted at $\log(\Phi) \sim 17$ (e.g. Korista et al., 1997b).

We have noticed that *Cloudy* models seem to frequently overpredict Mg II fluxes; a similar over-prediction by about a factor of two was found in models for windy NLS1s given in Leighly (2004a).

In Fig. 2.8, we show the line emissivity as a function of photon flux, assuming a 2-d geometry, for both the RE 1034+39 continuum, and the AGN continuum. In other words, we show the flux expected in each ring of area $2\pi r^2 dr$. The emissivity has been normalized by the luminosity in the entire line; i.e., we plot $L(R)/L_{total}$ for each line. For both continua, we see that significant line emission is predicted for the LOC model for fluxes lower than $\log \Phi \leq\sim 22$, out to at least $\log \Phi = 18$. However, the velocity widths of the lines may not support such a broad emission region. Assuming Keplerian velocities, a C IV velocity width of $900\,\mathrm{km\,s^{-1}}$ (Table 2.3), and an O VI velocity width of $1300\,\mathrm{km\,s^{-1}}$ corresponds to a ratio of fluxes of 4.4 at the radii where these lines should dominate, or $\Delta \log \Phi \approx 0.6$. This is a much smaller difference than the difference in the peaks of the C IV and N V distribution of $\Delta \log \Phi \approx 2.0$.

It is also interesting to note that the distribution of line emission is not much different for the two continua. The peaks for the higher-ionization lines are at slightly larger radii for RE 1034+39, except for C IV. The emissivity as a function of photon flux for Mg II is indistinguishable for the two SEDs. Another interesting thing about this plot is that the intermediate- and low-ionization lines increase strongly at larger radii (low flux). As discussed by Baldwin et al. (1995), the LOC model assumes truncation of line emission at $\Phi < 18$ as a result of graphite grains that will form in the clouds and decrease the emissivity. However, the steep increase in emissivity at larger radii predict that the observed flux of these intermediate- and low-ionization lines will depend very sensitively on the precise radius at which dust starts to dominate. This sensitivity possibly conflicts with the observation

that the equivalent widths of these lines don't vary very much from object to object.

2.5 Exploring the Influence of the Spectral Energy Distribution

In §2.3 we presented photoionization models using the RE 1034+39 SED, and found that there is a region in the Φ/n plane that can roughly reproduce the equivalent widths of the lines that we measured. In §2.4, we presented an LOC model using the RE 1034+39 continuum, and noted differences in predicted emission lines from the relatively hard RE 1034+39 and the softer AGN continuum that correspond to our expectation that a hard continuum should produce stronger high-ionization lines, and a hard continuum should produce stronger collisionally-excited emission lines.

In this section, we present the third type of photoionization analysis: we wish to determine whether the emission lines in RE 1034+39 are not only consistent with its observed hard SED, but actually require it. That is, is it possible to produce the observed emission lines with a much softer SED, for some combination of ionization parameter and density? At the same time, we want to examine the influence of the shape of the spectral energy distribution on the emission lines in a more general way, for several reasons. First, the only other systematic investigation of BLR emission-line dependence on SED that we are aware of is Krolik & Kallman (1988), who consider only three distinct SEDs, and a handful of lines. We want to consider a larger range of SEDs and a larger number of lines. Furthermore, we are also planning to use this in further investigations of the influence of the SED on emission lines (in, e.g., PHL 1811, an object with a relatively soft SED; Leighly & Casebeer (2007). Finally, we use these results to investigate whether line ratios currently commonly used as density and metallicity indicators are sensitive to the SED. However,

so that the flow of our discussion of the properties of RE 1034+39 is not interrupted, we relegate most of this discussion to §2.7. Briefly, we created a set of semiempirical spectral energy distributions parameterized by the cutoff temperature of the big blue bump kT_{cut}, which is measured in eV. We then used *Cloudy* (Version 96) to construct a grid of model line fluxes for a range of densities and ionization parameters. We calculate *a posteriori* (see §2.7.4) the effect of the global covering fraction.

2.5.1 Constraints using the RE 1034+39 Emission Lines

Using the results presented in the (§2.7), we can now address the question: is the hard spectral energy distribution that we observed from RE 1034+39 required in order to generate the observed emission-line properties? In order to address this question, we follow a procedure similar to that used in Leighly (2004a) to constrain *Cloudy* models for extreme NLS1s. We compare the line measurements from the observed spectra with the modeled line fluxes from the grids of *Cloudy* models using a figure of merit (FOM), defined as the absolute value of the difference of the base-10 log of the *Cloudy* line fluxes, transformed to the value that would be measured on Earth using the procedure described in §2.7.4, and the observed line fluxes. Note that in Leighly (2004a) the FOM was defined in terms of the line equivalent widths. Line fluxes work better here because the shape of the continuum underneath the lines changes as the SED changes; in Leighly (2004a) that continuum was held constant. Thus the FOM is defined as

$$FOM_{jkml} = \sum_i |\log(F^{model}_{here,ijkml}) - \log(F^{measured}_{here,i})| \tag{2.3}$$

where i, j, k, m, and l index the individual lines, the kT_{cut} describing the SED, the $\log(U)$, the $\log(n_H)$, and the covering fraction, respectively.

The FOM is defined using O VI λ1034, N V λ1240, C IV λ1549, He II λ1640, C III] λ1909,

and Si III] λ1892. These are the six highest-equivalent-width lines measured in RE 1034+39, excluding Lyα, which we discuss below, and the low-ionization line Mg II. As discussed in §2.7.3, the semiforbidden lines C III] and Si III] are commonly used as density indicators, and thus allow us to constrain the density in the line emitting gas in RE 1034+39.

We computed the FOM for the entire grid of *Cloudy* models. The minimum value of the FOM located the spectral energy distribution, ionization parameter, density and covering fraction that yielded line fluxes that matched most closely the observed fluxes. In Leighly (2004a) , evidence for multiple minima was found, so here we looked for multiple minima in a brute force way by sorting the data in order of increasing FOM and looking for jumps in the parameter values that would indicate another minimum. We also explored the FOM space by perturbing various parameters and examining the contours. After a thorough search, we found no evidence for multiple minima.

The minimum FOM was found for the following parameters: $kT_{cut} = 240\,\mathrm{eV}$, $\log(U) = -1.8$, $log(n_H) = 9.125$ and a covering fraction of 6%. In Fig. 2.8, we show covering fraction/density, and $kT_{cut}/\log(U)$ cuts in FOM space around this minimum. It is important first to notice that the minima are somewhat broad; as discussed in Leighly (2004a), broad minima are arguably physically more realistic because they imply that even though we are using a one-zone model, gas with properties perturbed a reasonable amount from the properties of the minimum will produce nearly identical lines so that the solution is not overly finely tuned. However, the FOM increases strongly toward lower kT_{cut} for values less than $\sim 150\,\mathrm{eV}$, indicating a harder SED is strongly favored.

Overlaid on Fig. 2.8 are the contours of the emission lines used to construct the FOM. We can see the confluence of the contours near the FOM minimum. The grid of models described in (§2.7) only include $\log(U) \leq -1.125$, so we originally could not see if there were

any other minima at higher ionization parameters. So we extend, for the best fitting values of the covering fraction and density, the $\log(U)$ vs kT_{cut} plane to higher values of $\log(U)$. Note that there is little density dependence for $\log(n_H) < 11.0$ for the high-ionization resonance lines, and, everything else being equal, the covering fraction only influences the flux, so we lose nothing by not considering those two parameters explicitly here. This extension reveals that the contours illustrating the measured values of the highest ionization lines (O VI, N V, and He II) do not dip below $kT_{cut} = 110\,\mathrm{eV}$. This indicates that a high kT_{cut} SED is supported even at high ionization parameter, and that perhaps the SED/$\log(U)$ degeneracy is broken.

Our model, however, is not without limitations. In Fig. 2.9 we show the log of the ratio of the observed data to the model at the FOM minimum, both for the strong lines used to generate the FOM, and Lyα, Mg II, Si IV λ1397, and C III λ977 as well. A prominent difference is seen for Lyα. One possible explanation for this difference is that the gas in RE 1034+39 has somewhat enhanced metallicity; our *Cloudy* models consider only solar metallicity gas. We note that we found no similar discrepancy for the LOC models. We also find prominent discrepancy for Mg II, such that the model value is much too strong. We find this also for the LOC models for RE 1034+39, as discussed in §2.4.3, and we have no explanation for this. Si IV appears to be somewhat too strong; this is a weaker line that is generally blended with O IV] λ 1404, and it may be that we prescribe too large fraction of the 1400Å feature to Si IV.

In addition, this is a one-zone model; it assumes that all the lines are produced by gas with uniform ionization parameter, density and covering fraction. As discussed earlier, this assumption may be fairly good for RE 1034+39 in particular, since the high- and intermediate-line profiles are very similar. But comparison of Fig. 2.8 and Fig. 2.9 for

the highest ionization lines may indicate the weakness in this assumption. Specifically, at the best *FOM* point, we produce too much C IV and insufficient O VI, resulting in discrepant observed-to-model ratios in Fig. 2.9. This discrepancy may be alleviated in a stratified model if a somewhat higher ionization parameter for the high-ionization lines is used. Nevertheless, the fact that the contours for the high-ionization lines lie at high kT_{cut} regardless of the ionization parameter may indicate that even for a stratified model, a relatively hard SED is still supported.

2.6 Discussion

2.6.1 Summary of Results

We have presented spectra and analysis from simultaneous *FUSE*, *ASCA*, and *EUVE* observations of the Narrow-line Seyfert 1 Galaxy RE 1034+39. Reanalysis of archival *HST* spectra were also presented. We find that almost all the lines in RE 1034+39 can be described well by narrow (FWHM $\leq\sim 1200\,\mathrm{km\,s^{-1}}$) Lorentzian profiles centered at the rest wavelength. That this is true for the UV emission lines was previously reported from the *HST* spectra by Puchnarewicz et al. (1998); our *FUSE* spectrum reveals for the first time the strong, narrow O VI line. The line profiles in RE 1034+39 are different than those in some other Narrow-line Seyfert 1 galaxies, in which only the intermediate- and low-ionization lines are narrow and centered at the rest wavelength; the high-ionization lines are broad and strongly blueshifted (e.g. Leighly & Moore, 2004). Our simultaneous far-UV and X-ray observations reveal a spectral energy distribution that peaks in soft X-rays, as was previously found by Puchnarewicz et al. (1995). This spectral energy distribution is much harder than that from typical quasars.

We presented three complementary types of photoionization analysis. First, we use the

observed RE 1034+39 spectral energy distribution, and assume that because the emission lines all have very similar profiles, they all may be emitted by gas with approximately uniform ionization parameter and density. The presence of low-ionization emission lines implies that the gas is optically thick to the continuum. The ratio of the semiforbidden lines C III] and Si III] constrains the density of the gas to be around $\log(n_H) = 9.75$. The equivalent widths of the other strong emission lines are consistent with a photon flux of $\log(\Phi) \approx 18.4$, implying an ionization parameter near $\log(U) = -1.8$.

As has been discussed by (Baldwin et al. 1995; see also Korista et al. 1997a , the line-emitting gas may not be characterized by a single ionization parameter and a single density but rather there may be a distribution of gas properties, with the emission of any particular region being dominated by emission from lines most favorably produced there; this is the Locally Optimally-emitting Cloud or LOC model. The second photoionization analysis presented is an LOC model for RE 1034+39. We computed the ratios of the emission lines with Lyα for LOC models using the RE 1034+39 SED and gas and density distributions used previously by Baldwin et al. (1995). For comparison, we reproduce the Baldwin et al. results. We find that the LOC results correspond quite well with the observations from RE 1034+39. In particular, O VI is strong, as observed. An exception is Mg II, which is observed to be about 5 times weaker than predicted by the model.

Finally, we investigated the role of the spectral energy distribution on the emission line fluxes explicitly by constructing a set of semiempirical spectral energy distributions parameterized by the cutoff temperature of the blue bump, and computing a large grid of line fluxes as a function of density, ionization parameter, and spectral energy distribution. Following Leighly (2004a), we define a figure of merit (FOM) as the sum of the absolute value of the difference between the model and observed fluxes for six strong emission lines.

We find a fairly broad minimum in the FOM around $kT_{cut} = 240\,\mathrm{eV}$, $\log(U) = -1.8$, $\log(n_H) = 9.125$, and covering fraction of 6%. The RE 1034+39 continuum most closely matches a semi-empirical SED with $kT_{cut} \sim 230\,\mathrm{eV}$, so it is not surprising that the minimum FOM solution has nearly the same ionization parameter and density as was inferred in the photoionization analysis using the observed RE 1034+39 continuum. Furthermore, the FOM increases strongly toward lower values of kT_{cut} corresponding to softer continua, indicating that a hard continuum, in the context of a one-zone photoionization model, is necessary to produce the emission lines that we see; softer continua simply do not produce the strong high-ionization lines that are the notable feature of the RE 1034+39 spectrum.

2.6.2 The O VI Line in RE 1034+39

In this section, we compare the O VI observed in RE 1034+39 with that observed in other AGN. RE 1034+39 is a somewhat exceptional object compared with most of those objects that have O VI measurements in that it has a relatively low luminosity, and a hard spectral energy distribution characterized by a flat α_{ox}. Such a hard spectral energy distribution is conducive for strong O VI emission; does RE 1034+39 match this expectation?

Zheng et al. (1995) find a significant anticorrelation between the O VI/Lyα ratio and α_{ox} in a sample of quasars observed on the ground or with *HST*, *IUE*, or *HUT*. They present a regression for this anticorrelation: $\log(\mathrm{O\ VI/Ly}\alpha) = -0.74\alpha_{ox} + 0.38$. Based on our measured $\alpha_{ox} = 1.22$, this regression predicts that O VI/Lyα will be 0.3.

We only measure the 1032Å component of O VI. Under optically-thin conditions, the ratio of the 1032Å component to the 1037Å component is 2.0. Under very optically-thick conditions, that ratio would be 1.0. Using the values for the line fluxes in Table 3, this analysis indicates a O VI/Lyα ratio between 0.76 and 1.0. So, the O VI flux relative

to Lyα appears to be particularly large compared with other objects, and it can be seen from their Fig. 2.1 that this ratio would have been the largest in the Zheng et al. (1995) sample. However, the regression of Zheng et al. (1995) has uncertainties representing the spread in values; taking into account the uncertainties shows that the observed ratio can be explained. In addition, there are some differences in the way the data were analyzed. We detect O V] λ1218, and our model removes that contribution from the Lyα flux. That was not done in the Zheng et al. sample, making their values of Lyα slightly larger, and hence their values of O VI/Lyα slightly smaller. However, if we combine our measured fluxes for Lyα and O V, it changes our ratio range to 0.59–0.78, still large compared with the rest of the Zheng et al. (1995) sample.

Zheng et al. (1995) also compare the equivalent width of the objects in their sample with the UV monochromatic luminosity. Using their cosmology ($H_0 = 50\,\mathrm{km\,s^{-1}\,Mpc^{-1}}$; $q_0 = 1$) we find that $\log(L_{1550}) = 28.1$ [erg s^{-1}] for RE 1034+39. This value makes RE 1034+39 less luminous than all but one of the objects considered by Zheng et al. Using their regression for the anticorrelation between the O VI EW and the luminosity, we find a predicted O VI equivalent width of 150Å. The observed equivalent width of O VI λ1032 component is 29Å, implying the equivalent width of the whole feature is between 43 and 58 Å. So, the predicted equivalent width is higher by greater than a factor of two. Considering the regression is between logarithmic quantities, the discrepancy is probably acceptable. Furthermore, our observed equivalent widths are consistent with the range of equivalent widths implied by the uncertainties on the regression parameters.

2.6.3 Directly Comparable Previous Results

Krolik & Kallman (1988) were possibly the first to address the issue of the response of

various emission lines to the shape of the spectral energy distribution, with the aim of trying to determine the shape of the continuum in the unobservable extreme ultraviolet. They consider three spectral energy distributions that are different in the shape of the extreme UV. They compute emission line ratios for combinations of three ionization parameters and three pressures, finding that some ratios vary negligibly between the different SEDs, while some ratios show considerably greater range. They attribute these results to some extent to the relative strength in the continuum bands responsible for exciting production of particular emission lines. For example, He II λ1640 and O VI are sensitive to the helium continuum, and therefore tend to be stronger with respect to Lyα for SEDs with strong helium continuum compared with Lyman continuum.

In (§2.7), we present similar computations as were presented by Krolik & Kallman (1988). A difference is that we examine a much larger range of spectral energy distributions and ionization parameters, although we do limit ourselves to discussion of a single density and slabs that are optically thick to the continuum in this paper. Another difference is that we examine a larger number of lines. Our inferences are more or less the same for our harder continua (§2.7.2). However, our results are somewhat different for the very soft continua that were not investigated by Krolik & Kallman (1988). For these continua, the low-ionization lines, which are produced below the hydrogen ionization front for the harder continua, are produced above the hydrogen ionization front and become primary coolants. While not directly applicable in this paper, the results of low-kT simulations are important for understanding objects with soft continua such as PHL 1811 (Leighly & Moore, 2006).

2.7 Semi-Empirical SED

2.7.1 Photoionization Modeling with a Semi-Empirical SED

To test the influence of the spectral energy distribution on the line emission, we needed a series of SEDs that could be expressed simply mathematically, and yet are approximately physically realistic. We start with the AGN spectrum that is included in the *Cloudy* package:

$$f_\nu = \nu^{-\alpha_{uv}} e^{\frac{h\nu}{kT_{cut}}} e^{\frac{kT_{IR}}{h\nu}} + a\nu^{\alpha_x}. \tag{2.4}$$

This equation models the big blue bump as a power law with index α_{uv} in the optical and UV with an exponential cut off at high energies parameterized by the temperature T_{cut}, and an exponential cutoff at low energies parameterized by T_{IR}. A power law with index α_x models the X-ray spectrum. We fixed the optical/UV power law index to $\alpha_{uv} = 0.33$, adopting the observationally-determined mean value from a sample of quasars by Natali et al. (1998), which is in agreement with the mean obtained from the LBQS by Francis et al. (1991a), and with the Einstein sample from Elvis et al. (1994). We fixed the X-ray power law continuum slope to $\alpha_x = 1$ (e.g. Zdziarski et al., 2000).

For the thin disk model, the high energy cutoff for the optical-UV continuum is theoretically related to the temperature of the inner edge of the accretion disk. For a fixed accretion rate with respect to the Eddington value, and for a fixed efficiency of conversion of accretion energy to radiation, we expect the accretion disk luminosity to be proportional to T^{-4}. The relative normalization between the X-ray and UV is observed to be dependent on luminosity through α_{ox}, the point-to-point slope between 2500Å and 2 keV (Wilkes et al., 1994). We use the theoretical constraint provided by the inner edge temperature, and the empirical constraint provided by the α_{ox} to relate T_{cut} to the X-ray power law normaliza-

tion a through their mutual dependence on luminosity. The proportionality constant was determined using the measured T_{cut} from coordinated *IUE* and *ROSAT* observations of the quasar 3C 273 (Walter et al., 1994). Our final constraint relates the lower limit frequency of the X-ray power law to T_{cut} so that the power law cannot be discerned in the optical-UV band.

In the discussion that follows, the spectral energy distribution is uniquely parameterized by the value of kT_{cut}. We computed photoionization models for a range of kT_{cut} from 10 eV to 320 eV, with $\Delta kT_{cut} = 10$. A representative subset of the spectral energy distributions, normalized so that they all have the same ionizing flux, are shown in Fig. 2.11. As shown in Fig. 2.12, a spectral energy distribution with $kT_{cut} = 230$ eV coincides fairly well with the spectral energy distribution of RE 1034+39, and one with $kT_{cut} = 10$ eV corresponds well with that of PHL 1811, a luminous NLS1 (Leighly et al., 2001, 2004; Leighly & Moore, 2006). This demonstrates that these semiempirical SEDs are representative of observed SEDs.

Our primary goal is to determine whether the emission lines in RE 1034+39 require a hard spectral energy distribution, or whether they are independent of SED. Thus, we choose the remaining parameters for the photonization models to be appropriate for RE 1034+39. In §2.3 we found that the column density should be large enough to be optically thick to the continuum. Therefore, here we use $N_H^{max} = 25$, which is sufficiently thick to produce low-ionization lines such as C II. We verified that, for a fixed ionization parameter, the depth of the hydrogen ionization front is almost independent of the shape of the spectral energy distribution (Fig. 2.13). However, the depth of the helium ionization front changes, being deeper for harder SEDs (Fig. 2.13). This trend is expected, as a larger proportion of the ionizing photons are in the helium continuum for harder SEDs.

We run *Cloudy* models for SEDs with $10 < kT < 320$; $\Delta(kT) = 10$, for hydrogen densities $7.875 < \log(n_H) < 12.75$; $\Delta(\log(n_H)) = 0.125$, and for ionization parameters $-3.0 < \log(U) < -1.25$; $\Delta(\log(U)) = 0.125$. Thus, 19,200 models were considered.

Lyα is a recombination line, and its intensity will depend primarily on the depth of the hydrogen ionization front for the fixed density considered in these models. Thus, its intensity should depend *only* on the ionizing flux, which is proportional to the ionization parameter for a fixed density, and be independent of the shape of the continuum, as long as the density is not so high that it starts to become thermalized. The contours of Lyα flux as a function of ionization parameter and kT_{cut} show that this is indeed the case (Fig. 2.14). Therefore, to partially remove the effect of the ionization parameter, we present the results as ratios of lines with respect to Lyα.

2.7.2 Model Results

In this discussion, we consider only the dependence on the spectral energy distribution and ionization parameter, and consider only one density, $n_H = 10^{10}\,\mathrm{cm}^{-2}$. Fig. 2.15–2.19 shows contours of emission lines with respect to Lyα for the adopted range of kT_{cut} and ionization parameter. We divide the results into four categories based on the ionization potential of the emitting ion and the emission mechanism. Figures 2.15–2.18 show the predominately collisionally excited lines, with Fig. 2.15 showing lines with ionization potential (I.P.) greater than that of He II (I.P. $>$ 54.4eV), Fig. 2.16 showing lines with I.P. between that of hydrogen and helium (13.6 $<$ I.P. $<$ 54.4), and Fig. 2.17 with I.P. less than that of hydrogen (I.P. $<$ 13.6 eV). Fig. 2.19 shows recombination lines from hydrogen and helium.

The behavior of some lines is quite easy to understand. For example, Fig. 2.15 shows the emission lines from ions with ionization potential higher than that of He^{2+}. They

are emitted most strongly when the continuum is relatively hard, because the ionization potential of the ions that create these lines is relatively high. They are emitted strongly when the ionization parameter is high because a high ionization parameter is required for the high ionization state. In addition, the harder continuum generates a higher temperature in the gas. The lines shown here are those from transitions with low excitation potentials, and are thus primary gas coolants. Therefore, the contours shown in Fig. 2.15 have maxima along the top of the plot, where the continuum is hard, and tail toward the right side, where the ionization is high.

Turning to Fig. 2.16, we find emission lines emitted between the helium ionization front and the hydrogen ionization front. In particular, C IV and N IV] are emitted most favorably at intermediate values of the ionization parameter, near $\log(U) = -1.5$. Again, these peak for the hardest continua because they are important gas coolants.

The situation is somewhat different for the intermediate ionization lines O III], Si IV, N III λ991, N III] λ1750, C III λ977, and C III] λ1909, shown in Fig. 2.16. These lines are most favorably produced at somewhat lower ionization than the lines discussed above. Therefore, their contours peak along the top of the plots at slightly lower ionization parameter (e.g., $\log(U) \approx -2$ for C III). They also show enhancements along the right side of the plots for continua with intermediate hardness. This occurs because in this region of the plots, the continua are too soft to create abundant ions with highest ionization; intermediate ionization states are dominant above the hydrogen ionization front. This is a consequence of the reduction in depth from the illuminated side of the slab to the helium ionization front, and the corresponding increase in depth of the intermediate ionization region between the helium and hydrogen ionization fronts as the spectra become softer. Thus, at high ionization, the gas cools via production of intermediate ionization lines. The

excitation of the ions is predominately collisional in both regions of the plots, so permitted and semiforbidden lines have roughly the same behavior.

The situation is radically different for the intermediate ionization lines Al III and Si III]. The contours from these lines, shown in Fig. 2.17, peak at intermediate ionization parameter, but are stronger for the softer spectra. It is particularly interesting to note the differing behavior for C III] and Si III]; the contours shown in Fig. 2.17 are almost mutually exclusive. The ions responsible for these lines are isoelectronic. Both are transitions from the ground state to levels with the same configuration ($^3P^0$), and their excitation potentials are quite similar. The principle difference between them appears to be the ionization potential to create the +2 and +3 ions. To create Si^{2+} and C^{2+}, the ions emitting these lines, 16.4 and 24.3 eV are required, respectively. To ionize them to the +3 state, 33.4 and 47.9 eV are required, respectively. Thus, Si^{2+} is more favorably produced when the continua are soft; for harder continua, the predominate ionization state in the intermediate ionization region is Si^{3+}. Furthermore, the *Cloudy* output indicates that for $\log(U) \approx -2$ and for the softer spectra, Si III] is the predominant coolant. Al III behaves similarly, although it is a permitted line, as the ionization potentials to create Al^{2+} and Al^{3+} are 18.8 and 28.4 eV, respectively.

Moving to the low-ionization lines, we show contours from N II, C II, Si II, Al II, Mg II, Ca II, and Na I in Fig. 2.17 and 2.18. The contours from these lines exhibit different behavior. First we consider the pairs of lines of N II λ1085, N II] λ2140, and C II λ1335, C II] λ2326. In both cases, the semiforbidden line is most strongly emitted at low ionization parameter for a hard spectrum, while the permitted line is most strongly emitted at a high ionization parameter for a soft spectrum. Although these are low-ionization lines, they are emitted in the partially ionized zone only for the hard spectra and high ionization param-

eter. Examination of the *Cloudy* output shows that this contrasting behavior originates in different excitation of the ion in the two regimes. At low ionization parameter, the semiforbidden line is collisionally excited. For a particular ionization parameter, it therefore emits most strongly for the harder spectra because the gas temperature is higher. The permitted lines are weaker in this regime because they have much higher excitation potentials than the semiforbidden lines, and for the low ionization parameters at which the appropriate ions exist, the temperature is not high enough to excite them. They are emitted more favorably for soft spectra at high ionization parameter as a result of pumping by the continuum.

The behavior of the low-ionization line Si II is interesting. The Si^+ ion has five groups of permitted resonance transitions with upper level energies less than 11 eV, near 1160, 1263, 1308, 1531 and 1814 Å. For harder continua, the *Cloudy* output indicates that the excitation is predominately collisional. Thus, the 1814 Å line is generally predicted to be the strongest of the Si II resonance lines, and is further predicted to be stronger relative to Lyα at the lowest ionization parameters. But for the softer spectra, continuum pumping is the predominate process for the higher excitation transitions. In fact, for the highest ionization parameter and softest spectrum, the higher-ionization transitions are as strong or stronger than Si II λ1814. This is an interesting result, because while SI II λ1263 and Si II λ1308 are strong in some AGNs, Si II λ1814 is not correspondingly strong, a result that has been difficult to explain (Baldwin et al., 1996). This issue will be examined further in Leighly & Moore (2006).

We turn next to the low ionization lines from Mg^+, Al^+, Ca^+, and neutral sodium (Fig. 2.18). These contours tend to be enhanced for the hardest and softest spectra. For the hardest spectra, these emission lines are produced to a large extent in the partially ionized zone beyond the hydrogen ionization front. The partially ionized zone is predominately

powered by X-rays. As shown in Fig. 2.13, as the spectra become softer, the depth of the partially-ionized zone shrinks, resulting in relatively less emission at a given ionization parameter for spectra with intermediate hardness. For the softest spectra, these lines are again produced strongly, because the ions emitting these lines have low ionization potentials; thus these lines serve relatively larger role as cooling agents when the spectra are soft.

Finally, we consider the recombination lines from hydrogen and helium. The He II lines are relatively easy to understand. They are strong when the helium ionization front is deep. As seen in Fig. 2.13, this is true when the continuum is hard. In contrast, He I is strong when the region between the helium and hydrogen ionization fronts is large; as seen in Fig. 2.13, this condition is met when the continuum is relatively soft.

2.7.3 SED Dependence of the Density Diagnostic Si III]/C III]

The ratio of the semiforbidden lines Si III] and C III] is frequently used to estimate the density of the emitting gas. These emission lines are produced by isoelectronic ions and have similar but not identical excitation potentials, and therefore in principle should be produced under roughly the same conditions. The important difference is in their critical densities: $1.04 \times 10^{11}\,\mathrm{cm}^{-3}$ and $3.4 \times 10^{9}\mathrm{cm}^{-3}$ for Si III] and C III] respectively.

The analysis presented above shows, however, that these emission lines are not independent of the spectral energy distribution, as a consequence of their different roles in cooling the gas, which may be the consequence of the differing ionization potentials. As discussed above, for intermediate and soft spectra with ionization parameter of $\log(U) = -2.5$, Si III] is emitted strongly because it is one of the primary coolants for the gas; for harder spectra, the ions responsible for cooling are instead C^{3+} and Si^{3+}. Thus, a high Si III] to C III] ratio could either indicate high density, or a soft spectral energy distribution. This is illus-

trated in Fig. 21, which shows, for example, a range of greater than 2 in this ratio *for a fixed density and ionization parameter* near $\log(U) = -2.3$, as the SED varies from hard to soft. Thus, there is a degeneracy between density and spectral energy distribution for the Si III]/C III] ratio that in principle could hamper its use as a density indicator.

This degeneracy may be partially broken by using Al III in combination with Si III] and C III]. Al III is also predicted to be strong when the spectrum is soft, but it has little dependence on density because it is a permitted line. Thus, if both Al III and Si III] are strong with respect to C III], a soft spectrum may be indicated; if Al III is weak while Si III] is strong, a high density may be indicated.

2.7.4 SED Dependence of Metallicity indicators

We looked at the SED dependence for three different metallicity indicators (e.g. Hamann et al., 2002): N III λ1750/O III] λ1666, N V λ1240/C IV λ1550, and N V/(O VI+C IV) (Fig. 2.21). Fig. 2.21a shows that N III]/O III] has little dependence on the spectral energy distribution, and is therefore arguably the most reliable metallicity indicator. In contrast, Fig. 2.21b shows that the N V/C IV ratio has a strong dependence on ionization parameter, and some dependence on SED for the softest spectral energy distributions. The ionization parameter dependence is partially mitigated by using instead the N V/(C IV+O VI) ratio (Hamann et al., 2002) as shown in Fig. 2.21c, except for the softest SEDs.

2.7.5 Obtaining the Observed Model Line Fluxes for Comparison With Measured Values

For reference, in this section, we describe the method that we used to compare the *Cloudy* results with the observed line fluxes.

The luminosity of the ionizing light observed here on Earth equals the luminosity of the ionizing light at the continuum source, i.e.,

$$L_{here} = L_{there}. \tag{2.5}$$

Therefore, if d equals the distance from the ionizing continuum source to the observer, Φ equals the number flux of ionizing photons from the continuum source, and r equal to the distance from the ionizing continuum source to the photoionized gas, we find that

$$\Phi_{here} d^2 = \Phi_{there} r^2, \tag{2.6}$$

so that

$$\frac{\Phi_{here}}{\Phi_{there}} = \frac{r^2}{d^2}. \tag{2.7}$$

If the clouds do not cover the ionizing continuum source completely, the covering fraction CF must be taken explicitly into account so that

$$r^2 CF F_{there} = d^2 F_{here}. \tag{2.8}$$

Eliminating the distances using Equation 7, and taking the base-ten log, we obtain

$$\log(F_{here}) = \log(\Phi_{here}) - \log(\Phi_{there}) + \log(CF) + \log(F_{there}). \tag{2.9}$$

The figure of merit is defined as the absolute value of the difference in the base-ten log of the line fluxes, and is given by

$$FOM_{ijkml} = |\log(\Phi_{here}) - \log(\Phi_{there,k}) + \log(CF_l) + \log(F^{model}_{there,ijkm}) - \log(F^{measured}_{here,i})| \tag{2.10}$$

where i, j, k, and m index the individual lines, the value of kT_{cut}, the value of $\log(U)$, and the value of $\log(n_H)$, respectively.

Assuming arbitrarily that $\log(\Phi_{there})$ is 17.75, then we can express $\log(\Phi_{here})$ as

$$\log(\Phi_{here}) = 17.75 - \Delta\log(\Phi), \tag{2.11}$$

where $\Delta\log(\Phi)$ is the scaling factor required to reduce the observed continuum with photoionizing flux of 17.75 to the photoionizing flux we observe on Earth. Comparing the *Cloudy* output with the observed spectral energy distribution indicates that $\Delta\log(\Phi) = 18.25$. Inserting Equation 11 in to the FOM equation results in

$$FOM_{ijkml} = |17.75 - 18.25 - \log(\Phi_{there,j}) + \log(CF_l) + \log(F^{model}_{there,ijkm}) - \log(F^{measured}_{here,i})|. \tag{2.12}$$

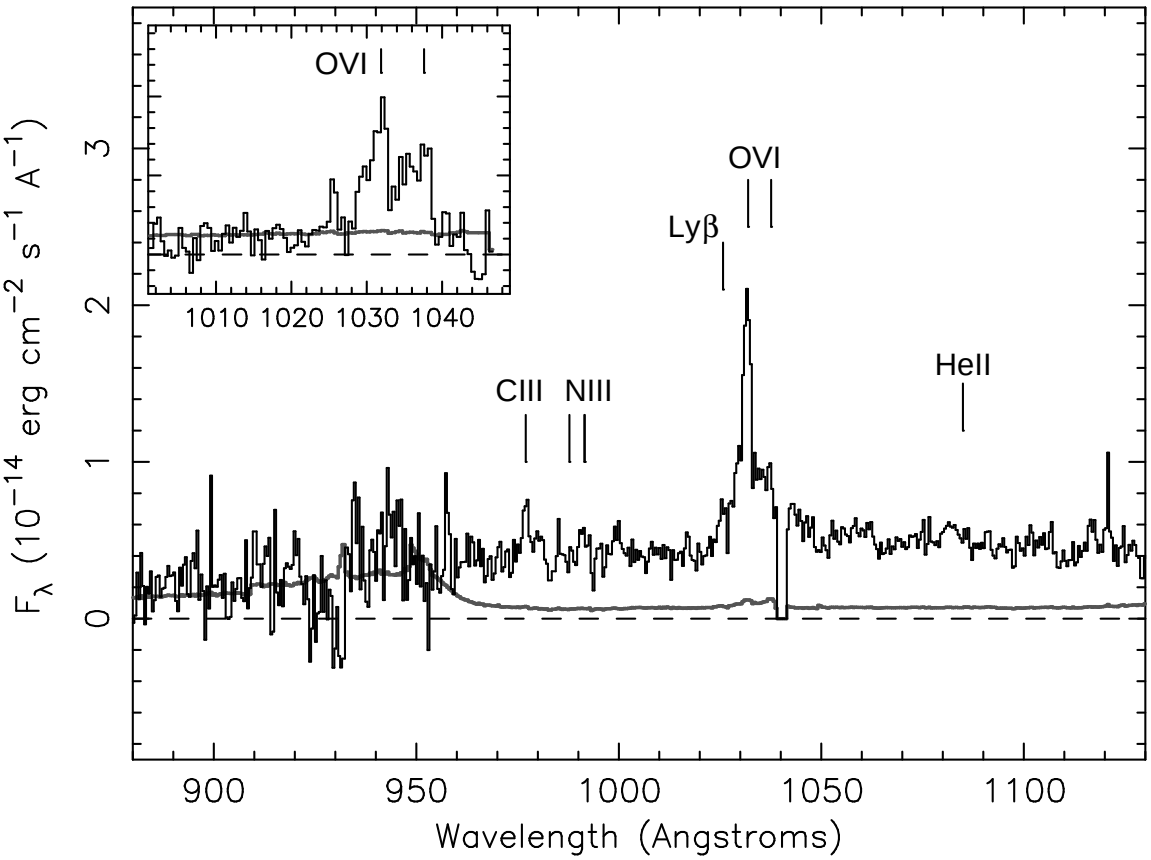

Figure 2.1 The extracted, coadded *FUSE* spectrum of RE 1034+39. Airglow lines from Lyβ, Lyδ, and Lyγ have been removed. The thick line shows the uncertainty spectrum. Emission lines commonly observed in this bandpass in AGN are labeled; we detect C III, O VI, and Lyβ. Note that the 1037 Å component of the O VI doublet was not detected in the LiF1a spectrum, as it falls on the edge of the detector where background is enhanced (see text for details). Inset: the SiC1a spectrum, showing enhancements at the appropriate wavelengths for both components of the O VI line.

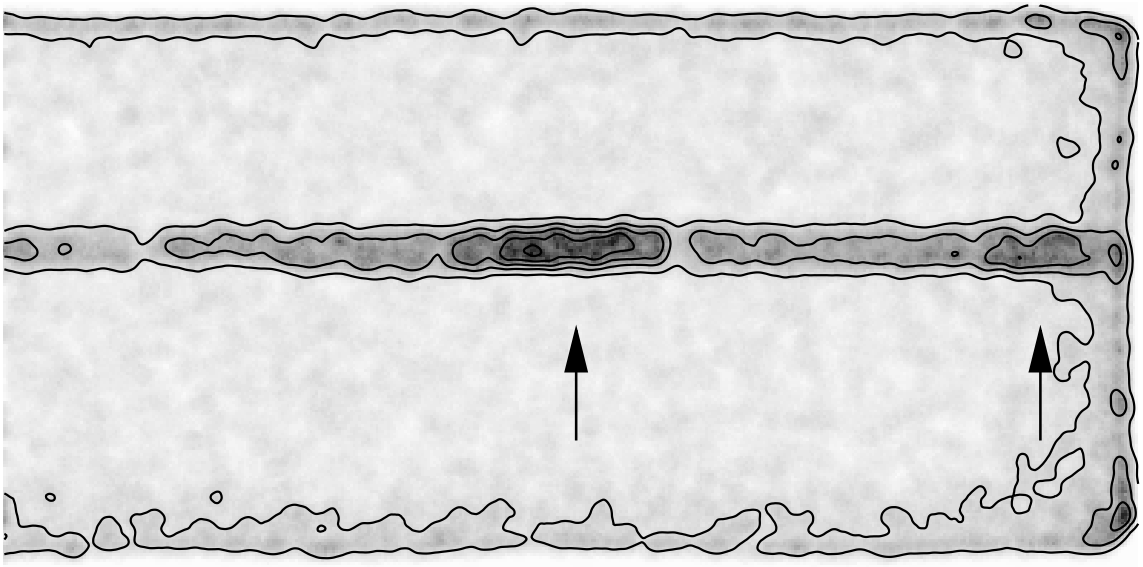

Figure 2.2 The long wavelength portion of the LIF1 detector image, after screening and before background subtraction. The image has been adaptively smoothed and is plotted on a linear scale. The LIF1a trace is clearly detected. The arrows show approximate expected centers of the O VI doublets. The 1031.93Å component is clearly seen. The 1037.62Å component can be seen near the edge of the detector, where the effective area is lower and the background is higher.

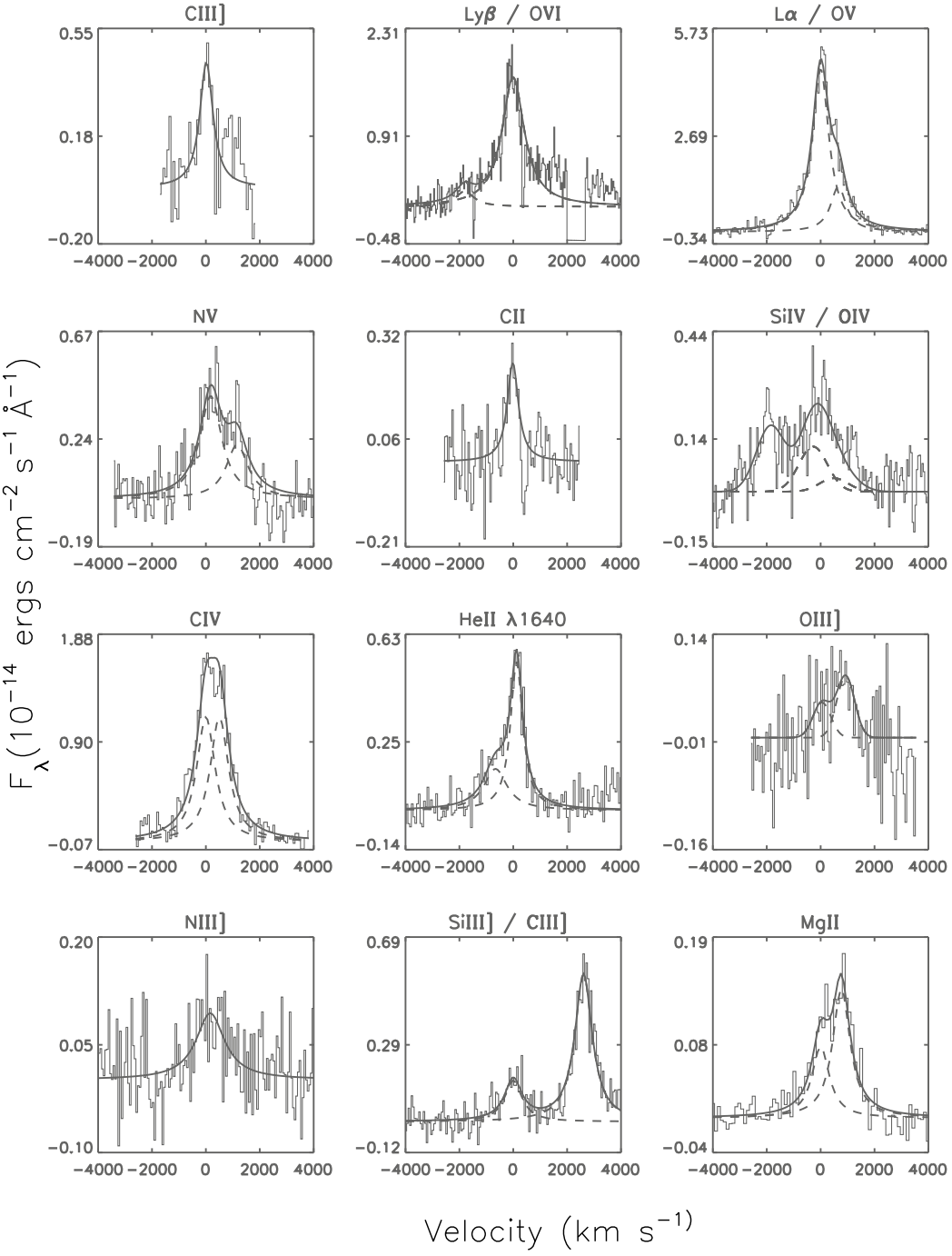

Figure 2.3 The models for the emission lines in the RE 1034+39 spectra, after continuum subtraction. All emission lines are consistent with a Lorentzian profile.

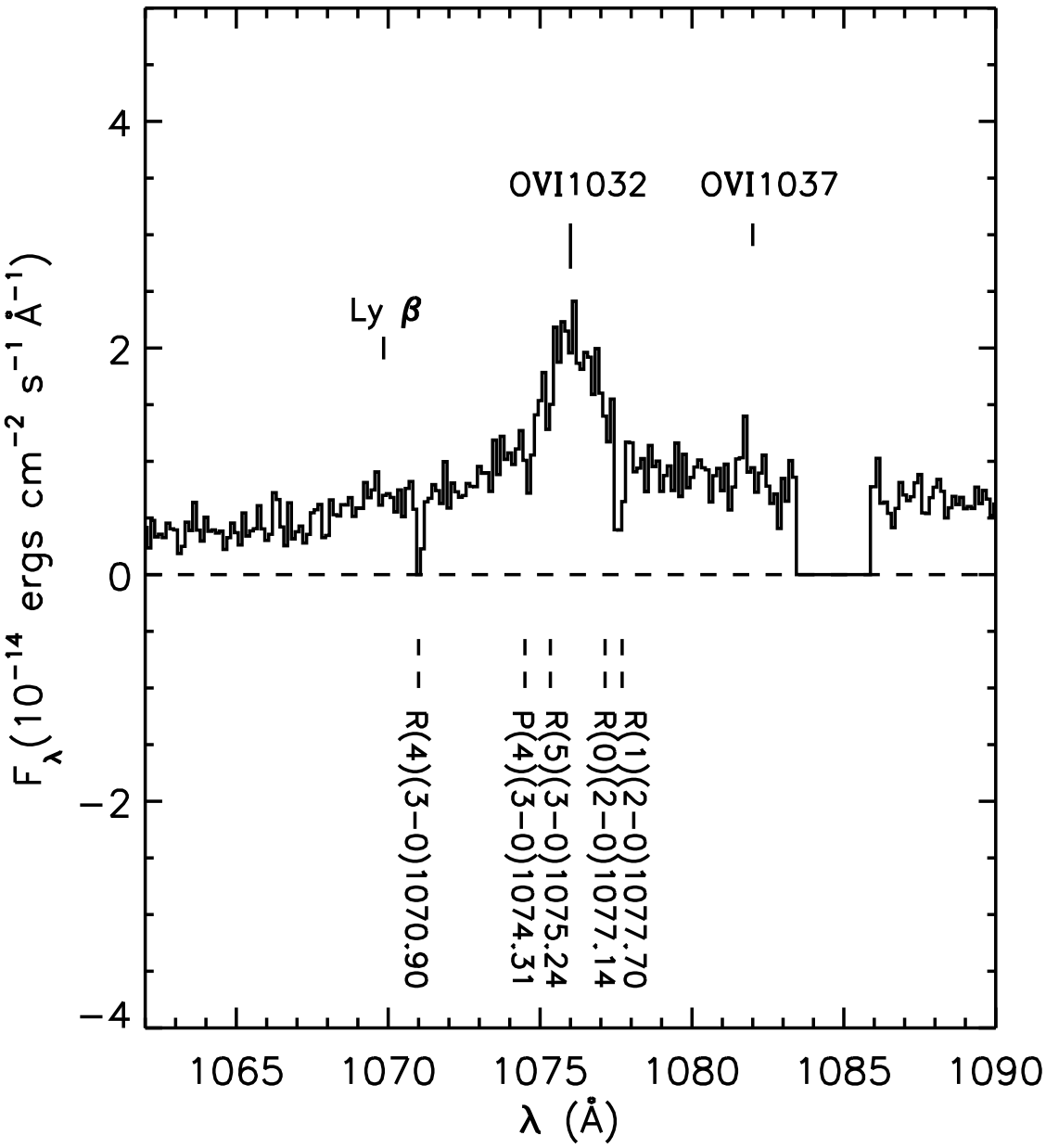

Figure 2.4 The region of the spectrum containing O VI and Lyβ. The rest-frame positions of the emission lines are labeled above the plot; the Galactic absorption lines are labeled below. All absorption lines are consistent with zero redshift molecular hydrogen transitions originating in our Galaxy; no absorption lines intrinsic to the AGN are observed.

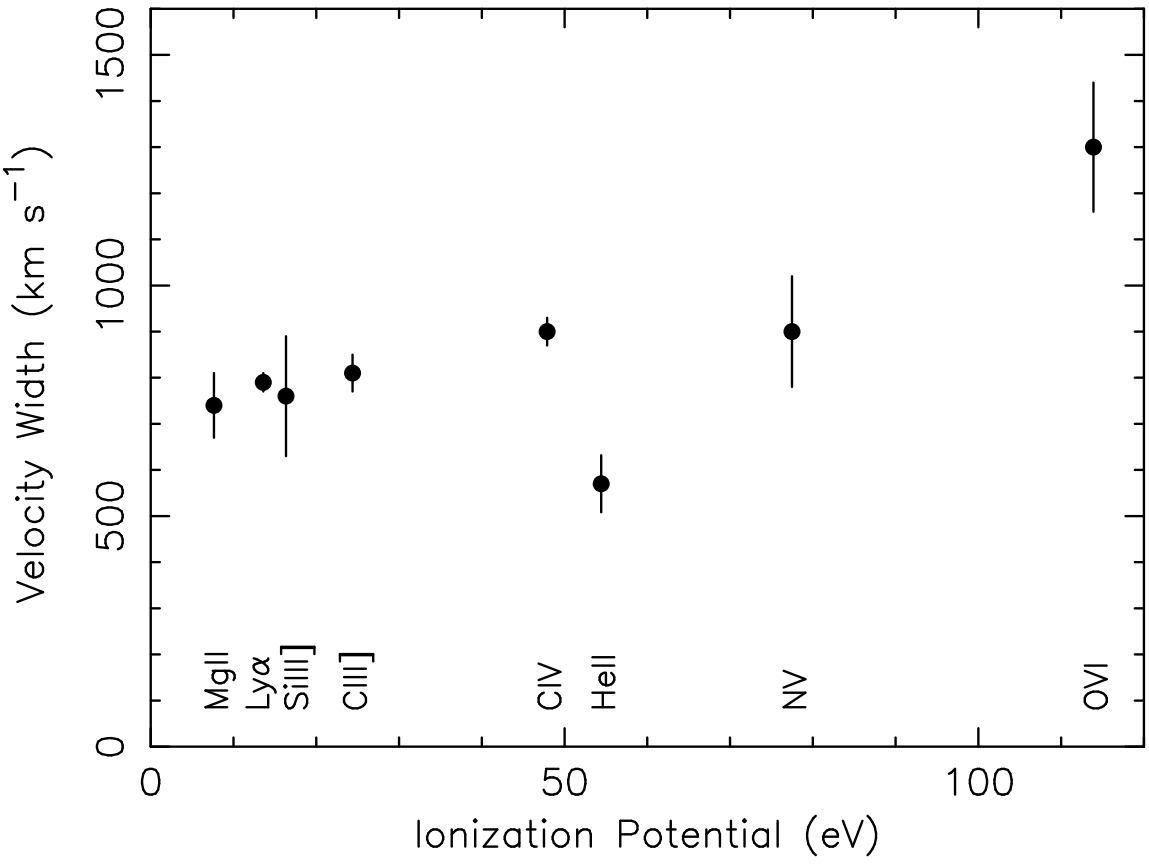

Figure 2.5 The velocity width (FWHM) as a function of ionization potential for the brighter and least-blended FUV and UV emission lines. A slight increase in velocity width potentially indicates stratification of the emission line region. The exception is He II which differs from the other lines because it has a blue wing; deblending the blue wing may result in a narrower core.

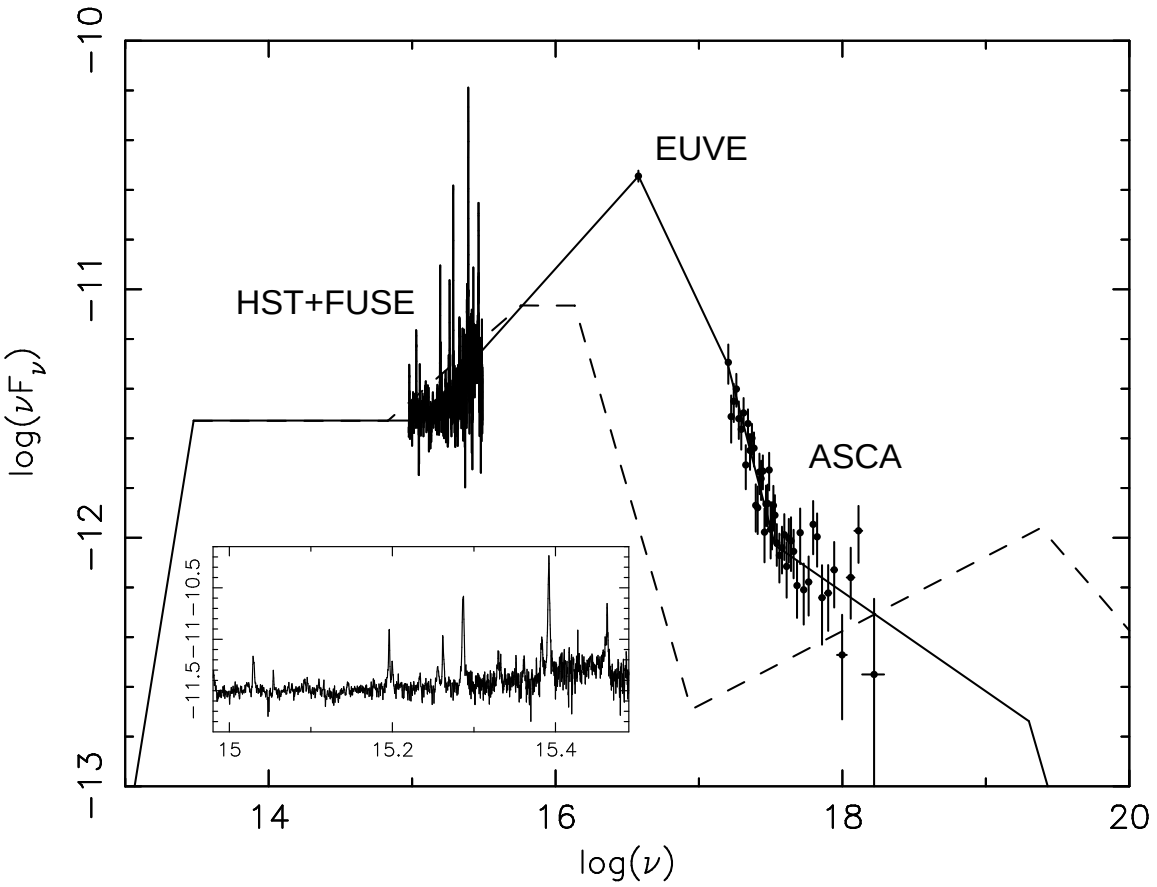

Figure 2.6 The adopted continuum for *Cloudy* simulations was constructed from the simultaneous *FUSE*, *EUVE* and *ASCA* data, and the nonsimultaneous *HST* data. The *Cloudy* AGN continuum is shown for comparison (dashed line). The inset shows the subtle upturn in the UV continuum toward high frequencies.

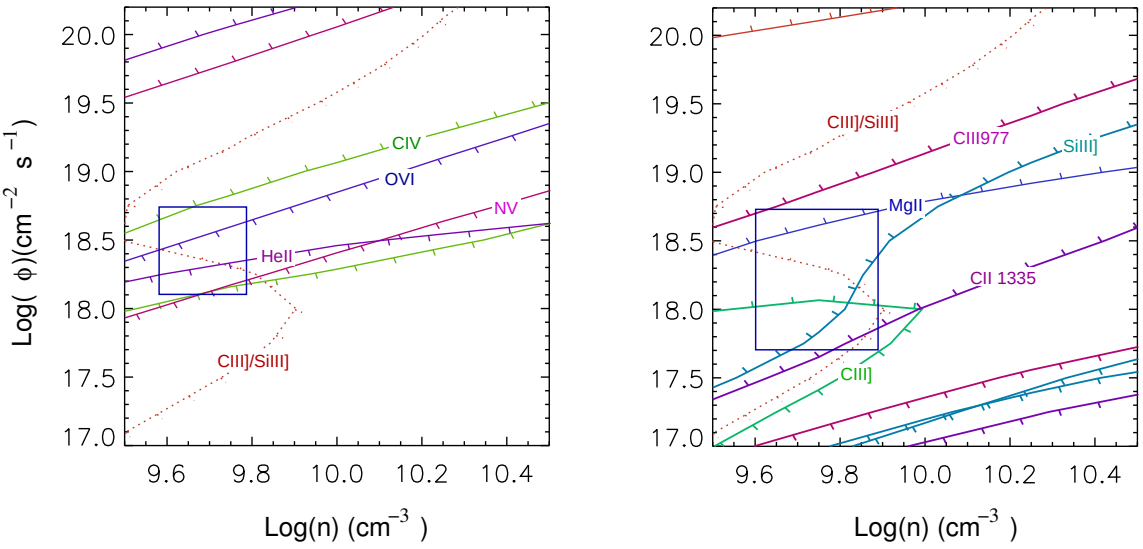

Figure 2.7 *Cloudy* model results for the high-ionization lines (left) and the intermediate- and low-ionization lines (right). The dotted line shows the ratio of C III] to Si III], a parameter that should be sensitive to density. The contour ticks mark the direction of decreasing equivalent width. The boxes delineate the region of parameter space that is intersected by all contours.

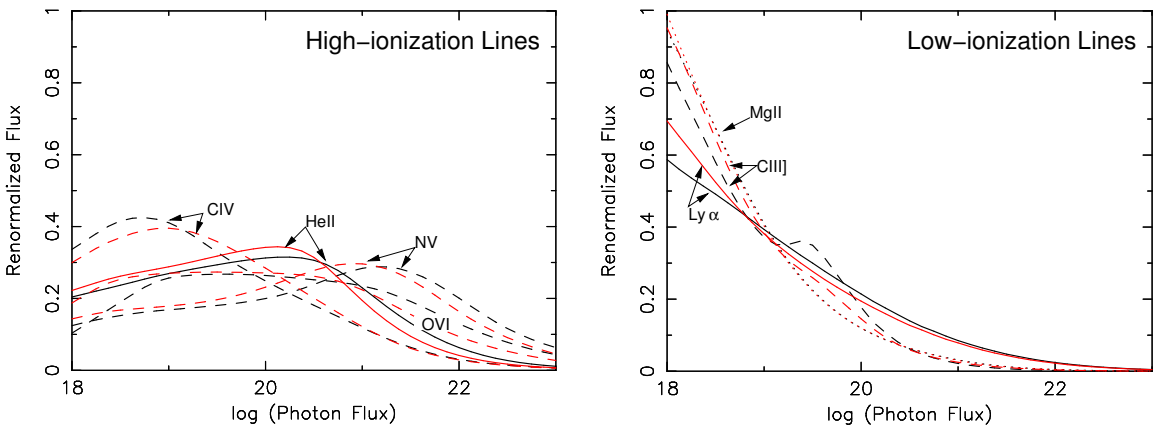

Figure 2.8 Renormalized line emissivity for a 2-d, flattened geometry for LOC models. The left plot shows the results for the high-ionization lines, and the right plot shows the results for the intermediate- and low-ionization lines. The red and black lines show the results for the RE 1034+39 and AGN continua, respectively. Little difference is seen between these two continua; however, the emission is distributed over a much larger $\Delta\Phi$ than is implied by the difference in the velocity widths of the lines. The emissivity of the low-ionization lines rises strongly toward large radii (low fluxes) perhaps indicating sensitivity of these lines to the value of the lowest Φ used in LOC models.

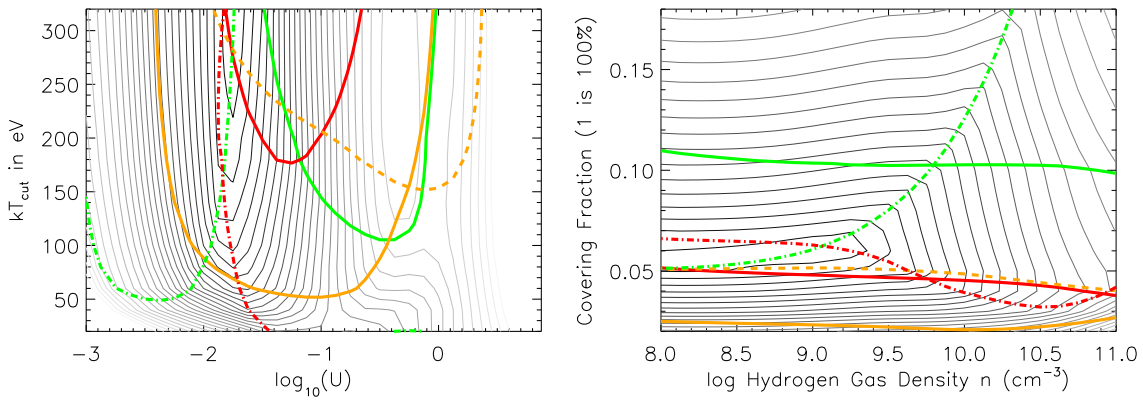

Figure 2.9 *Cloudy* model results for cuts through the FOM matrix around the global minimum located at $kT_{cut} = 240\,\mathrm{eV}$, $\log(U) = -1.8$, $\log(n_H) = 9.125$, and covering fraction of 6%. The spectral energy distribution parameterized by kT_{cut} versus the ionization parameter $\log(U)$ (*left*) and the covering fraction versus the hydrogen density $\log(n_H)$ (*right*) are shown. The thin, grayscale contours show the FOM with interval of 0.4, and with the darker contours in the minimum. The thick colored contours show where the model line fluxes equal the measured line fluxes with the following key: green – O VI; red – N V; orange – C IV; dashed orange – He II; dash-dot red – Si III]; dash-dot green – C III] (i.e., permitted lines are solid, recombination lines are dashed, and intercombination lines are dash-dotted.)

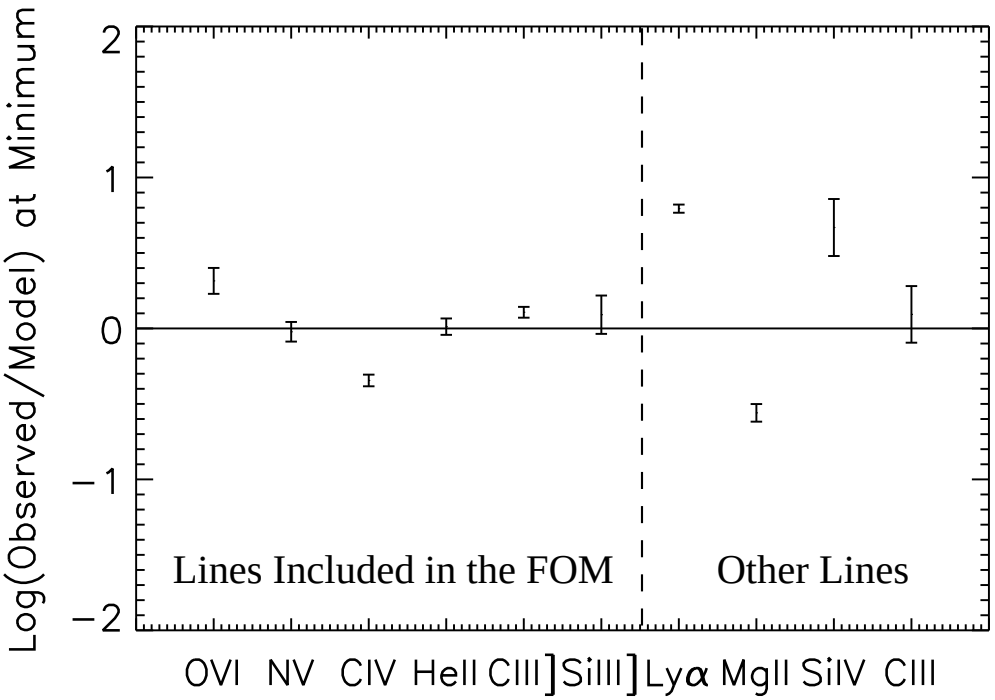

Figure 2.10 The log of the ratio of the observed line fluxes with model line fluxes. Error bars indicate statistical uncertainty from the spectral fitting. The six lines on the left were used to construct the FOM.

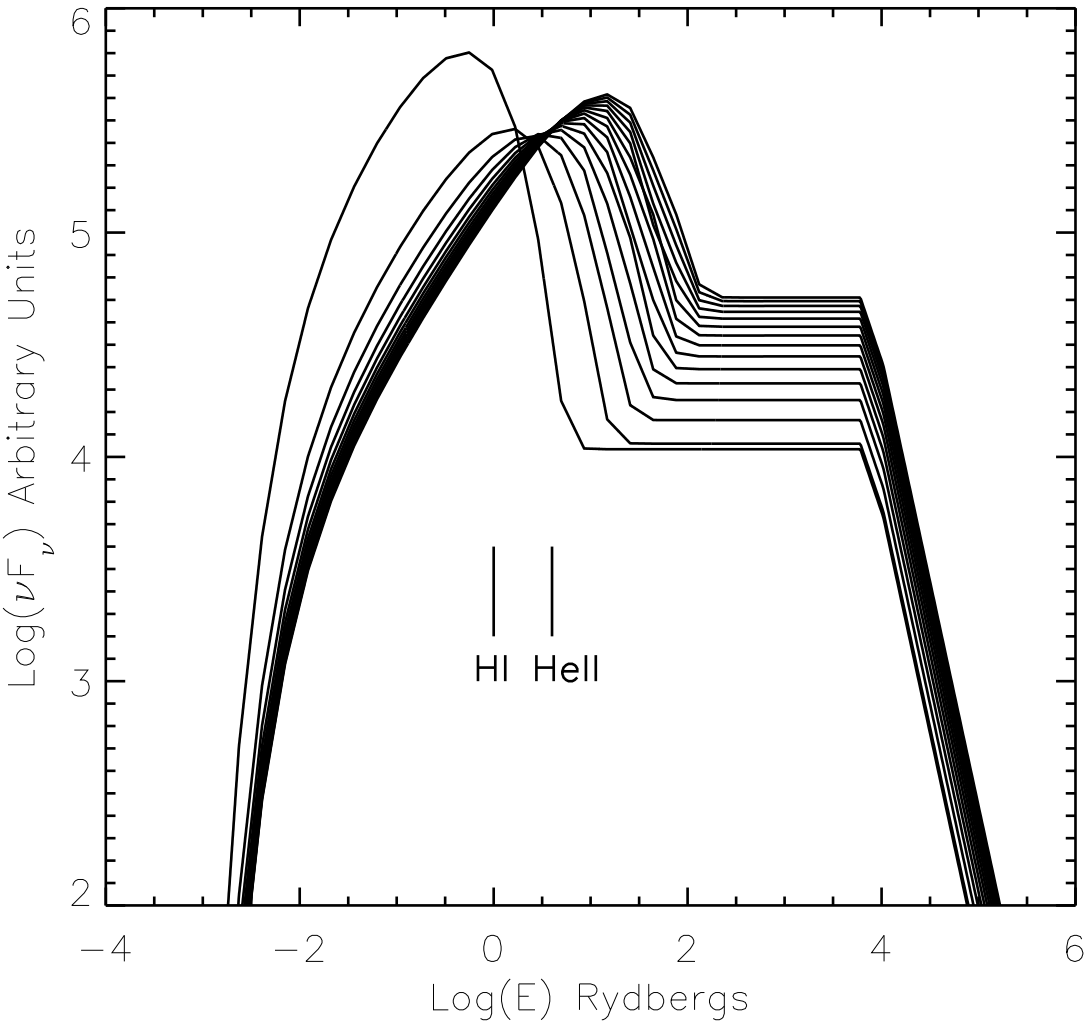

Figure 2.11 A representative set of the semi-empirical spectral energy distributions used in §2.7, normalized so that they all yield the same value of the ionizing flux.

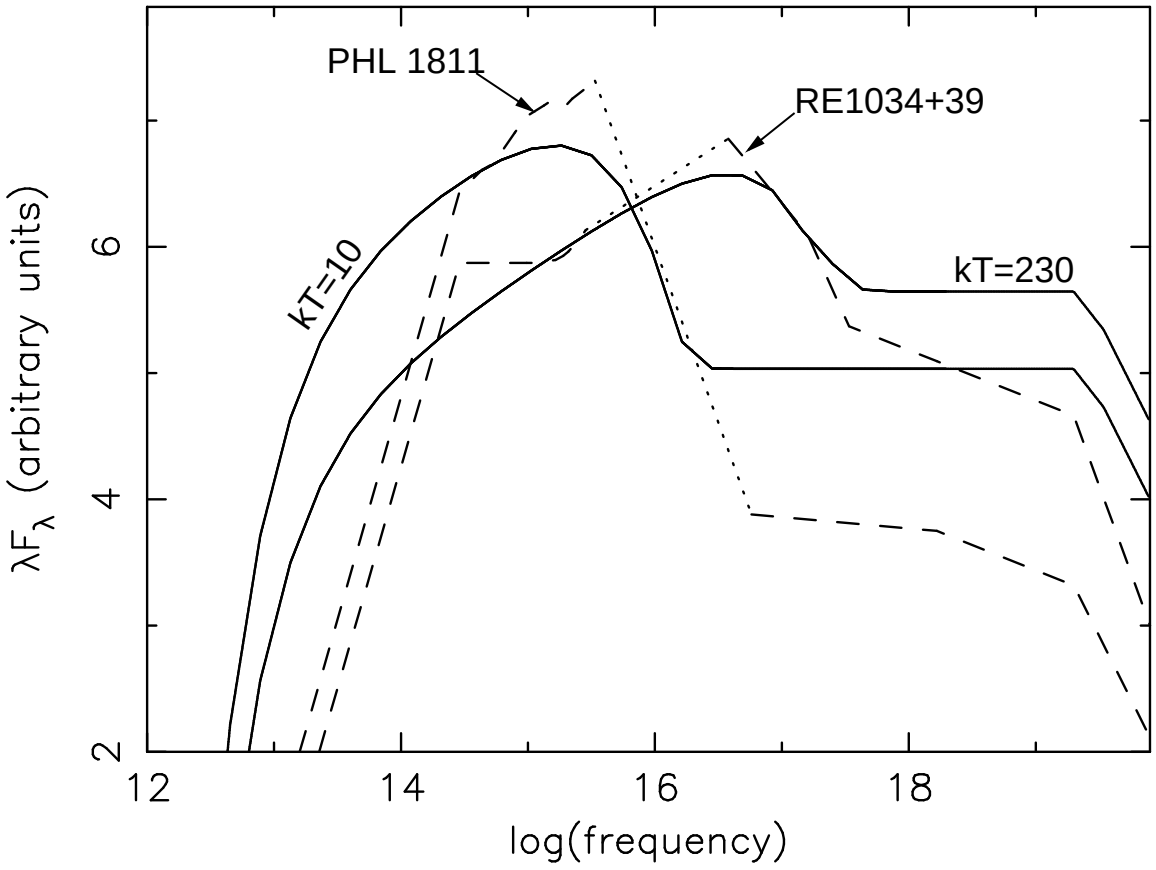

Figure 2.12 Comparison of observed SEDs (solid lines) from coordinated observations with the semi-empirical spectral energy distributions (dashed lines; dotted lines in the unobservable EUV), illustrating that the semi-empirical SEDs correspond fairly well with observed ones.

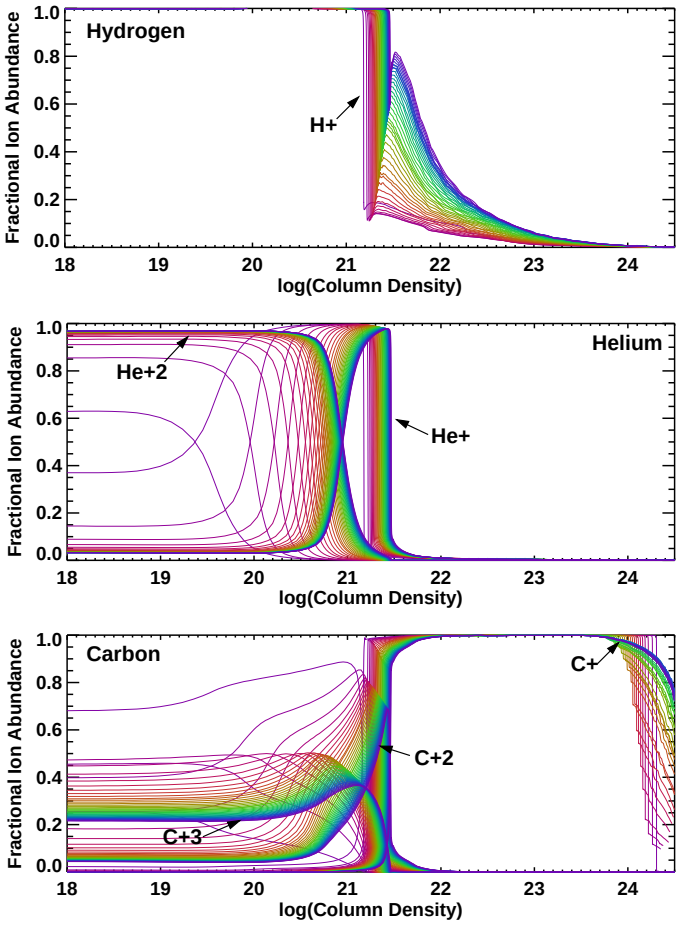

Figure 2.13 The ionization fraction for select ions of hydrogen, helium and carbon as a function of column density for the semi-empirical SEDs. We assume $\log U = -2$, $\log n_H = 10$, and $\log N_H = 26$ for illustration. Red lines corresponds to lower values of kT (soft continua), and blue corresponds to higher values of kT (harder continua). Notable differences include a deeper partially-ionized zone for hydrogen for the harder continua, deeper He I region but shallower He II region for the softer continua, and overall low ionization at small column density for softer continua.

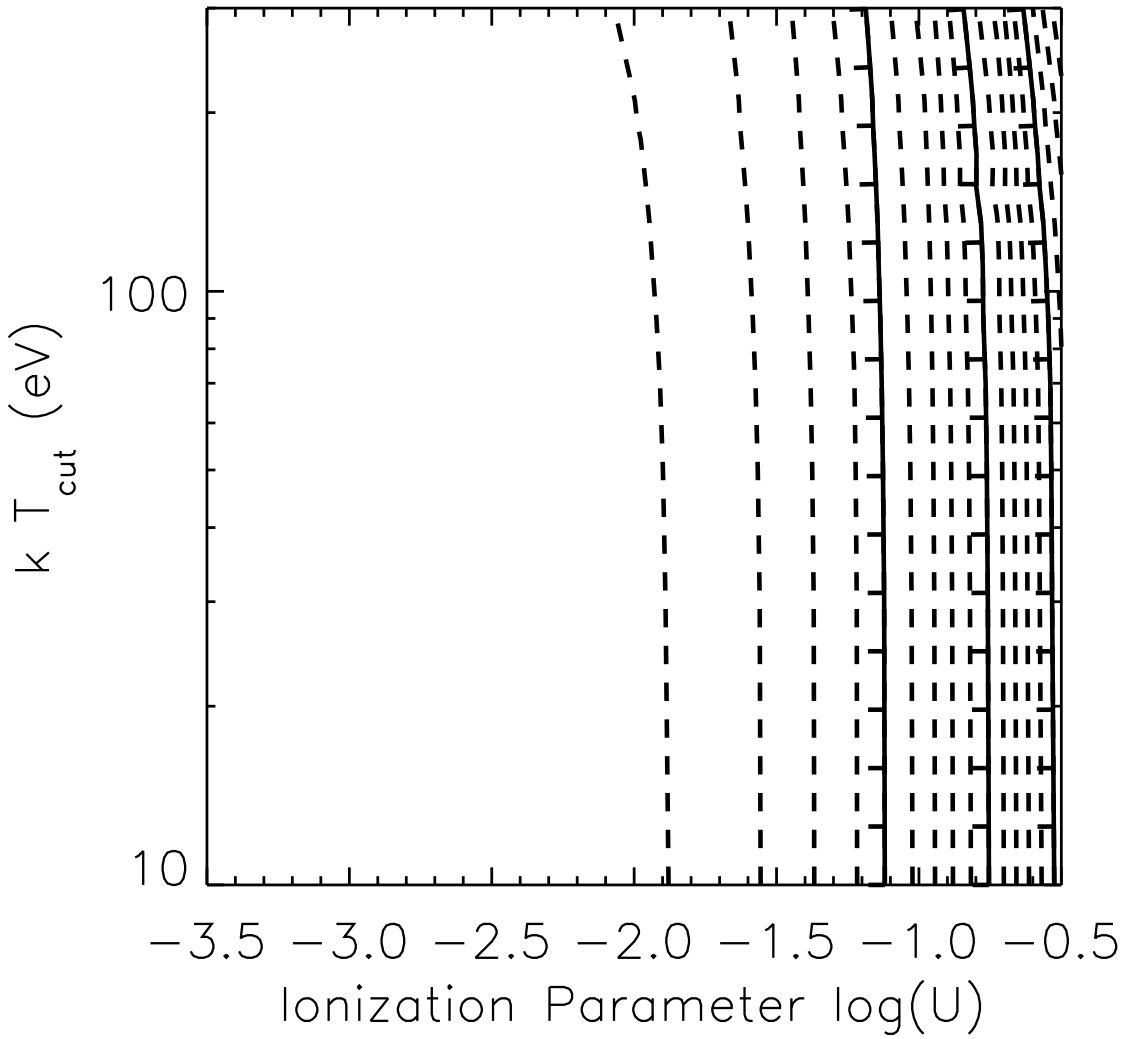

Figure 2.14 The contours of Lyα flux as a function of $\log(U)$ and kT. This shows that Lyα flux is almost independent of spectral energy distribution, as expected. By dividing other line flux values by the Lyα, we can partially remove the ionization parameter dependence.

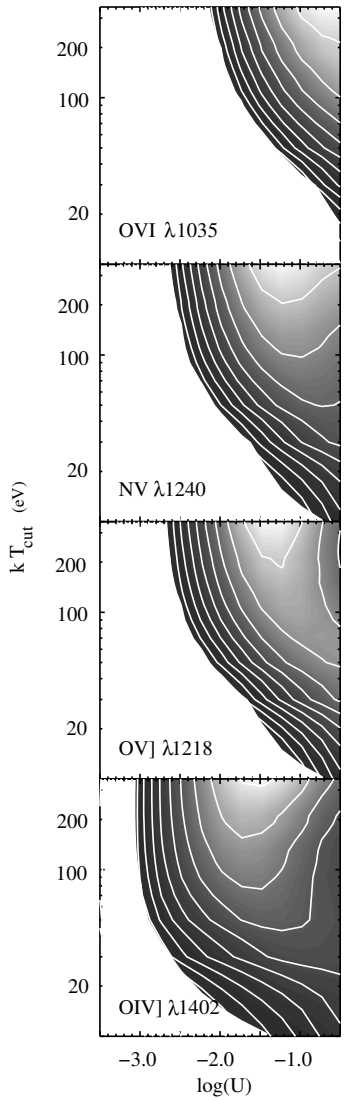

Figure 2.15 Ratios of lines from ions with I.P. $> 54.4\,\mathrm{eV}$ with Lyα. Shading shows the whole range for each emission line; contours increase by a factor of 1.25. The density for these simulations is $n_H = 10^{10}\mathrm{cm}^{-3}$.

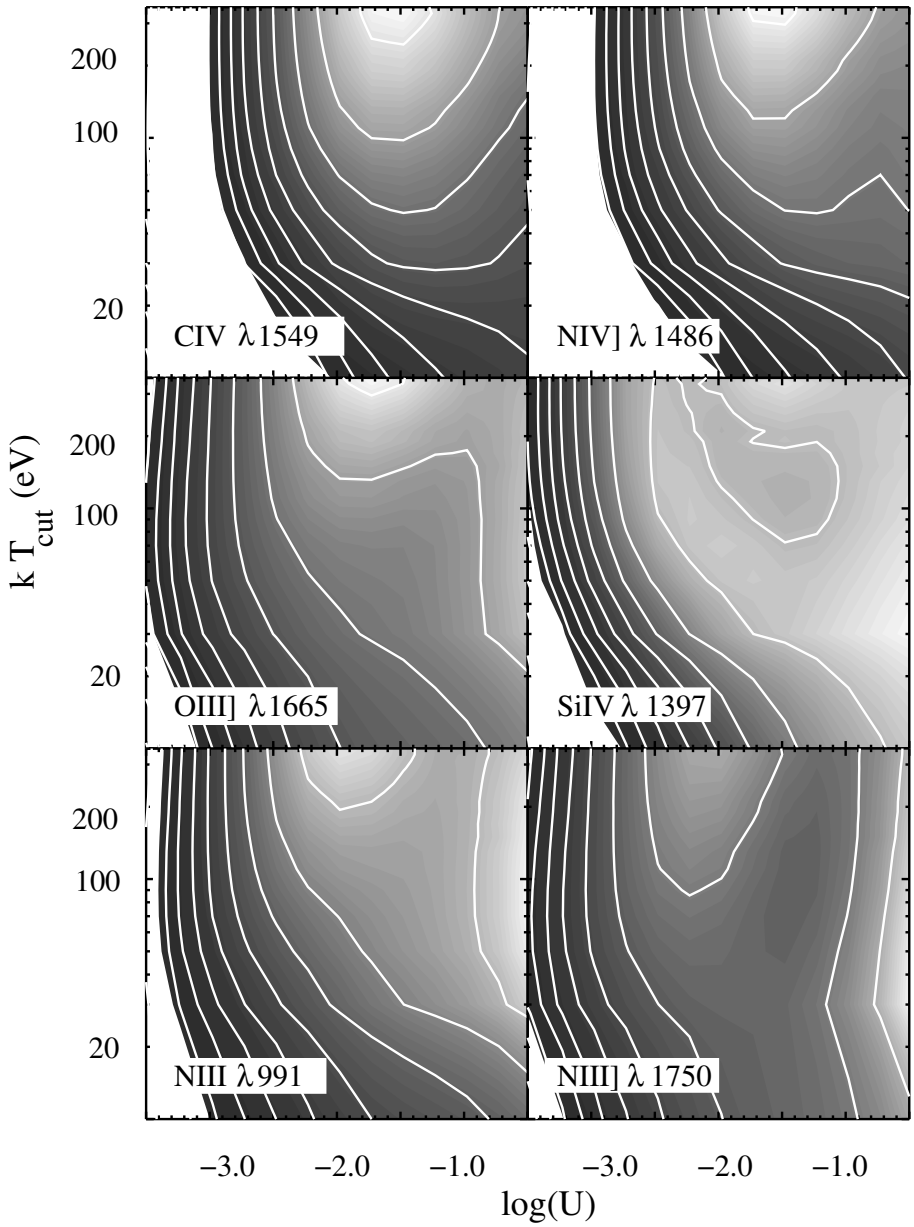

Figure 2.16 Ratios of lines from ions with 13.6 < I.P. < 54.4 eV with Lyα.

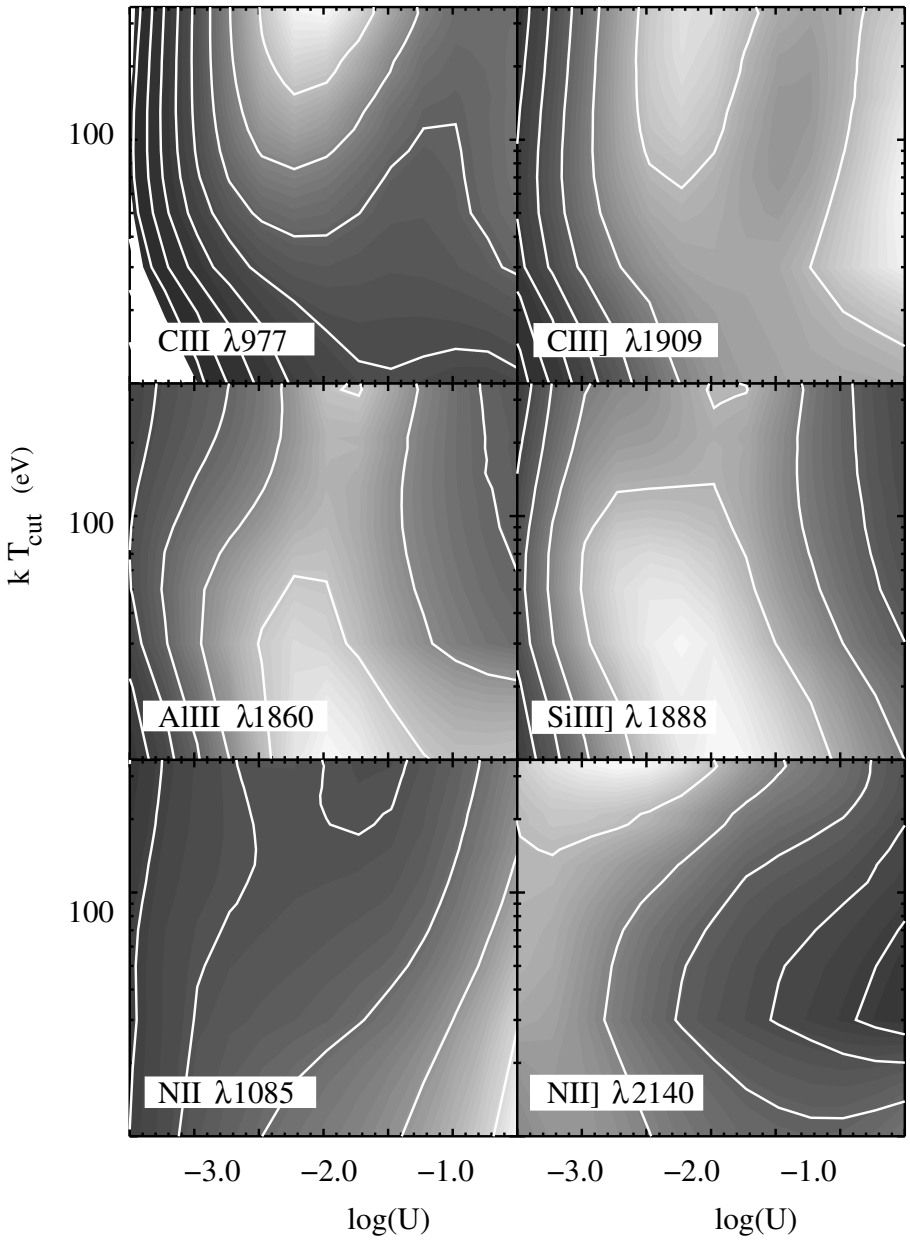

Figure 2.17 Fig. 16 continued.

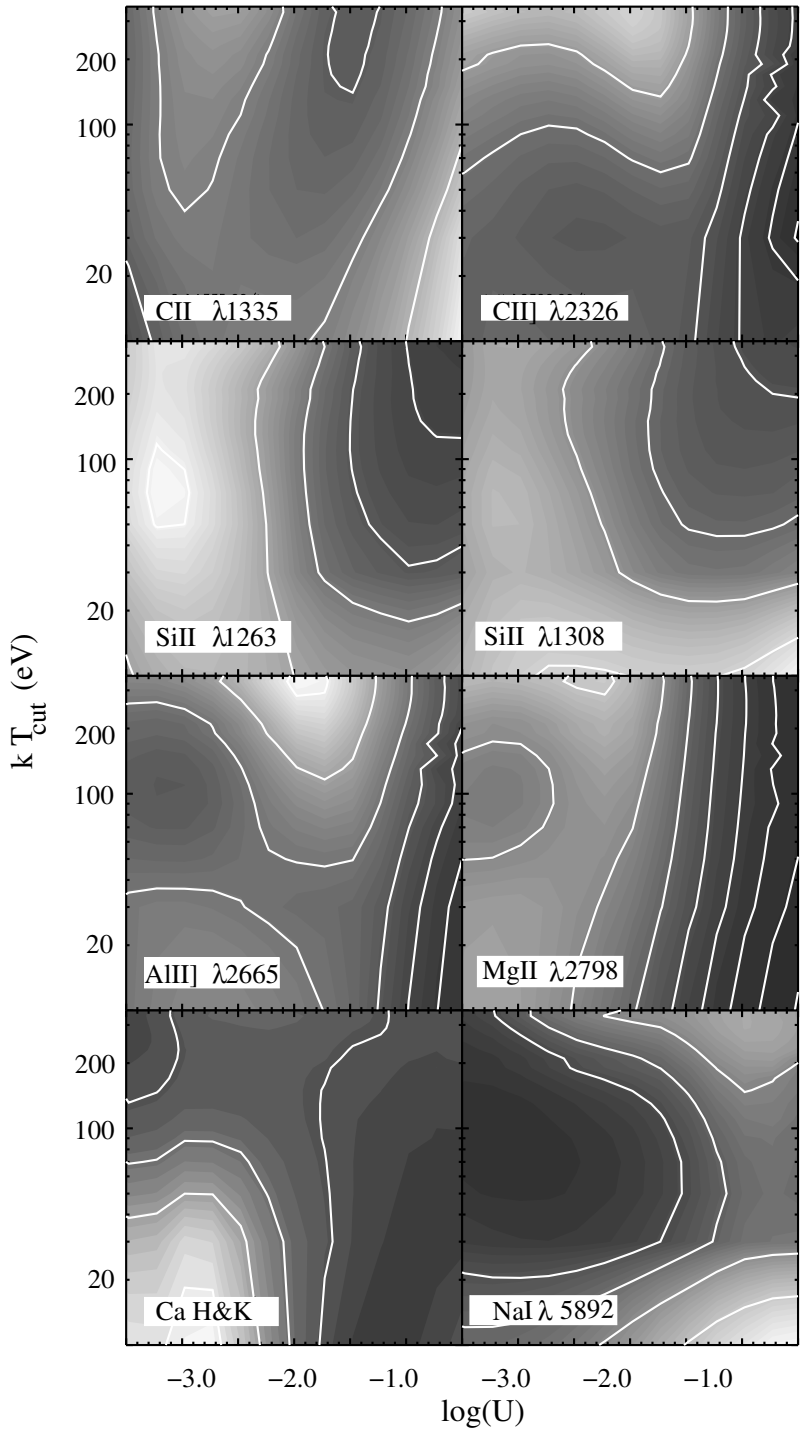

Figure 2.18 Ratio of lines from ions with I.P. $< 13.6\,\mathrm{eV}$ with Lyα.

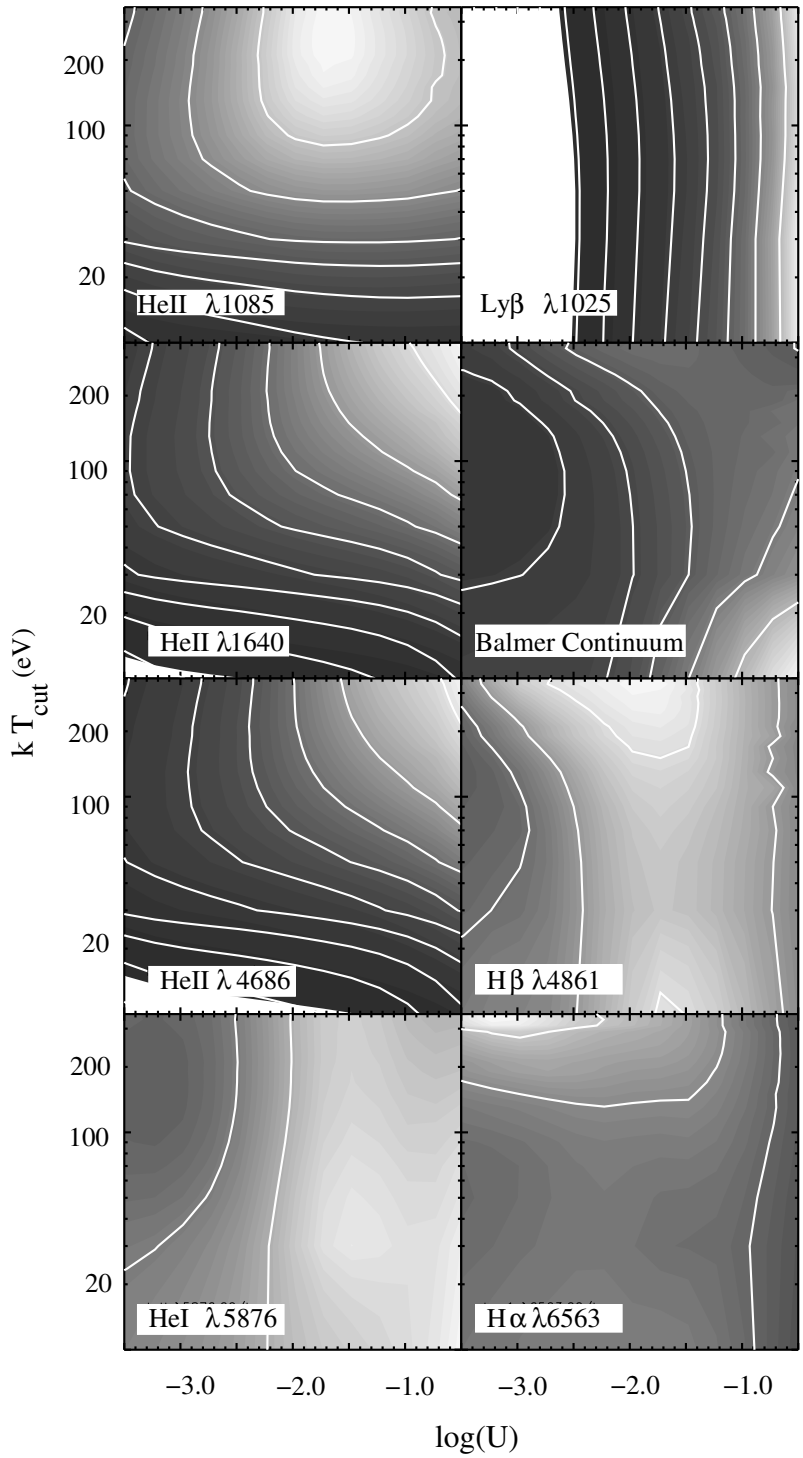

Figure 2.19 Ratio of recombination lines with Lyα.

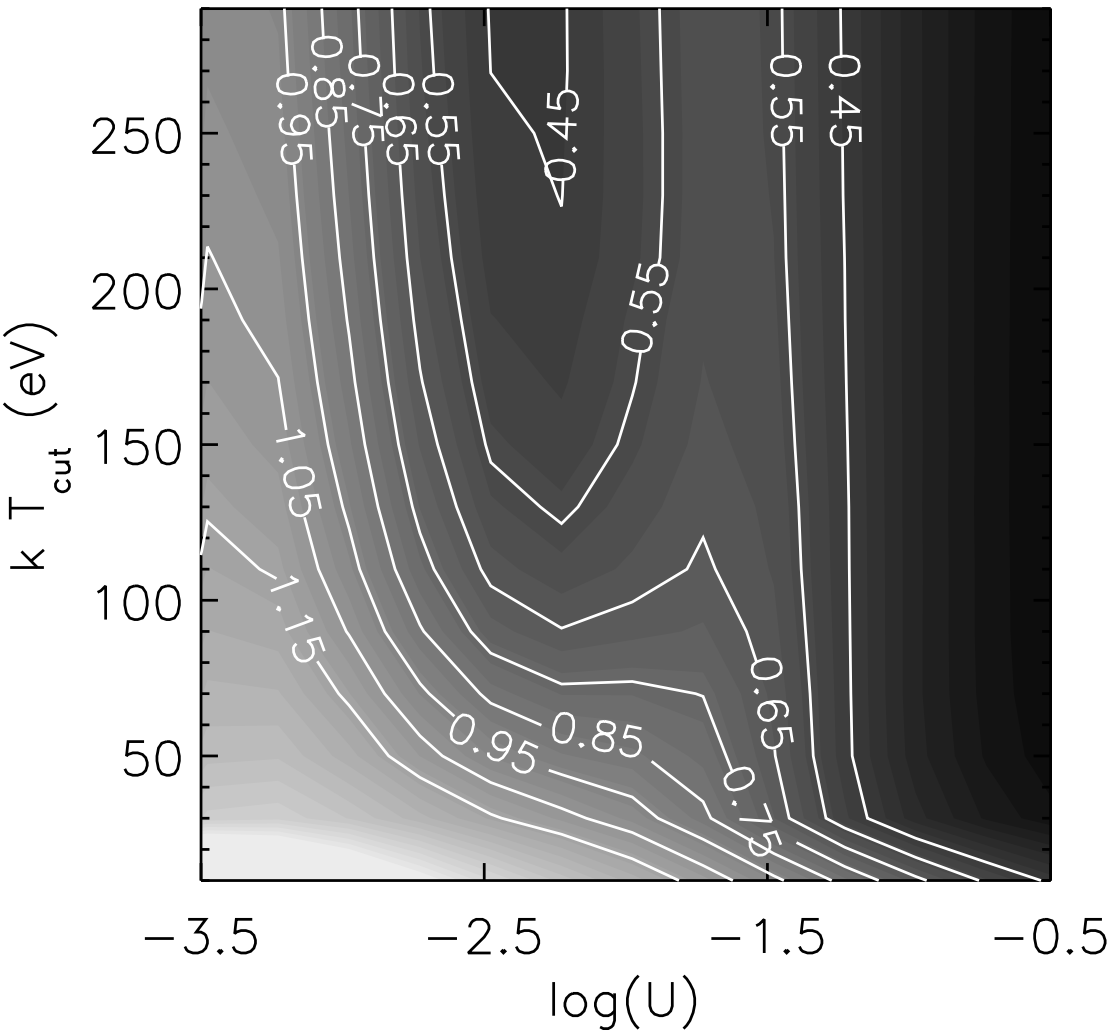

Figure 2.20 Contours for the density indicator Si III]/C III]. Significant variations in the kT_{cut} direction indicate that Si III]/C III] is not independent of the spectral energy distribution.

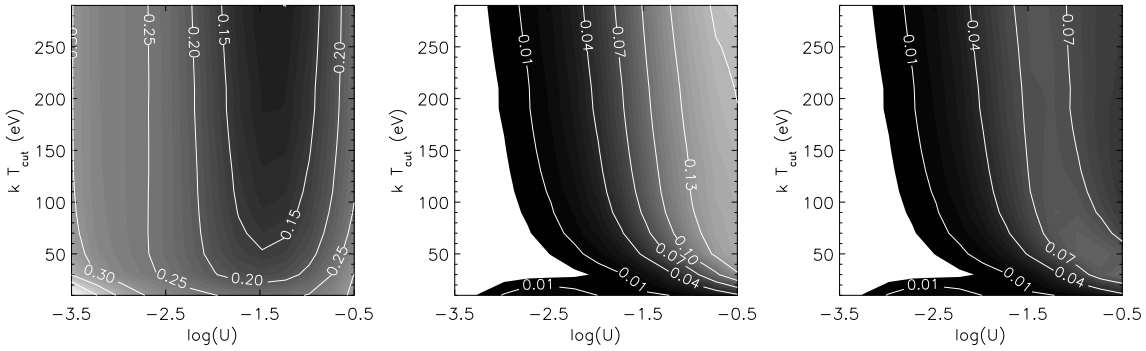

Figure 2.21 Contours for the metallicity indicators. Left: N III]/O III]; middle: N V/C IV; right: N V/(O VI+C IV). Variations in the kT_{cut} direction reveal that the metallicity indicators are not robust for the softest spectral energy distributions.

Table 2.1. Observing Log

Observatory	Date	Bandpass	Exposure (seconds)
FUSE	2000 April 30 20:50:43 – 2000 May 3 02:32:18	905–1187 Å	43,640
ASCA	2000 May 1 00:14–12:37	0.6–10 keV (SIS)	15,700
		0.8–10 keV (GIS)	17,500
EUVE	2000 April 1:27:59 – 2000 May 2 20:57:59	0.15 keV	63,700
HST FOS	1997 January 31	G130H (1140–1605)	4,420
		G190H (1575–2330)	2,460
		G270H (2220–3300)	670

Table 2.2. Spectral parameters in the X-ray band

Correction[a]	Photon index (Γ)	PL Norm.[b]	kT(keV) [c]	BB Norm.[d]	χ^2_ν/d.o.f
Without	$2.28^{+0.18}_{-0.20}$	$6.4^{+1.3}_{-1.2}$	0.152±0.017	1.3 ± 0.3	1.13/149
With	$2.35^{+0.17}_{-0.16}$	$7.1^{+1.1}_{-1.1}$	0.122±0.014	3.4 ± 0.9	1.13/138

[a]Correction for SIS data included or not.

[b]The power-law normalization in units of 10^{-4} photons cm^{-2} s^{-1} keV^{-1} at 1 keV in the source rest frame.

[c]The blackbody temperature in the source rest frame.

[d]Source luminosity in units of 10^{34} ergs s^{-1} assuming it is located at 10 kpc. The luminosity distance is 190.2 Mpc using cosmological parameters of $H_0 = 70$ km s^{-1} Mpc^{-1}, $\Lambda_0 = 0.70$, and $\Omega_M = 0.3$.

Table 2.3. Prominent Emission Line Measurements

Emission Line	measured λ(Å)[a,b,c]	Laboratory λ (Å)[a]	FWHM (km s^{-1}) [d]	F(10^{-14} ergs s^{-1}cm^{-2})[c]	W_λ (Å)
C III	977.4 ± 0.2	977.0	1170 ± 540	1.6 ± 0.3	4.1
Lyβ	1028.3 ± 1.2	1025.7	1220 ± 620	0.20 ± 0.12	0.5
O VI	1031.7 ± 0.06	1031.9	1300 ± 140	11.2 ± 1.0	28.8
Lyα	1215.9 ± 0.02	1215.7	790 ± 20	22.2 ± 0.6	49
O V]	1218.3 ± 0.2	1218.3	1020 ± 130	6.5 ± 0.8	14.4
N V	1239.4 ± 0.2	1238.8	900 ± 120	2.6 ± 0.3	5.8
	1243.4 ± 0.2	1242.8	900 ± 120	1.4 ± 0.2	3.1
C II	1334.4 ± 0.3	1334.5	300 ± 90	0.7 ± 0.5	1.6
O IV]	1399.7		1120 ± 70	0.09 ± 0.06	0.23
	1401.2		1120 ± 70	0.51 ± 0.06	1.3
	1404.8		1120 ± 70	0.14 ± 0.06	0.31
	1407.3		1120 ± 70	0.09 ± 0.06	0.20
Si IV	1393.8 ± 0.3	1393.8	1120 ± 70	1.33 ± 0.22	3.0
	1402.8 ± 0.3	1402.8	1120 ± 70	1.37 ± 0.47	3.0
C IV	1548.0 ± 0.08	1548.2	900 ± 30	7.9 ± 0.4	14.4
	1550.5 ± 0.08	1550.8	900 ± 30	8.4 ± 0.5	15.2
He II (blueshifted)	1637 ± 0.1[e]	1640.4	700 ± 140	1.0 ± 0.2	1.8
He II	1640.7 ± 0.1	1640.4	570 ± 60	2.7 ± 0.3	5.0
O III]	1661.0 ± 1.4	1660.8	810 ± 40	0.45 ± 0.21	0.8
	1666.3 ± 0.7	1666.2	810 ± 40	1.0 ± 0.18	1.8
N III]	1751.0 ± 0.5	1750.4	810 ± 40	0.62 ± 0.13	1.1
Si III]	1892.3 ± 0.3	1892.0	760 ± 130	1.18 ± 0.15	2.1
C III]	1909.1 ± 0.08	1908.7	810 ± 40	4.45 ± 0.16	8.1
Mg II	2796.4 ± 0.3	2796.4	740 ± 70	1.0 ± 0.09	5.0
	2803.6 ± 0.3	2803.5	740 ± 70	1.4 ± 0.10	7.0

[a] Vacuum wavelengths for $\lambda < 3000$Å; Air wavelengths for $\lambda > 3000$Å.

[b] No entry in this column means that the wavelengths were fixed at the laboratory wavelength for the purpose of deblending weak lines.

[c] Repeated uncertainties in these column mean that the flux ratios were constrained in the fitting.

[d] Repeated values in this column mean that the widths were constrained to be equal in the fitting.

[e] A blueshifted component was observed on He II; this is the central wavelength of that component.

Table 2.4. Emission Line Comparison

Emission line[a]	RE 1034+39 Relative Flux	Relative Flux		
		Francis	Zheng[a]	Brotherton
Lyβ+O VI	102[c]	9.3	16.0	11.6
Lyα+N V feature	118	100		100
Lyα	100		100	
N V	18.0		14.0	
1400 Å feature	15.9	19	8.1	6.8
He II	16.8[b]	18[d]	3.4	5.2[d]
C IV	73	63	52	27
1900 Å feature	25.4	29		10
Al III	0.0		2.9	
Si III]	5.3		2.8	
C III]	20.0		12	
Mg II	10.8	34	33	13

[a]Radio-quiet quasars.

[b]Sum of blueshifted and rest frame components..

[c]Assuming that the 1037Å and 1031Å lines have the same flux (optically thick). The value would be 77 if the lines have 2:1 ratio (optically thin).

[d]He II λ1640+O III] λ1666.

Table 2.5. LOC model results

Emission Line	Baldwin [a,b]	Baldwin Re-created[a,c]	RE 1034+39 SED [a]	RE 1034+39 (measured)[a]
O VI λ1032 + Lyβ	0.16	0.19	0.52	0.51
Lyα	1.0	1.0	1.0	1.0
N V	0.04	0.067	0.18	0.18
O IV]+Si IV	0.06	0.05	0.17	0.16
C IV	0.57	0.54	1.11	0.73
O III] + He II λ1640	0.14	0.16	0.25	0.11[d]
Mg II	0.34	0.29	0.47	0.11

[a]Flux ratios with respect to Lyα.

[b]The results taken from Baldwin et al. 1995.

[c]Our re-creation of the Baldwin et al. (1995) results.

[d]Only narrow, restframe component of He II is included.

Chapter 3

A Self-Consistent NLTE-Spectra Synthesis Model of FeLoBAL QSOs

3.1 Introduction

We test the ideas of Branch et al. (2002) and Casebeer et al. (2004) by using the generalized stellar atmosphere code `PHOENIX` to model the spectra of the two FeLoBALs that were successfully modeled using SYNOW, and including spectra that extend to rest-frame optical wavelengths for FIRST J121442+280329. `PHOENIX` is a much different code than `SYNOW` in that it contains all the relevant physics to determine the spectrum of outflowing gas. It solves the fully relativistic NLTE radiative transfer problem including the effects of both lines and continua in moving flows. For a discussion of the use of both `SYNOW` and `PHOENIX` in the context of modeling supernovae spectra, see Branch, Baron, & Jeffery (2003). We find that `PHOENIX` is able to model the spectra from these objects surprisingly well, and we are able to derive several important physical parameters from the model.

In §3.2 we describe the `PHOENIX` model in detail. In §3.3 we describe our determination of the best-fitting model. In §3.4 we describe the results of our model fitting. In §3.5 we discuss the physical implications of the model, how it relates to other BAL spectra and where it fits in the BAL picture. An appendix includes a flowchart of a `PHOENIX` calculation.

3.2 Models

Photoionization codes have been essential in understanding emission and absorption features in the spectra of active galaxies. *Cloudy* (Ferland et al., 1998) is the most commonly used

one; however, it is not the only code in existance, and is not universally the best code to use in all circumstances. In this section, we compare and contrast `PHOENIX` and *Cloudy*, pointing out their similarites and differences in their computational structure, input parameters, and output products. Our approach in this section is simple and approximate; a more detailed and technically correct discussion of `PHOENIX`, including many references, is included in the Appendix.

As discussed in the classic review article by Davidson & Netzer (1979), a photoionization code solves essentially two sets of problems. The first set are the ionization balance equations. These describe the number density of each ion and the next state as a function of the ionizing flux and the recombination rate. The second set are the thermal balance equations. The photoelectron has energy that adds heat to the gas. The photoelectrons cause collisional excitation that can cause collisionally excited line emission. These equations are coupled through the electron density (check). The equations are solved on a grid that is a function of depth into the slab of gas, as the characteristic ionization state of a gas decreases with depth as photoionizing photons are depleted from the incident continuum. The solution as a function of depth is typically iterated several times until it coverges. For more details, see the *Cloudy* manuals *Hazy*[1] and Ferland et al. (1998).

Cloudy self consistently computes the photon emission at any point in the gas slab. But that is not what the observer sees: the photon must escape to the surface to be seen. This is the radiative transfer, which involves another entire set of equations describing the interaction of the photon with matter as it tranverses the gas. Computationally, the principal difference between *Cloudy* and `PHOENIX` is the treatment of radiative transfer. `PHOENIX` solves the raditive transfer equations exactly; *Cloudy* currently uses an approximation known as

[1]The *Cloudy* manuals are available with the source code distribution at `http://www.nublado.org/`.

the escape probability method to compute the continuum and line transfer. As noted in the *Hazy* manual for *Cloudy* "This (escape probabilities) is probably the weakest assumption in the present prediction of the spectrum." A classic discussion of the errors inherent in the escape probability method is found in Avrett & Loeser (1988); it is also discussed in the context of X-ray spectroscopy by Dumont et al. (2003).

The escape probability method is expected to be valid under conditions where the photon escapes without interaction or minimal interaction with the gas. For nebular conditions, i.e., optically thin to the continuum (e.g., planetary nebulae), the escape probability method may produce very similar results as exact radiative transfer. It is expected to fail in cases where the gas is optically thick to the continuum, especially, for example, in the partially-ionized zone in active galaxies. Why doesn't *Cloudy* use exact radiative transfer? Exact radiative transfer is a planned improvement for *Cloudy* (Ferland, 2000a). It should be noted, however, that one of the advantages of *Cloudy* is that it runs very fast; models can be computed in a matter of seconds. Adding radiative transfer slows a code down considerably; that is one reason why `PHOENIX` is run on supercomputers, and whereas work using *Cloudy* will investigate results from tens to hundreds of thousands of simulations Leighly (2004b); Leighly & Casebeer (2007, e.g.,), work done using `PHOENIX`, such as that presented here, may involve only hundreds of successfully converged simulations as a matter of practicality.

`PHOENIX` has two other advantages over *Cloudy*. While the *Cloudy* atomic database is very large, and complete and accurate atomic data is one of the strengths of the code, the atomic database for `PHOENIX` is even larger. As an example of the differences in the atomic data, we include the properties of Fe^{+} and Fe^{+2} atoms in *Cloudy*, `PHOENIX`, a version of *Cloudy* used by Verner et al. (2003), and an iron model used by Sigut & Pradhan (2003) and

Sigut et al. (2004) (Table 3.1). This table also details the type of radiative transfer used in the code, and whether or not the thermal equilibrium is solved or not (specifically, Sigut & Pradhan (2003) and Sigut et al. (2004) determine the ionization equilibrium using *Cloudy*, and then solve the radiative transfer, so their computation is not entirely self-consistent). As can be seen in this table, `PHOENIX` has the most complete atomic database in Fe^{+} and Fe^{+2}, and that carries over to other ions as well. This is important for modeling FeLoBALs because of the large number of iron absorption lines.

The second additional advantage of `PHOENIX` involves its handling of relative motion in the emitting and absorbing gas. Relative motion influences radiative transfer because it effectively changes the wavelength dependence of the opacity. For example, if a parcel of gas adjacent to an emitted photon is moving significantly with respect to that photon, that photon will see reduced line opacity. *Cloudy* can handle turbulence, and the influence of turbulence on AGN broad line emission has been discussed by Bottorff et al. (2000). The limitation of *Cloudy* is that turbulence is handled by convolving a Gaussian of the width of the turbulence with the thermal line profile; this is the only mechanism available in *Cloudy* to handle relative motions in a gas. In contrast, `PHOENIX` can handle any input velocity field. This distinction is important, especially when lines are overlapping, because reduced opacity toward both higher and lower wavelengths (as assumed if the turblence is modelled as a gaussian) will produce a different spectrum than if the opacity is reduced only toward higher wavelengths, as is appropriate in the outflow scenario discussed in this paper.

In this paper we model the situation envisioned by Branch et al. (2002): the emission and absorption occur in a fairly optically thick expanding shell illuminated from the inside by the continuum; as discussed in §5.4, this situation may be a consequence of quasar evolution, occuring when the quasar ejects a shroud of dust and gas (Voit et al., 1993, e.g.,). `PHOENIX`

treats this situation better than *Cloudy* can because it is very optically thick and exact radiative transfer is likely to be important, because there are many overlapping transitions, especially from Fe II, so a large atomic database is important, and because the relative velocity in an outflow is an expansion rather than a turbulence.

We finally note that there is one additional important difference between *Cloudy* and `PHOENIX`, and that is in the input and output. The *Cloudy* output includes of lists of lines and opacities, and the observed spectrum must be constructed from these by the user of the code. In contrast, `PHOENIX` is a spectral synthesis code; the direct output is a model spectrum. The only way to obtain fluxes or equivalent widths of lines in a `PHOENIX` model is to measure them directly from the synthetic spectrum in the same way that they are measured from the observed spectrum. Measuring emission and absorption lines from complex quasar spectra is well known to be rather uncertain, as a consequence of blending and uncertain placement of the continuum. So in `PHOENIX`, this step is bypassed, and the synthetic spectrum is compared directly with the observed spectrum. Second, the input parameters are somewhat different. The principle input parameters of *Cloudy* are the ionization parameter, which is the ratio of the photoionizing flux and the density, and the column density. In `PHOENIX`, density is given as a function of the radius in concordance with the assumed velocity profile as a function of radius. An analogy to the photoionizing flux is a little difficult to construct. As noted in the next section, two of the important parameters are the reference radius R_0, which is the radius where the continuum optical depth at 5000Å is unity, and the model temperature T_{model}, which is defined in terms of the luminosity L and the reference radius as a blackbody. Thus, L or T are somewhat analogous to the photoionizing flux, because for a fixed reference radius, they give the intensity of the continuum at the reference radius. Finally, the column density can be evaluated for particular values of the optical depth.

Table 3.1. An Example Comparison of Models

Model	Fe^{+} atom (levels / energy / lines)[a]	Fe^{+2} atom (levels / lines)	Radiative Transfer	Thermal Equilibrium
Cloudy	371 / 11.6eV / 68,635	no UV lines	local escape prob.	yes
Verner et al. 2003	830 / 14.06 eV / 344,035	no UV lines	local escape prob.	yes
Sigut & Pradhan 2003	830 / $\sim$ 15 eV / 23,000	no lines	exact	no[b]
Sigut, Pradhan & Nahar 2004	285 / $\sim$ 7 eV / 3892	581 / 10,885	exact	no[b]
PHOENIX	617 / 14.81 eV / 13,675	566 / 9,721	exact	yes

[a]Number of levels in the model atom / the energy of the highest level / the number of NLTE transitions.

[b]Sigut and collaborators obtain their temperature structure from *Cloudy* before doing the radiative transfer, so their model is not thermally self-consistent.

3.2.1 The Model Parameters

Our models are spherically symmetric, with homologous expansion ($v \propto r$). Homologous expansion is analogous to the Hubble expansion. The model atmospheres are characterized by the following parameters (see Baron et al., 2004, for details): (i) the reference radius R_0, which is the radius where the continuum optical depth in extinction ($\tau_{\rm std}$) at 5000Å is unity; (ii) the model temperature $T_{\rm model}$, which is defined by means of the luminosity, L and the reference radius, R_0, [$T_{\rm model} = (L/(4\pi R_0^2 \sigma))^{1/4}$], where σ is Stefan's constant; (iii) the density structure parameter v_e, [$\rho(v) \propto e^{-v/v_e)}$]; (iv) the expansion velocity v_0, at the reference radius; (v) the pressure, P_{out}, at the outer edge of the atmosphere; (vi) the LTE-line threshold ratio, equal to 5×10^{-6}; (vii) the albedo for line scattering (metal lines only, here set to 0.95); (viii) the statistical velocity $\zeta = 50$ km s^{-1}, treated as depth-independent isotropic turbulence, and (ix) the elemental abundances are solar as given by Grevesse & Noels (1993).

We emphasize that for extended model atmospheres one should not assign, *a priori*, a physical interpretation to the parameter combination of $T_{\rm model}$ and R_0. While $T_{\rm model}$ has a well defined physical meaning for plane-parallel stellar atmospheres, its definition for extended atmospheres is connected to the particular definition of the radius R_0 (see Baschek et al., 1991). In addition, the reference radius R_0 in our models is defined using an extinction optical depth scale at $\lambda = 5000$Å and is not directly comparable to observationally derived radii. Therefore the model temperature is not well defined for extended atmospheres and must be regarded only as a convenient numerical parameter. We chose the maximum extinction optical depth so that model would be just optically thick to continuum scattering in order to replicate the optical spectrum observed in these objects.

3.2.2 Comparison of our model with de Kool et al. (2002)

The de Kool et al. (2002) approach

Because we want to compare and contrast our model with de Kool et al. (2002) we must first briefly describe their analysis. We repeat the description of their analysis from Branch et al. (2002) here. In their analysis, de Kool et al. (2002) used effective continuous spectra that consisted of a power-law continuum plus Fe II and Mg II BELs. The Mg II BEL was the sum of two Gaussians centered on the two components of the Mg II λ2798Å doublet (λ2796Å, $\lambda 2803\mathring{A}$). Two different templates for the Fe II BELs were considered. The first consisted of a linear combination of five sets of Fe II BELs from theoretical model calculations (Verner et al. 1999), and the second was the observed Fe II BEL spectrum of the strong emission-line QSO 2226–3905 (Graham et al., 1996). For the absorption features, de Kool et al. (2002) obtained a template distribution of line optical depth with respect to velocity in the BALR from the observed absorption profile of Fe II λ3004Å, an apparently unblended line

of moderate strength. Given the assumption that only absorption takes place in the BALR, the optical depth was obtained from $\tau(\mathrm{v}) = \log \mathrm{F}_\lambda$, where F_λ is the fractional residual flux in the absorption feature. The resulting optical depth distribution extended from about 1200 to 2700 km s^{-1} and peaked near 2100 km s^{-1}. This optical depth distribution, scaled in amplitude, was used for all absorption lines. For each of the absorbing ions that were introduced Fe II, Mg II, Cr II, and Mn II the column density was a fitting parameter. The relative strengths of the lines of each ion turned out to be consistent with LTE.

Three models that differed in their details (de Kool et al., 2002) were presented, with similar results. The column densities of Fe II, Cr II, and Mn II were well constrained. (The column density of Mg II could not be well constrained because the only Mg II absorption, due to λ2798Å, is saturated.) The excitation temperature was found to be near 10,000 K. Two local covering factors, representing the fractions of the power-law source and the BELR that are covered by the BALR as viewed by the observer, were introduced to reproduce the observed nonblack saturation the fact that in the observed spectrum, even very strong absorption features do not go to zero flux. Both local covering factors were found to be 0.7 ± 0.1.

A detailed view of the spectral fit for one of the models was presented, and practically all of the observed absorptions were reasonably well accounted for. To further interpret the results of FIRST J121442.3+280329. of their spectrum fits, de Kool et al. (2002) then used the photoionization–equilibrium code CLOUDY to compute a grid of constant-density slab models irradiated by a range of ionizing spectra. The ionization parameter U, the hydrogen density n and the hydrogen column density N were found to satisfy $2.0 < \log \mathrm{U} < 0.7$, $7.5 < \log \mathrm{n} < 9.5$, and $21.4 < \log \mathrm{N} < 22.2$, respectively. From these values, the distance of the BALR from the center of the QSO was inferred to be between 1 and 30 pc.

The PHOENIX approach

The PHOENIX model is a very detailed model, calculated from first principles. We compare it with the rather simplified, template fitting approach of de Kool et al. (2002) (see also: Korista et al., 1992; Arav et al., 2001; de Kool et al., 2001) and discuss differences in the approaches. For a more complete understanding of PHOENIX we suggest that the reader explore the information in the Appendix.

In contrast to the approach by de Kool et al. (2002) we model the continuum, the emission lines, and the absorption lines simultaneously. The Fe II emission lines in our model are calculated self-consistently using our rather sophisticated model atom. The velocity width of the emission lines is determined by the outflow characteristics. In fact, the radiative transfer through the moving clouds is what gives the lines their width and therefore the calculations from the model are directly comparable with the observed spectrum. In addition we have run in excess of 100 models during the fitting process fitting the continuum, emission and absorption line features simultaneously, compared with the linear combination of the five calculations run with the sophisticated CLOUDY models in the de Kool et al. (2002) approach. None of our models are based on observed emission line spectra and as such we do not have the problems associated with the correct placement and removal of the continuum.

We have none of the fitting parameters associated with the emission line fits displayed in de Kool et al. (2002). We rely on a global fit to the overall spectrum from a model calculated from first principles, to determine how our model compares with observation.

Our approach does not use a template fit to the absorption line spectrum $\tau(\mathrm{v}) = \log \mathrm{F}_\lambda$. In our model the spectrum is calculated directly from self-consistently solving the radiative transfer problem with scattering in an expanding atmosphere from first principles. Our

optical depth profile as a function of velocity is determined based on the physical conditions of the gas and the radiation field at a given velocity, not on the actual spectrum of the object *a priori*.

Our model grid is specified in terms of $\tau_{\rm std}$ and the spatial extent is then determined by the implicit condition that $\tau_{\rm std}$ (R_0)= 1.0. Thus, the inner and outer spatial boundaries are determined by the input $\tau_{\rm std}$ grid and vary not only from model to model but within a given model from iteration to iteration as we reach convergence. Given the density parameterization, the pressure and temperature are determined by the NLTE equation of state from iteration to iteration. The models are very well converged. Thus, in contradistinction to template fitting of de Kool et al. (2002) since we do not have a spacially fixed inner boundary and the $\tau_{\rm std}$ grid is fixed we do not have a-priori a fixed ionization parameter or column density.

3.3 Determining the Best Fit Model

In order to find the appropriate model parameters we began with the parameters of Branch et al. (2002) (v_{max} = 2800km s^{-1}, v_{phot} = 1000km s^{-1}, t_{bb} = 8000 K, t_{exc} = 10000 K) and restricted our initial calculations to pure LTE, which is much less computationally demanding and hence allows us to produce large grids which are then calculated in full NLTE. Given an LTE grid, we then chose a subset of "best fit" (by eye) models which we proceeded to calculate in full NLTE. Once we felt subjectively that we had the best model fit we turned to a more objective method of determining the best fit. Over 100 models where run during this process.

3.3.1 Figure of Merit

Determining a goodness of fit criterion for spectra is a non-trivial task. A pure χ^2 method is not ideal because a good fit of a synthetic spectrum to an observed spectrum should ideally fit on all scales. That is, the continuum shape (colors) should be correct as well as all the line features. Since our synthetic spectral models include detailed physics of the interaction of the lines and continua, we strive to fit both. Since we don't know the errors due to flux calibration, reddening, etc., a χ^2 would not have the traditional meaning in terms of probability. Nevertheless we have adopted a χ^2–like method to produce a Figure Of Merit (FOM).

$$FOM = \sum_{\{\lambda\}} [\frac{f_\lambda(model(parameters))/C_{Norm} - f_\lambda(observed)}{0.10 \times f_\lambda(model(parameters))/C_{Norm}}]^2$$

We assumed a relative error of 10This corresponds to the 0.10 in the FOM formula.

We compare the model spectrum with the observation by finding the minimum FOM for a given set of model parameters by iteratively adjusting the the normalization constant ($C_{\rm Norm}$). That is, for the full set of models i we find the best value of C_{Norm} that produces the smallest FOM. This approach allows C_{Norm} to be determined by the fit and thus C_{Norm} is best interpreted as just a fitting parameter without physical content. The model which has the set of parameters with the smallest FOM is the model which we pick as our best fit. It should be emphasized that our grid is a small one in which we "wiggle" our solution by one magnitude in luminosity by adjusting $T_{\rm model}$ in order to see if our models are at a minimum.

3.4 Results

3.4.1 FIRST J121442.3+280329

We first turn our attention to the FeLoBAL quasar FIRST J121442.3+280329 (Becker et al., 2000a; White et al., 2003) UV and optical spectra. We adopted a redshift for FIRST J121442.3+280329 of $z = 0.692$ as measured from the peak the Mg II emission feature. We corrected for a Galactic extinction of $E(B-V) = 0.023$ (Schlegel et al., 1998b) obtained from NED using the reddening curve of Cardelli et al. (1989) supplemented by the work of O'Donnell (1994). We smoothed all observed spectra using a near-gaussian smoothing procedure with a width of 300 km s^{-1}.

The model calculations and fits were done according to the method discussed in section 3.3.1 and the FOM calculations are presented in Table 3.2. Figure 3.1 compares our best-fitting synthetic `PHOENIX` spectrum and the restframe UV spectrum of FIRST J121442.3+280329. The best-fit parameters for FIRST J121442.3+280329 were: $T_{\rm model} =$ 4600 K, $R_0 = 1.4 \times 10^{17}$ cm, $v_e = 300$ km s^{-1}, and $v_0 = 2100$ km s^{-1} (for clarity these values are also shown in Table 3.3).

With this radius and model temperature, the luminosity of the model is $L = 6.3 \times 10^{45}$ ergs s^{-1}. Overall, the synthetic model compares favorably with the restframe UV observation of FIRST J121442.3+280329; in particular the Fe II lines, both from ground and excited states, fit very well. The Mg II λ2798 feature appears to be too strong in emission and yet too weak in absorption. This could be a sign of asymmetry in the atmosphere, Branch et al. (2002) and de Kool et al. (2002) found a similar result in their calculations. However we have not yet explored metallicity or SED effects in our model. Figure 3.2 compares the FIRST J121442.3+280329 rest-frame optical observations to the synthetic

Table 3.2. Grid model results

Object	$T_{\rm model}$ (K)	Radius (cm)	FOM
FIRST J121442.3+280329	4500	1.4×10^{17}	24.4
FIRST J121442.3+280329	4600	1.4×10^{17}	6.2
FIRST J121442.3+280329	4700	1.4×10^{17}	6.9
ISO J005645.1-273816	4500	1.4×10^{17}	25.9
ISO J005645.1-273816	4600	1.4×10^{17}	12.4
ISO J005645.1-273816	4700	1.4×10^{17}	14.1

model. The synthetic model calculation is a reasonable fit to the optical observation. The features at 4600Å are reproduced in the synthetic spectrum, yet are not as strong as the observation and H I absorption appears to be strong in the synthetic spectrum. However, this is dependent on our placement of the continuum and it should be noted that the observed optical spectrum is very "noisy". The observations of Hall (2007) show that absorption features do exist in optical spectra of one FeloBAL QSO which is very similar to the QSOs studied here.

In order to reproduce the optical observation with our model we placed our lower boundary condition (that the specific intensity is given by the solution to the diffusion equation at the inner edge of our opaque core) at the somewhat low value of $\tau_{\rm std} = 10$. Ideally we place that opaque core at $\tau_{\rm std} \gtrsim 100$, but when we did that we found that the model spectrum longward of 2800 Å no longer fit the observation. In particular the optical flux was very attenuated and had deep P-Cygni profiles unlike the observation. FeLoBALs, although very

Table 3.3. PHOENIX best-fitting model parameters.

$T_{\rm model}$	R_0	v_0	v_e	Luminosity
4600 K	1.4×10^{17} cm	2100 km s^{-1}	300 km s^{-1}	6.3×10^{45} ergs s^{-1}

optically thick by AGN standards, are optically thinner than, for example, the atmosphere of a Type II supernova. Models in which the continuum optical depth is high ($\tau_{std} = 100$) fail to reproduce the optical, and the UV spectra redward of Mg II of FeLoBALs.

NLTE effects

This section should be considered as how important it is to correctly model photoionization and recombination in models. Figure 3.3 shows the importance of NLTE effects in correctly modeling spectra. The solid line has all the species that we included in these calculations in NLTE, whereas the dashed line has everything in NLTE except for Ca I-III. For species treated in LTE the Saha-Boltzmann equations are solved in order to calculate the atomic level populations instead of the full rate equations. An LTE treatment of calcium results in under-estimation of the ionization of Ca I in the model which creates a large quantity of Ca II in the line forming region. Therefore the Ca II H&K features appear in the LTE spectrum. When NLTE is turned on for Ca I–III in the PHOENIX model, the level populations are controlled by the hotter radiation field (photoionized) from deeper layers and Ca II is overionized compared to the local gas temperature. Therefore the Ca II H&K features, which are resonance transitions, disappear from the synthetic spectrum. The synthetic model which treats Ca I–III in NLTE closely reproduces the optical observation

whereas the synthetic model without the NLTE Ca I–III clearly overestimates the strength of the H&K lines.

3.4.2 ISO J005645.1-273816

The optical spectrum of ISO J005645.1-273816 was obtained in September 2000 with the FORS1 instrument installed on the VLT UT1/Antu (Duc et al., 2002). We adopted a redshift of $z = 1.776$ which was determined by the C IV, Fe II λ2627 line, and Mg II emission lines. We corrected for an Galactic extinction of $E(B-V) = 0.017$ (Schlegel et al., 1998b) using the standard reddening curve (Cardelli et al., 1989; O'Donnell, 1994). We smoothed all observed spectra using a near-gaussian smoothing procedure with a width of 300 km s^{-1}.

The Mg II feature has a similar shape when compared with FIRST J121442.3+280329 and ISO J005645.1-273816 appears to have similar Fe II features when compared with FIRST J121442.3+280329. Because of the similarities between ISO J005645.1-273816 and FIRST J121442.3+280329 we compare the synthetic model spectrum which fit FIRST J121442.3+280329 with the rest frame UV spectrum of ISO J005645.1-273816. This comparison is shown in Figure 3.4. Following the same fitting procedure outlined in § 3.3 and the same grid of models used for FIRST J121442.3+280329 we found that the parameters which were a best fit for FIRST J121442.3+280329 also were a best fit for ISO J005645.1-273816. The Fe II lines fit very well for this object and the Mg II emission feature was too strong while the absorption was too weak. This is very similar to the fit to the UV spectrum of FIRST J121442.3+280329.

The similarities between the UV spectra of FIRST J121442.3+280329 and ISO J005645.1-273816 are interesting. FIRST J121442.3+280329 and ISO J005645.1-273816 may be a

subtype of FeLoBAL AGN with very similar characteristics. For emphasis, in Figure 3.5 we show the synthetic model spectrum with the combined FIRST J121442.3+280329 UV and optical spectra and the ISO J005645.1-273816 UV spectrum. The high quality fit, over a wide wavelength range, is compelling. It is however unlikely that the PHOENIX models would compare favorably with the total composite spectrum of ISO J005645.1-273816. ISO J005645.1-273816 was discovered in the infrared and the UV spectrum is diminished with respect to the infrared (Duc et al., 2002); however the IR emission could be due to reprocessing by dust outside the region that we have modeled.

3.4.3 Physical Conditions

The physical conditions in PHOENIX are calculated from the constraints of the input physical parameters given in Table 3.3. The PHOENIX model for ISO J005645.1-273816 and FIRST J121442.3+280329 has the following physical dynamics; outflow mass 550 $M_{\odot}$, kinetic energy 30×10^{51} ergs, and a mass loss rate of $\dot{M} = 159$ $M_{\odot}$ yr^{-1} above the "photosphere" ($\tau_{std} = 1$). In addition the PHOENIX model has outflow mass 3000 $M_{\odot}$, kinetic energy 100×10^{51} ergs, and a mass loss rate of $\dot{M} = 466$ $M_{\odot}$ yr^{-1} above $\tau_{std} = 10$. The PHOENIX model has an equivalent hydrogen column density of 2×10^{24} cm^{-2} for the region above the "photosphere" ($\tau_{std} = 1$) and a maximum equivalent hydrogen column density of 2×10^{25} cm^{-2} for the entire atmosphere ($\tau_{std} = 10$). These values are displayed in Table 3.4

3.5 Discussion

The model fits are especially good considering the few free parameters in the PHOENIX model. The reader should keep in mind that we are not fitting each absorption line separately, but rather construct a global fit to the entire spectrum using the parameters given in Table

Table 3.4. PHOENIX Physical Conditions.

τ_{std}	Outflow Mass	Kinetic Energy	$\dot{M}$	Column Density
1	547 $M_\odot$	30×10^{51} ergs	159 $M_\odot$ yr^{-1}	2×10^{24} cm^{-2}
10	3000 $M_\odot$	100×10^{51} ergs	466 $M_\odot$ yr^{-1}	2×10^{25} cm^{-2}

3.3. This includes the absorption, the emission, and the continuum, all fit with these few parameters. In fact, our model spectrum is created by the solution to the radiative transfer equation at every wavelength point across the spectrum simultaneously.

In this section, we discuss some of the physical constraints from these models, how observed polarization in FeLoBALs fits in with this model, provide a few inferences about other FeLoBALs and then discuss some implications for quasar populations and evolution.

3.5.1 Physical Constraints Inferred

Although we have assumed a specific density profile, the radial extension of our model is very small ($v_{max} = 2800$ km s^{-1} and $v_0 = 2100$ km s^{-1}); thus the model does not strongly probe the density structure of the ejecta, except to infer that the density profile is rather flat. Branch et al. (2002) assumed a power-law density profile with $\rho \propto (\frac{v}{v_0})^{-n}$, with $n = 2$, whereas our effective power-law index at the pseudo-photosphere $\tau_{\rm std} = 1$ is $v_0/v_e = 7$, nominally significantly steeper, but since the radial extension of our model is so small the discrepancy should not be considered important. What is perhaps more interesting is that our value of v_0 is quite a bit higher than that of Branch et al. (2002) who used a photospheric velocity of 1000 km s^{-1}. Interestingly, they had to impose a minimum velocity of

1800 km s^{-1} on Fe II and Cr II and they chose the same value of v_{max} = 2800 km s^{-1}. The lower photospheric velocity is likely to be a consequence of the Schuster-Schwarzschild approximation of SYNOW (single T_{exc} in atmosphere); in contrast, PHOENIX allows line formation throughout the atmosphere, and lines typically form in the "line-forming region" ($3.0 < \tau_{\rm std} < 0.1$) depending on their strength. The much lower "photospheric" temperature that we find is robust since SYNOW does no continuum transfer and thus the "temperature" in a SYNOW model is not physically meaningful, it just is a way of parameterizing the underlying continuum. However, PHOENIX solves the full NLTE radiative transfer problem and particularly our result that the Ca II H+K feature is only reproduced in NLTE indicates that we have the right physical conditions in our model.

The synthetic model has $547 M_{\odot}$ and kinetic energy 30×10^{51} ergs above the "photosphere" ($\tau_{std} = 1$). With $R_0 = 1.4 \times 10^{17}$ cm and maximum velocity v_{max} = 2800 km s^{-1} we estimate a crossing time of $t \simeq R_0/v_{max}$ = 15.5 yr. We estimate the mass loss rate using $\dot{M} \simeq M/t$ = 35 M$_{\odot}$ yr^{-1} which is 1/5 the mass loss rate in our PHOENIX model of $\dot{M}$ = 159 M$_{\odot}$ yr^{-1}. The kinetic energy luminosity is estimated at $\dot{E}_k \simeq E_k/t$ = 4.3×10^{43} erg s^{-1} which is two orders of magnitude lower than the bolometric luminosity of the model $L_{bol} = 6.3 \times 10^{45}$ erg s^{-1}; thus the flow could be luminosity driven. Even more interesting is that the velocity we find is very similar to characteristic velocities of hot stellar winds which are thought to be driven by line absorption in the atmosphere (Walborn et al., 1995).

Branch et al. (2002) found a luminosity of 6×10^{46} erg s^{-1} from the photometry of FIRST J121442.3+280329 and using the quasar composite spectrum of Mathews & Ferland (1987) to perform the K-correction and the relation $L_{bol} = 9 \lambda L_{\lambda}$ at 5100Å (Kaspi et al., 2000). Using the quasar composite spectrum of Francis et al. (1991b) we find L$_{\rm bol}$ = 4.4×10^{46} erg s^{-1}

for FIRST J121442.3+280329 and $L_{bol} = 1.7 \times 10^{45}$ erg s^{-1} for ISO J005645.1-273816. Since the spectra are so similar, but the total luminosities inferred differ by a factor of 10, suggesting that the K-correction is important, as it is dependent on the shape of the spectral energy distribution.

Our models have a maximum column density of 2×10^{25} cm^{-2} for the entire atmosphere and a column density of 2×10^{24} cm^{-2} for the region above the "photosphere" $\tau_{std} = 1$. As discussed in §4.1, the larger column density is constrained by our fit to the optical spectrum. A higher column density would produce a larger continuum and line optical depth and therefore more extinction in the optical that is not observed. Thus, the requirement that a photosphere be present places a limit on the minimum column density of 2×10^{24} cm^{-2}, and the optical spectrum places a limit on the maximum column density of 2×10^{25} cm^{-2} of the wind. These constraints make these models Thompson thick, and is sufficient to make these objects appear to be X-ray faint as observed (Green et al., 2001a; Gallagher et al., 2006).

We can now calculate a luminosity distance using a variant of the Spectral-fitting Expanding Atmosphere Method (SEAM) used to derive distances to supernovae (Baron et al., 1995; Lentz et al., 2001a; Baron et al., 1999; Mitchell et al., 2002; Baron et al., 2004). SEAM is a sophisticated variant of the classical Baade-Wesselink method (Baade, 1926). Our approach here differs from the conventional SEAM method in the crucial respect that in the supernova case, we know both that homology is an excellent approximation shortly after the explosion and we know that there was an explosive ejection at a time t_0 (which SEAM determines). Here, homology has been taken to be an expedient Ansatz (this model more closely approaches that of a constant velocity wind, due the the large R_0 and small radial extent, which roughly fixes the value of R_0). There is no reason *a priori* to expect

that FeLoBALs are the result of a single ejection event and thus the radius in our models is much more poorly known than in the case of supernovae. However the radial extent does determine the overall density, and if we were able to identify features which are good density indicators we may be able to place the results of this method on firmer ground. Of course, we are sensitive to systematic errors in the overall flux calibration and in the total reddening. Errors due to reddening tend to cancel out, since the more we must deredden the observed spectrum, the hotter we must make the synthetic spectrum, which compensates for the dimmer observed spectrum.

The SEAM method uses observed photometry and the synthetic spectrum to calculate synthetic photometry as well as K-corrections. From this we find a distance modulus μ which is simply related to the luminosity distance. Using $m_B = 17.06$ for FIRST J121442.3+280329 we find $\mu = 42.56$ or $d_L = 3.25$ Gpc, which compares favorably with the luminosity distance inferred for our adopted cosmology ($\mathrm{H}_0 = 70,\ \Omega_\mathrm{M} = 0.3,\ \Omega_\Lambda = 0.7$) of $d_L = 4.2$ Gpc. Using $m_B = 22.74$ for ISO J005645.1-273816 we find $\mu = 46.59$ or $d_L = 20.8$ Gpc, which is a bit high compared with the luminosity distance inferred for our adopted cosmology $d_L = 13.4$ Gpc. As we noted above, it seems likely that the K-corrections are important and thus we obtain a distance for the relatively nearby FIRST J121442.3+280329 which is good to about 30%, but for the more distant ISO J005645.1-273816 the distance is off by 55%. Nevertheless, that fact that the distances agree to better than a factor of two indicates that our model predicts roughly the right size as well as the right SED for both objects.

Since our `PHOENIX` synthetic spectra are quite a good fit, we may also determine the bolometric luminosity using our synthetic spectra to perform synthetic photometry and calculate K-corrections. With this method we find that $L_{bol} = 1.2 \times 10^{46}$ erg s^{-1} for FIRST

J121442.3+280329 and $L_{bol} = 2.9 \times 10^{45}$ erg s^{-1} for ISO J005645.1-273816.

We obtained L_{bol} in two different ways, both of which where consistent with each other. However the two objects have nearly identical SEDs in the regions that we can observe. Why does the synthetic L_{bol} differ by a factor of 10? The values for R_0 which are the same for the synthetic models must actually differ slightly between the two objects, or, as noted above, the K-correction is important.

We use our model luminosity to estimate a few quantities. If we assume that our model luminosity is the Eddington luminosity then the black hole mass and the accretion rate are $M_E = 5 \times 10^7$ M$_\odot$ and $\dot{M}_E = 1.1$ M$_\odot$ yr^{-1}. These are roughly consistent with usual estimates for quasars, even if we scale the luminosity up by a factor of 3 that we infer from photometry.

3.5.2 Polarization

The studies that have been done regarding polarization (e.g., Lamy & Hutsemékers, 2004, 2000) in which they found that the polarization increases in the absorption troughs, do not rule out the model described in this paper. In fact our model is consistent with the two component model given in Lamy & Hutsemékers (2004) in which the observer looks through a equilateral wind and sees a polar component which is dominated by electron scattering. A spherically symmetric model is a required computational constraint inherent in `PHOENIX`; thus we assume 100% global covering. The polarization results indicate that some asymmetry must be present; nevertheless, the presence of P-Cygni profiles indicate that the covering fraction is high.

Our model will not change much if we relax the 100% global covering fraction and have the same electron scattering polar component described in Lamy & Hutsemékers (2004). In

fact, reducing the covering factor would most likely provide a better fit, as it would reduce the emission feature in Mg II that was shown in §4.1 to be slightly too big.

3.5.3 Other FeLoBAL QSOs

FeLoBALs are observed to have a wide range of spectra. We fit only the spectra of two objects in this paper; in this section, we comment briefly on whether or not the PHOENIX model is likely to be able to explain the spectra of other objects.

Hall (2007) report blueshifted broad absorption lines troughs in Balmer lines in the quasar SDSS J125942.80+121312.6. Our PHOENIX model predicts Balmer absorption in at least Hβ and Hγ as seen in Fig. 2. Thus our model may very well be able to explain the spectra of this object too.

The value of the global covering fraction is very likely to be responsible for the differences between the spectra that we can model, and those of other FeLoBAL QSOs (Hazard et al., 1987; Cowie et al., 1994; Becker et al., 1997; Hall et al., 2002). Specifically, many FeLoBALs appear to have only absorption features, and the emission features are week. The high global covering fraction inherent in the PHOENIX model predicts rather prominent emission features and P-cygni profiles. Reducing the global covering while viewing the outflow from the equatorial region would reduce the emission line strengths while retaining the strong absorption features.

So-called overlapping trough QSOs (Hall et al., 2002) may also be able to be explained by this paradigm. We investigated them with our models and yet where unable to come up with a satisfactory solution, because the emission in our 100% global covering method is too high. Therefore the covering fraction in these type of quasars might be not quite as large as for the objects modeled here. In addition they appear to have higher velocity winds

and possibly higher optical depths.

If the covering fraction is not 100%, then from some lines of sight we may see the nucleus directly. The strong Fe II absorption observed when the outflow is in the line of sight may be seen as as emission in this case, and ultrastrong Fe II emission may be seen. The idea of linking Fe II emission with BAL outflows not in the line of sight has been suggested for the prototypical Narrow-line Seyfert 1 (NLS1) I Zw 1 (Boroson & Meyers, 1992).

3.5.4 Implications for Quasar Populations and Evolution

Broad absorption lines are found in the spectra of 10–20% of the quasars in the Sloan Digital Sky Survey (Trump et al., 2006). The simplest interpretation of this fact is that all quasars have an outflow that occults 10–20% of quasar lines of sight (the orientation model). Alternatively, the outflow may cover a larger percentage of sight lines, and the broad absorption lines may only be present during some small fraction of the quasar lifetime during which it is blowing gas out of the nucleus (e.g., Voit et al., 1993; Becker et al., 2000b; Gregg et al., 2006). As discussed in § 3.2, our model requires a large global covering fraction, although it does not have to be 100%. Here we briefly review the support for both scenarios, and discuss how our results fit into models for quasars in general.

Weymann et al. (1991) compare the emission-line and continuum properties of spectra from 42 BALQSOs with those of 29 normal QSOs. They find that the emission-line and continuum properties are very similar between the BALQSOs and the non-BALQSOs. This result forms a key support for the orientation model. Another important piece of evidence that supports the idea that BALQSOs and non-BALQSOs differ only in their orientation is the fact that X-ray spectra from some BALQSOs are highly absorbed, but apparently intrinsically identical to those of non-BALQSOs (Gallagher et al., 2002).

However, the Weymann et al. (1991) sample is very small, and the number of BALQSOs for which X-ray spectra of sufficient quality to obtain absorption column information is also small. Thus, while the orientation model is widely accepted, and may be applicable to many BALQSOs, the evidence for the evolutionary model, at least for some subclasses of BALQSOs, is growing. The best candidate for objects characterizing the evolutionary model and not fitting into the orientation model are the low-ionization BALQSOs. Early on, these were noted to have optical and UV emission-line and continuum properties different than ordinary quasars (Weymann et al., 1991; Boroson & Meyers, 1992); for example, they tend to have strong Fe II emission and weak O III]. They also tend to be more reddened than non-BALQSOs and HiBALs (Reichard et al., 2003), and they are uniformly more X-ray weak than HiBALs (Gallagher et al., 2006). In addition, they are very rare; Trump et al. (2006) find only about 1% of quasars are LoBALs. Thus, the usual argument used in favor of the orientation model, the similarity of spectra from BALQSOs and non-BALQSOs, doesn't work as well for LoBALs.

Further evidence for an evolutionary role of BALQSOs comes from their radio properties. If BALQSOs were observed predominately edge-on, as are radio galaxies, one would expect to see a steep radio spectrum dominated by the synchrotron emission in the radio lobes. However, BALQSOs show both steep and flat radio spectra (e.g., Becker et al., 2000b). Furthermore, Fe II BALQSOs are extremely rare, and there is evidence among the small sample of an anti-correlation between the radio-loudness and the strength of the BAL features that led Gregg et al. (2006) to propose that quasars in this state are emerging from cocoons of gas that produces the BALs and which suppresses the development of radio jets and lobes. In addition, Brotherton et al. (2006) present spectropolometric results showing polarization parallel to the radio axis, implying a small angle of inclination; they present

an extensive review of the implications of the radio properties on BALQSO models.

Numerous models of quasar evolution admit a time period early in the life of a quasar when it is heavily shrouded by dust and gas. Before we see the bare quasar, we expect to see it in a heavily absorbed stage. Outflows may result from the turning on of the QSO (Hazard et al., 1984). LoBALs may be young quasars that are casting off their cocoons of dust and gas (Voit et al., 1993) and may be related to ultra-luminous infrared galaxies (Egami, 1999). Becker et al. (1997) suggest that FeLoBALs may be the missing link between galaxies and quasars. Recent simulations of mergers and quasar evolution show that during much of the lifetime of the quasar, it is heavily shrouded by gas with large column densities (e.g., Hopkins et al., 2005). Observational support for this view comes from the discovery of a large number (four out of a sample of eight) LoBALs in high redshift quasars (Maiolino et al., 2004).

Thus, observational evidence and scenarios for quasar evolution imply that FeLoBALs may be candidates for support of the evolutionary scenario. If the quasar observable lifetime is assumed to be 10^7 years, the fact that FeLoBALs only make up 0.33% of quasars in the SDSS (Trump et al., 2006) implies that the time scale for this stage is approximately 3×10^4 years. That should be a lower limit, however, since these objects may be missed in the SDSS (Trump et al., 2006). This relatively short time period, compared with the total lifetime of a quasar, compares favorably with our crossing time of 15 years.

It is clear that a high global covering fraction is compatible with the evolutionary scenario. But what about the other parameters obtained from the model fits?. One possible problem is that the radius of the model shows that the outflow occurs well within the central engine, at approximately 1.4×10^{17} cm. The quasar feedback scenario proposed by Fabian (1999) infers that the bulk of the gas expelled from the AGN is accelerated beyond

the Bondi radius, which for a $5 \times 10^7\, M_\odot$ black hole is 4×10^{21} cm. On the other hand, the amount of gas expelled during this process could be comparable to the amount of gas contained by the entire galaxy, far more than the rather modest $547 M_\odot$ that we infer. It is quite possible that the accretion/blow out process is messy and chaotic; there may be a phase in which the central engine "burps", and this results in the features that we see.

3.6 Conclusions

Using the spectral synthesis code `PHOENIX` we compute synthetic spectra that provide very good fits to the observed restframe UV and optical spectra of two FeLoBALs. While our models are limited to exact spherical symmetry, they provide excellent fits. In order to reconcile our results with the polarization data on these objects, we require some asymmetry, but still a high global covering fraction, which would only modestly affect the flux spectrum.

We are able to determine a luminosity distance estimate which is direct and is accurate to around 50%. The question arises: could these objects be used as distance indicators at high z, even if only as a sanity check on the really high-z Hubble diagram from GRBs?

Our results lend support to the inference that FeLoBALs are an evolutionary stage of the QSO as opposed to a pure orientation effect. Our model with a smaller covering factor may be able to explain other BAL QSO such as overlapping trough QSOs. In addition our model column densities, which are Compton thick, match those that are expected from X-ray non-detections of these objects.

For future work we plan to explore metallicity effects on the model spectrum. This is not trivial, as it is not just a matter of changing the metallicity and comparing the model. Completely different sets of dynamical and luminosity parameters may be required to achieve the best fitting model spectrum. We plan to continue our analysis with the Hall

(2007) spectrum. We have compared our observed spectrum with the one from that paper and think that it is an excellent candidate for this type of modeling.

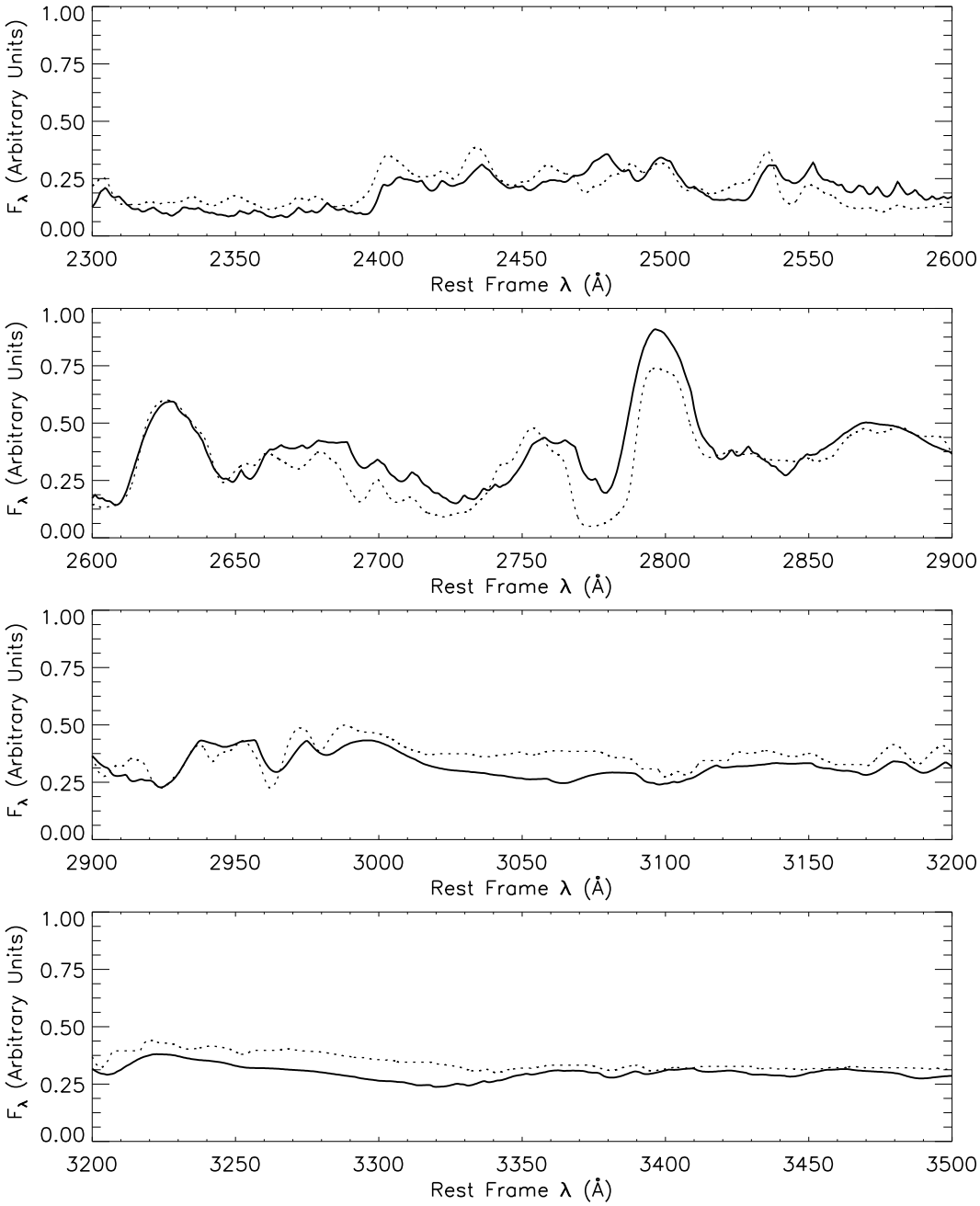

Figure 3.1 The PHOENIX spectrum (solid line) vs the restframe, dereddened, and smoothed, observed FIRST J121442.3+280329 (dotted line) UV spectrum.

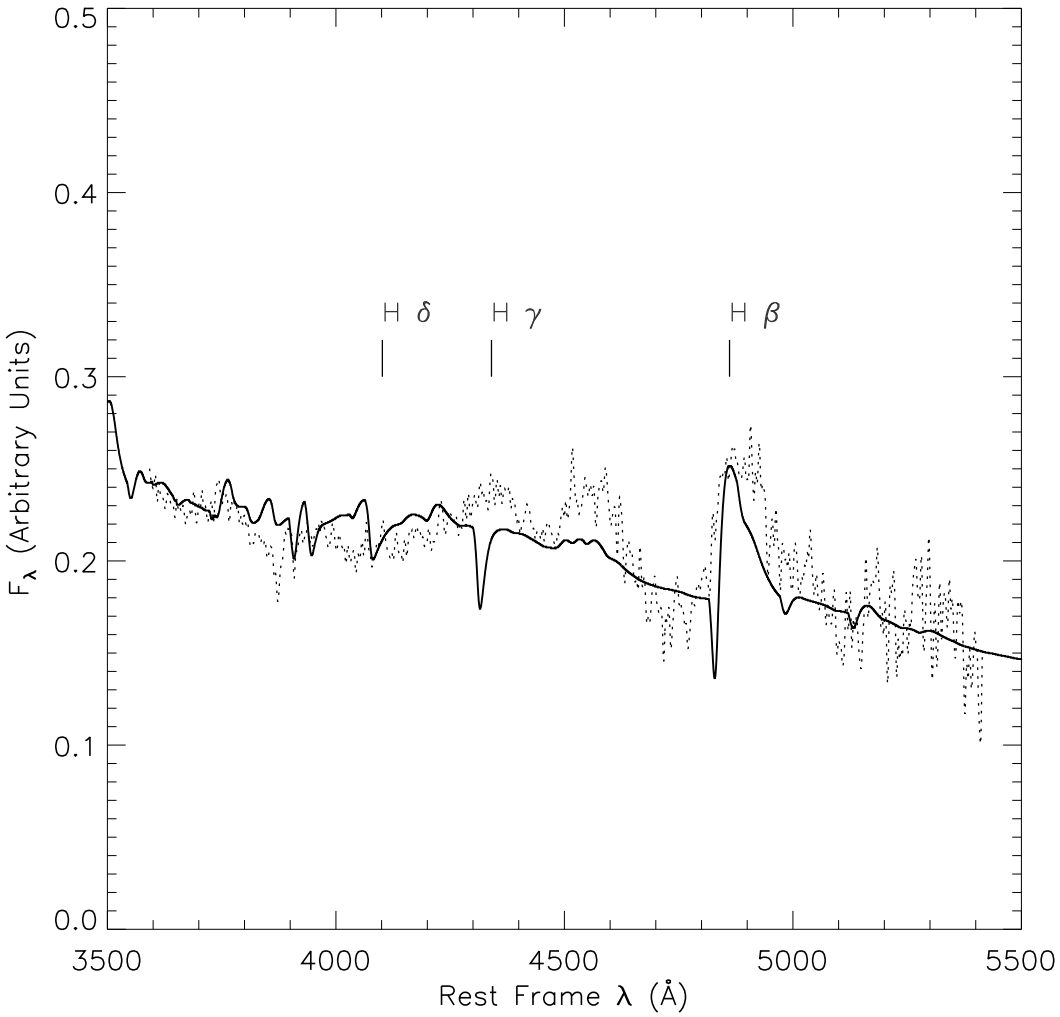

Figure 3.2 The PHOENIX model (solid line) vs the restframe, dereddened, and smoothed, observed optical spectrum of FIRST J121442.3+280329 (dotted line).

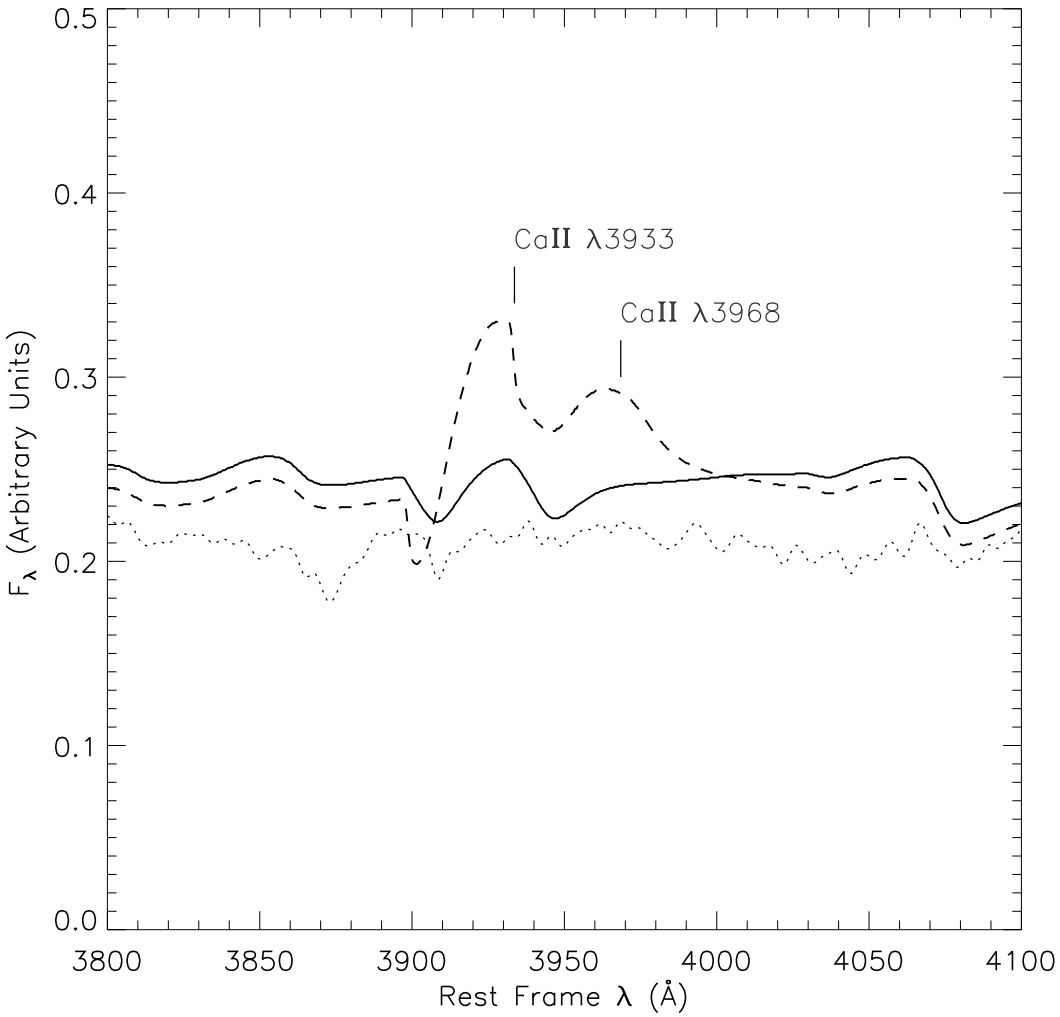

Figure 3.3 The optical spectrum of FIRST J121442.3+280329 (dotted) deredshifted, dereddened, and smoothed, versus two synthetic PHOENIX models. The dashed line represents a PHOENIX model with the ions discussed in §3.2 in NLTE except for the Calcium I-III ions, which are in LTE. The solid line shows a model with all of the ions in NLTE that are discussed in §3.2.

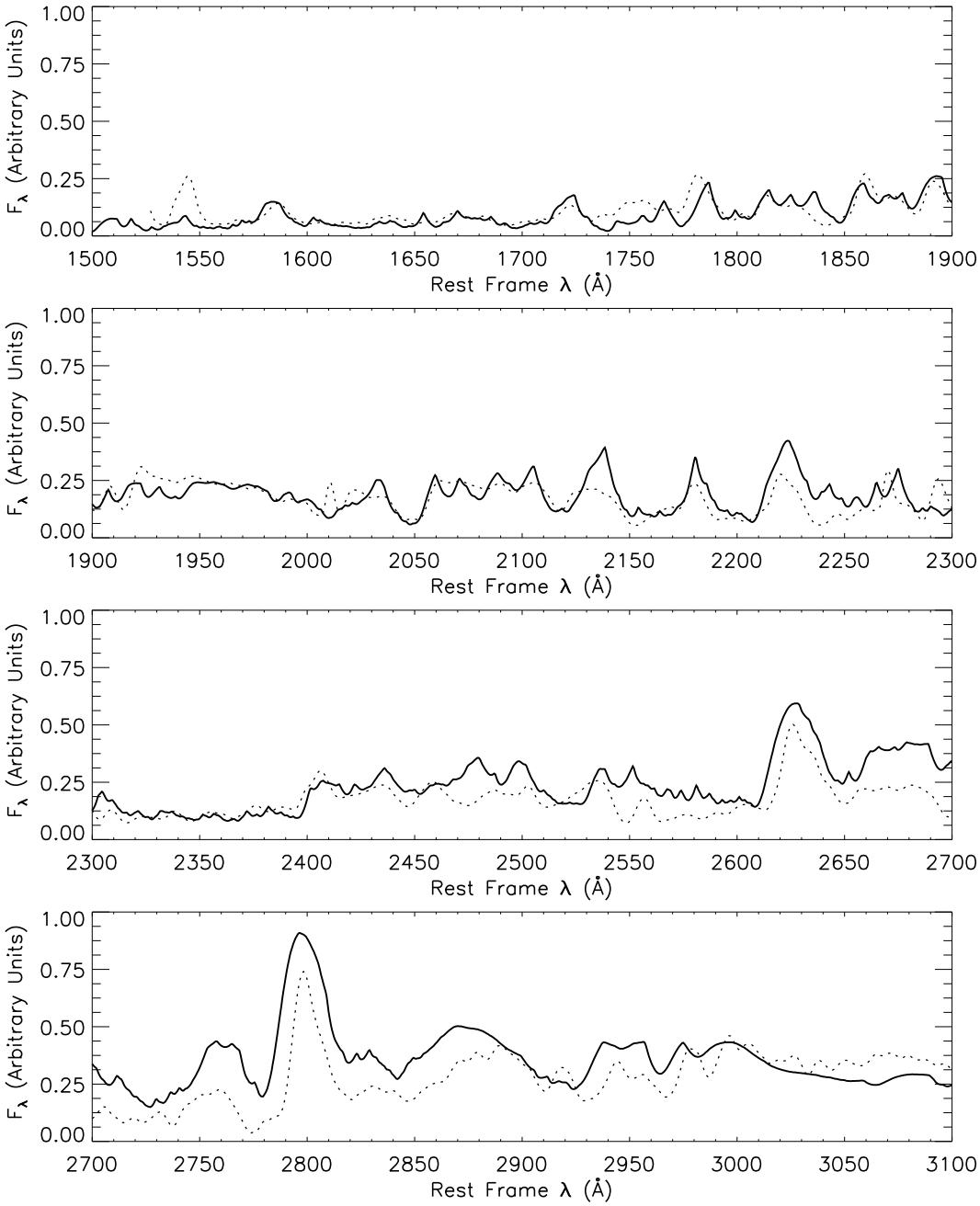

Figure 3.4 The PHOENIX model (solid line) vs the restframe, dereddened, and smoothed, UV spectrum of ISO J005645.1-273816 (dotted line).

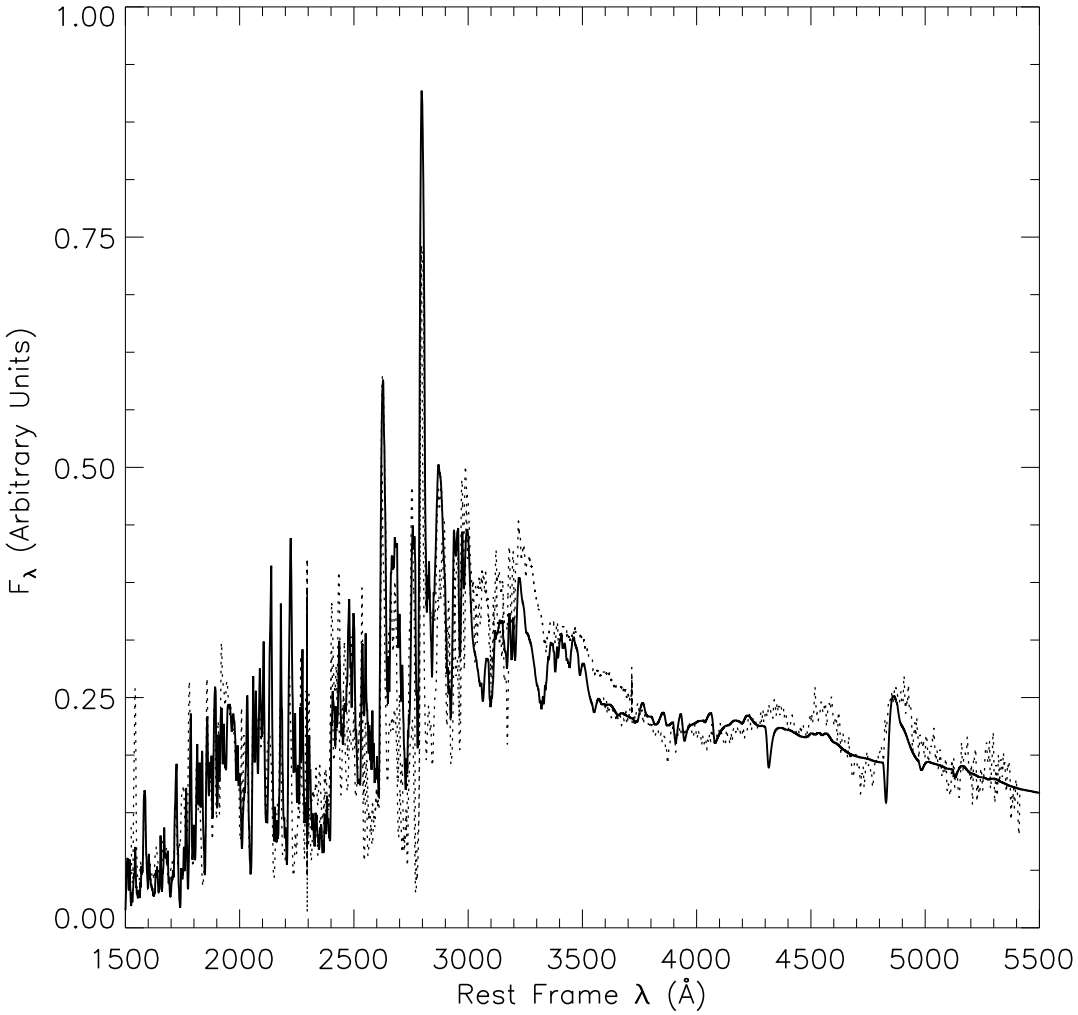

Figure 3.5 The combined spectra of FIRST J121442.3+280329 and ISO J005645.1-273816. The wavelength range spans 1500–5500Å. the `PHOENIX` spectrum is the solid line, while the FIRST J121442.3+280329 UV through optical spectrum and the ISO J005645.1-273816 UV spectrum are dotted. All spectra are restframe, deredshifted, and smoothed.

Chapter 4

Conclusions and Summary

Following is a summary of the results from each chapter and then a brief discussion of future work.

4.1 RE 1034+39

We conclude that, although RE 1034+39 has extreme O VI properties, they are consistent with trends appropriate for an object with its observed spectral energy distribution and luminosity. This suggests that neither the emission line region geometry nor the inclination angle is especially unusual in this object, but rather is an extension of those in other quasars.

4.2 FIRST J121442.3+280329 and ISO J005645.1-273816

With detailed synthetic modeling using `PHOENIX` we calculate synthetic models which are very good fits to one subtype of FeLoBAL. We are able to determine a luminosity distance estimate which is direct and is accurate to around 50%. The question arises: could these objects be used as distance indicators at high z, even if only as a sanity check on the really high-z Hubble diagram from GRBs? While our models are limited to exact spherical symmetry, they provide excellent fits. In order to reconcile our results with the polarization data on these objects we would require a jet, which would only modestly affect the flux spectrum. Our results lend support to the inference that FeLoBALs are an evolutionary stage of the QSO as opposed to a pure orientation effect. Our model with a smaller covering factor may be able to explain other BAL QSO such as overlapping trough QSOs. In addition

our model column densities, which are Compton thick, match those that are expected from X-ray non-detections of these objects.

In addition are currently developing code which would allow us to include a more AGN-like spectral energy distribution into our model. This future work may allow us even better understanding of energetics in AGN outflows as well as the FeLoBAL sub class.

4.3 Future Work

The work done in Chapter 2 is for the most part complete. The study of FeLoBAL AGN however is of future interest for me.

For future work we plan to explore metallicity effects on the model spectrum. This is not trivial, as it is not just a matter of changing the metallicity and comparing the model. Completely different sets of dynamical and luminosity parameters may be required to achieve the best fitting model spectrum.

Hall (2007) found that they see absorption features from the hydrogen balmer series in the optical spectrum of FeLoBAL QSOs. In addition they have a broad fit to their object from the UV to the optical. Our initial comparision to their object in Figure 4.1 looks promising, however we may be required to alter our assumption of solar metallicity due to the (possibly) weaker iron emission in this object. We plan to continue our analysis with the Hall (2007) spectrum. We have compared our bestfitting `PHOENIX` model spectrum from chapter 3. with the one from that paper (Fig. 4.1) and think that it is an excellent candidate for this type of modeling.

I am currently employed with Northrop Grumman at Tinker Air Force base located in Midwest City, Oklahoma.

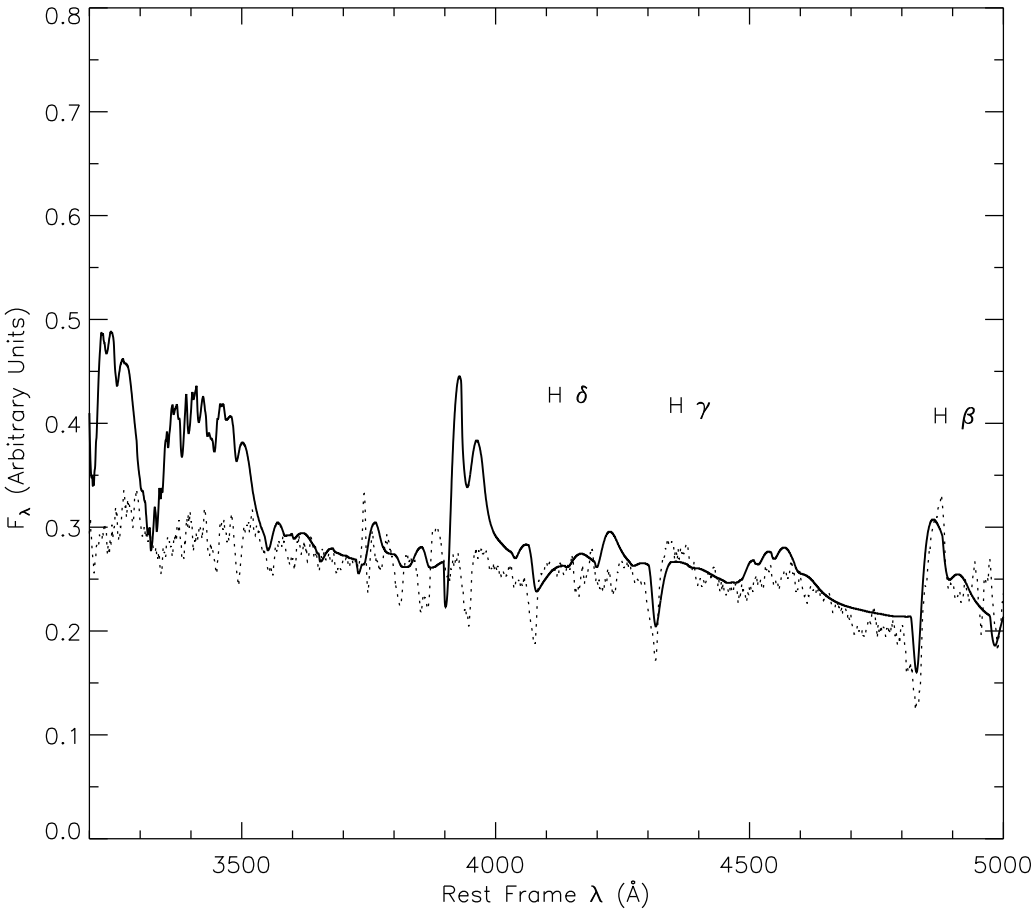

Figure 4.1 The PHOENIX model (solid line) vs the restframe, dereddened, and smoothed, optical spectrum of Hall (2007) (dotted line).

Bibliography

Allard, F., Hauschildt, P. H., Alexander, D. R., Tamanai, A., & Schweitzer, A. 2001, ApJ, 556, 357

Allard, F., Hauschildt, P. H., & Starrfield, S. 1997, Ann. Rev. Astr. Ap., 35, 137

Arav, N., Becker, R. H., Laurent-Muehleisen, S. A., Gregg, M. D., White, R. L., Brotherton, M. S., & de Kool, M. 1999, ApJ, 524, 566

Arav, N., de Kool, M., Korista, K. T., Crenshaw, D. M., van Breugel, W., Brotherton, M., Green, R. F., Pettini, M., Wills, B., de Vries, W., Becker, B., Brandt, W. N., Green, P., Junkkarinen, V. T., Koratkar, A., Laor, A., Laurent-Muehleisen, S. A., Mathur, S., & Murray, N. 2001, ApJ, 561, 118

Arav, N., Kaastra, J., Kriss, G. A., Korista, K. T., Gabel, J., & Proga, D. 2005, ApJ, 620, 665

Avrett, E. H. & Loeser, R. 1988, ApJ, 331, 211

Baade, W. 1926, Astr. Nach., 228, 359

Baldwin, J., Ferland, G., Korista, K., & Verner, D. 1995, ApJ, 455, L119+

Baldwin, J. A. 1997, in ASP Conf. Ser. 113: IAU Colloq. 159: Emission Lines in Active Galaxies: New Methods and Techniques, ed. B. M. Peterson, F.-Z. Cheng, & A. S. Wilson, 80–+

Baldwin, J. A., Ferland, G. J., Korista, K. T., Carswell, R. F., Hamann, F., Phillips, M. M., Verner, D., Wilkes, B. J., & Williams, R. E. 1996, ApJ, 461, 664

Baldwin, J. A., Wampler, E. J., Burbidge, E. M., Odell, S. L., Smith, H. E., Hazard, C., Nordsieck, K. H., Pooley, G., & Stein, W. A. 1977, ApJ, 215, 408

Baron, E., Bongard, S., Branch, D., & Hauschildt, P. 2006, ApJ, submitted

Baron, E., Branch, D., Hauschildt, P. H., Filippenko, A. V., & Kirshner, R. P. 1999, ApJ, 527, 739

Baron, E. & Hauschildt, P. H. 1998, ApJ, 495, 370

—. 2004, A&A, 427, 987

Baron, E., Hauschildt, P. H., Branch, D., Austin, S., Garnavich, P., Ann, H. B., Wagner, R. M., Filippenko, A. V., Matheson, T., & Liebert, J. 1995, ApJ, 441, 170

Baron, E., Hauschildt, P. H., & Lowenthal, D. 2003, in Stellar Atmospheric Modeling, ed. I. Hubeny, D. Mihalas, & K. Werner (San Francisco: ASP), 385

Baron, E., Hauschildt, P. H., & Mezzacappa, A. 1997, in Thermonuclear Supernovae, ed. P. Ruiz-Lapuente, R. Canal, & J. Isern (Dordrecht: Kluwer), 627

Baron, E., Nugent, P., Branch, D., & Hauschildt, P. 2004, ApJ, 616, 91

Baron, E. et al. 2000, ApJ, 545, 444

Baschek, B., Scholz, M., & Wehrse, R. 1991, A&A, 299, 374

Bechtold, J., Siemiginowska, A., Shields, J., Czerny, B., Janiuk, A., Hamann, F., Aldcroft, T. L., Elvis, M., & Dobrzycki, A. 2003, ApJ, 588, 119

Becker, R. H., Gregg, M. D., Hook, I. M., McMahon, R. G., White, R. L., & Helfand, D. J. 1997, ApJ, 479, L93+

Becker, R. H., White, R. L., Gregg, M. D., Brotherton, M. S., Laurent-Muehleisen, S. A., & Arav, N. 2000a, ApJ, 538, 72

—. 2000b, ApJ, 538, 72

Begelman, M. C. 2003, Science, 300, 1898

Boroson, T. A. & Green, R. F. 1992, ApJS, 80, 109

Boroson, T. A. & Meyers, K. A. 1992, ApJ, 397, 442

Bottorff, M., Ferland, G., Baldwin, J., & Korista, K. 2000, ApJ, 542, 644

Branch, D., Baron, E., & Jeffery, D. 2003, in Supernovae and Gamma-Ray Bursts, ed. K. W. Weiler (New York: Springer-Verlag), 47

Branch, D., Leighly, K. M., Thomas, R. C., & Baron, E. 2002, ApJ, 578, L37

Brandt, W. N. & Boller, T. 1999, in ASP Conf. Ser. 175: Structure and Kinematics of Quasar Broad Line Regions, ed. C. M. Gaskell, W. N. Brandt, M. Dietrich, D. Dultzin-Hacyan, & M. Eracleous, 265–+

Brotherton, M. S., De Breuck, C., & Schaefer, J. J. 2006, ArXiv Astrophysics e-prints

Brotherton, M. S., Green, R. F., Kriss, G. A., Oegerle, W., Kaiser, M. E., Zheng, W., & Hutchings, J. B. 2002, ApJ, 565, 800

Brotherton, M. S., Tran, H. D., Becker, R. H., Gregg, M. D., Laurent-Muehleisen, S. A., & White, R. L. 2001, ApJ, 546, 775

Cardelli, J. A., Clayton, G. C., & Mathis, J. S. 1989, ApJ, 345, 245

Casebeer, D., Baron, E., Branch, D., & Leighly, K. 2004, in AGN Physics with the Sloan Digital Sky Survey, ed. G. T. Richards & P. B. Hall, ASP Conference Series (San Franciso: ASP), 231

Casebeer, D., Baron, E., Leighly, K., Jevremovic, D., & Branch, D. 2007, ApJ submitted

Casebeer, D. A., Leighly, K. M., & Baron, E. 2006, ApJ, 637, 157

Collin-Souffrin, S., Dumont, S., & Tully, J. 1982, A&A, 106, 362

Collin-Souffrin, S., Dyson, J. E., McDowell, J. C., & Perry, J. J. 1988, MNRAS, 232, 539

Cowie, L. L., Songaila, A., Hu, E. M., Egami, E., Huang, J.-S., Pickles, A. J., Ridgway, S. E., Wainscoat, R. J., & Weymann, R. J. 1994, ApJ, 432, L83

Davidson, K. & Netzer, H. 1979, Reviews of Modern Physics, 51, 715

de Kool, M., Arav, N., Becker, R. H., Gregg, M. D., White, R. L., Laurent-Muehleisen, S. A., Price, T., & Korista, K. T. 2001, ApJ, 548, 609

de Kool, M., Becker, R. H., Gregg, M. D., White, R. L., & Arav, N. 2002, ApJ, 567, 58

Dietrich, M., Hamann, F., Shields, J. C., Constantin, A., Vestergaard, M., Chaffee, F., Foltz, C. B., & Junkkarinen, V. T. 2002, ApJ, 581, 912

Duc, P.-A. et al. 2002, A&A, 389, L47

Dumont, A.-M., Collin, S., Paletou, F., Coupé, S., Godet, O., & Pelat, D. 2003, A&A, 407, 13

Egami, E. 1999, in IAU Symp. 186: Galaxy Interactions at Low and High Redshift, ed. J. E. Barnes & D. B. Sanders, 475–+

Elvis, M., Wilkes, B. J., McDowell, J. C., Green, R. F., Bechtold, J., Willner, S. P., Oey, M. S., Polomski, E., & Cutri, R. 1994, ApJS, 95, 1

Eracleous, M. & Halpern, J. P. 2004, ApJS, 150, 181

Eracleous, M., Halpern, J. P., & Charlton, J. C. 2003, ApJ, 582, 633

Espey, B. & Andreadis, S. 1999, in ASP Conf. Ser. 162: Quasars and Cosmology, ed. G. Ferland & J. Bladwin, 351–+

Fabian, A. C. 1999, MNRAS, 308, L39

Ferland, G. J. 2000a, in Revista Mexicana de Astronomia y Astrofisica Conference Series, Vol. 9, Revista Mexicana de Astronomia y Astrofisica Conference Series, ed. S. J. Arthur, N. S. Brickhouse, & J. Franco, 153–157

Ferland, G. J. 2000b, Hazy, A Brief Introduction to Cloudy 94 (University of Kentucky Internal Report, 565 pages)

Ferland, G. J., Korista, K. T., Verner, D. A., Ferguson, J. W., Kingdon, J. B., & Verner, E. M. 1998, PASP, 110, 761

Ferrarese, L. & Merritt, D. 2000, ApJ, 539, L9

Fisher, A. 2000, PhD thesis, Univ. of Oklahoma, unpublished

Francis, P. J., Hewett, P. C., Foltz, C. B., Chaffee, F. H., Weymann, R. J., & Morris, S. L. 1991a, ApJ, 373, 465

—. 1991b, ApJ, 373, 465

Frank, J., King, A., & Raine, D. J. 2002, Accretion Power in Astrophysics: Third Edition (Accretion Power in Astrophysics, by Juhan Frank and Andrew King and Derek Raine, pp. 398. ISBN 0521620538. Cambridge, UK: Cambridge University Press, February 2002.)

Gabel, J. R., Arav, N., & Kim, T.-S. 2006, ApJ, 646, 742

Gallagher, S. C., Brandt, W. N., Chartas, G., & Garmire, G. P. 2002, ApJ, 567, 37

Gallagher, S. C., Brandt, W. N., Chartas, G., Priddey, R., Garmire, G. P., & Sambruna, R. M. 2006, ApJ, 644, 709

Gebhardt, K. et al. 2000, ApJ, 543, L5

Graham, M. J., Clowes, R. G., & Campusano, L. E. 1996, MNRAS, 279, 1349

Green, P. J. 1996, ApJ, 467, 61

—. 1998, ApJ, 498, 170

Green, P. J., Aldcroft, T. L., Mathur, S., Wilkes, B. J., & Elvis, M. 2001a, ApJ, 558, 109

Green, P. J., Forster, K., & Kuraszkiewicz, J. 2001b, ApJ, 556, 727

Gregg, M. D., Becker, R. H., & de Vries, W. 2006, ApJ, 641, 210

Grevesse, N. & Noels. 1993, in Abundances, ed. C. Jaschek & M. Jaschek (Dordrecht: Kluwer), 111

Grupe, D., Beuermann, K., Thomas, H.-C., Mannheim, K., & Fink, H. H. 1998, A&A, 330, 25

Hall, P. B. 2007, AJ, 133, 1271

Hall, P. B. et al. 2002, ApJS, 141, 267

Halpern, J. P., Leighly, K. M., & Marshall, H. L. 2003, ApJ, 585, 665

Hamann, F. 1998, ApJ, 500, 798

Hamann, F., Cohen, R. D., Shields, J. C., Burbidge, E. M., Junkkarinen, V., & Crenshaw, D. M. 1998, ApJ, 496, 761

Hamann, F., Korista, K. T., Ferland, G. J., Warner, C., & Baldwin, J. 2002, ApJ, 564, 592

Hauschildt, P. H. 1992, JQSRT, 47, 433

Hauschildt, P. H. & Baron, E. 1995, JQSRT, 54, 987

—. 1999, J. Comp. Applied Math., 109, 41

—. 2004a, A&A, 417, 317

—. 2004b, Mitteilungen der Mathematischen Gesellschaft in Hamburg, 24, 1

Hauschildt, P. H. & Baron, E. 2006, A&A, 451, 273

Hauschildt, P. H., Baron, E., & Allard, F. 1997a, ApJ, 483, 390

Hauschildt, P. H., Lowenthal, D. K., & Baron, E. 2001, ApJS, 134, 323

Hauschildt, P. H., Schwarz, G., Baron, E., Starrfield, S., Shore, S., & Allard, F. 1997b, ApJ, 490, 803

Hazard, C., McMahon, R. G., Webb, J. K., & Morton, D. C. 1987, ApJ, 323, 263

Hazard, C., Morton, D. C., Terlevich, R., & McMahon, R. 1984, ApJ, 282, 33

Ho, L. C. 2003, in ASP Conf. Ser. 290: Active Galactic Nuclei: From Central Engine to Host Galaxy, ed. S. Collin, F. Combes, & I. Shlosman, 379–+

Hopkins, P. F., Hernquist, L., Martini, P., Cox, T. J., Robertson, B., Di Matteo, T., & Springel, V. 2005, ApJ, 625, L71

Kaspi, S., Smith, P. S., Netzer, H., Maoz, D., Jannuzi, B. T., & Giveon, U. 2000, ApJ, 533, 631

Korista, K., Baldwin, J., & Ferland, G. 1998, ApJ, 507, 24

Korista, K., Baldwin, J., Ferland, G., & Verner, D. 1997a, ApJS, 108, 401

Korista, K., Ferland, G., & Baldwin, J. 1997b, ApJ, 487, 555

Korista, K. T., Weymann, R. J., Morris, S. L., Kopko, M. J., Turnshek, D. A., Hartig, G. F., Foltz, C. B., Burbidge, E. M., & Junkkarinen, V. T. 1992, ApJ, 401, 529

Kriss, G. 1994, in ASP Conf. Ser. 61: Astronomical Data Analysis Software and Systems III, ed. D. R. Crabtree, R. J. Hanisch, & J. Barnes, 437–+

Kriss, G. A. 2001, in ASP Conf. Ser. 224: Probing the Physics of Active Galactic Nuclei, ed. B. M. Peterson, R. W. Pogge, & R. S. Polidan, 45–+

Krolik, J. H. & Kallman, T. R. 1988, ApJ, 324, 714

Kuraszkiewicz, J., Wilkes, B. J., Czerny, B., & Mathur, S. 2000, ApJ, 542, 692

Kwan, J. & Krolik, J. H. 1981, ApJ, 250, 478

Lamy, H. & Hutsemékers, D. 2000, A&A, 356, L9

—. 2004, A&A, 427, 107

Laor, A. & Netzer, H. 1989, MNRAS, 238, 897

Leighly, K., Halpern, J., & Jenkins, E. 2004, in ASP Conf. Ser. 311: AGN Physics with the Sloan Digital Sky Survey, ed. G. T. Richards & P. B. Hall, 277–+

Leighly, K. M. 1999, ApJS, 125, 317

—. 2004a, ApJ, 611, 125

—. 2004b, ApJ, 611, 125

Leighly, K. M. & Casebeer, D. 2007, ArXiv Astrophysics e-prints

Leighly, K. M., Halpern, J. P., Helfand, D. J., Becker, R. H., & Impey, C. D. 2001, AJ, 121, 2889

Leighly, K. M. & Moore, J. R. 2004, ApJ, 611, 107

—. 2006, ApJ, 644, 748

Lentz, E., Baron, E., Branch, D., & Hauschildt, P. H. 2001a, ApJ, 557, 266

—. 2001b, ApJ, 547, 402

Lentz, E. et al. 2001c, ApJ, 547, 406

Magorrian, J. et al. 1998, AJ, 115, 2285

Maiolino, R., Oliva, E., Ghinassi, F., Pedani, M., Mannucci, F., Mujica, R., & Juarez, Y. 2004, A&A, 420, 889

Mathews, W. G. & Ferland, G. J. 1987, ApJ, 323, 456

Mitchell, R., Baron, E., Branch, D., Hauschildt, P. H., Nugent, P., Lundqvist, P., Blinnikov, S., & Pun, C. S. J. 2002, ApJ, 574, 293

Mitchell, R., Baron, E., Branch, D., Lundqvist, P., Blinnikov, S., Hauschildt, P. H., & Pun, C. S. J. 2001, ApJ, 556, 979

Moos, H. W., Cash, W. C., Cowie, L. L., Davidsen, A. F., Dupree, A. K., Feldman, P. D., Friedman, S. D., Green, J. C., Green, R. F., Gry, C., Hutchings, J. B., Jenkins, E. B., Linsky, J. L., Malina, R. F., Michalitsianos, A. G., Savage, B. D., Shull, J. M., Siegmund, O. H. W., Snow, T. P., Sonneborn, G., Vidal-Madjar, A., Willis, A. J., Woodgate, B. E., York, D. G., Ake, T. B., Andersson, B.-G., Andrews, J. P., Barkhouser, R. H., Bianchi, L., Blair, W. P., Brownsberger, K. R., Cha, A. N., Chayer, P., Conard, S. J., Fullerton, A. W., Gaines, G. A., Grange, R., Gummin, M. A., Hebrard, G., Kriss, G. A., Kruk, J. W., Mark, D., McCarthy, D. K., Morbey, C. L., Murowinski, R., Murphy, E. M., Oegerle, W. R., Ohl, R. G., Oliveira, C., Osterman, S. N., Sahnow, D. J., Saisse, M., Sembach, K. R., Weaver, H. A., Welsh, B. Y., Wilkinson, E., & Zheng, W. 2000, ApJ, 538, L1

Murray, N., Chiang, J., Grossman, S. A., & Voit, G. M. 1995, ApJ, 451, 498

Mushotzky, R. & Ferland, G. J. 1984, ApJ, 278, 558

Narayanan, D., Hamann, F., Barlow, T., Burbidge, E. M., Cohen, R. D., Junkkarinen, V., & Lyons, R. 2004, ApJ, 601, 715

Natali, F., Giallongo, E., Cristiani, S., & La Franca, F. 1998, AJ, 115, 397

Nugent, P., Baron, E., Branch, D., Fisher, A., & Hauschildt, P. 1997, ApJ, 485, 812

Nussbaumer, H. & Storey, P. J. 1982, A&A, 115, 205

O'Donnell, J. E. 1994, ApJ, 422, 158

Osmer, P. S., Porter, A. C., & Green, R. F. 1994, ApJ, 436, 678

Osmer, P. S. & Shields, J. C. 1999, in ASP Conf. Ser. 162: Quasars and Cosmology, ed. G. Ferland & J. Baldwin, 235–+

Osterbrock, D. E. 1989, Astrophysics of gaseous nebulae and active galactic nuclei (Research supported by the University of California, John Simon Guggenheim Memorial Foundation, University of Minnesota, et al. Mill Valley, CA, University Science Books, 1989, 422 p.)

Peterson, B. M. 1997, An Introduction to Active Galactic Nuclei (An introduction to active galactic nuclei, Publisher: Cambridge, New York Cambridge University Press, 1997 Physical description xvi, 238 p. ISBN 0521473489)

Petz, A., Hauschildt, P. H., Ness, J.-U., & Starrfield, S. 2005, A&A, 431, 321

Pounds, K. A., Done, C., & Osborne, J. P. 1995, MNRAS, 277, L5

Proga, D. & Kallman, T. R. 2004, ApJ, 616, 688

Proga, D., Stone, J. M., & Kallman, T. R. 2000, ApJ, 543, 686

Puchnarewicz, E. M., Mason, K. O., & Siemiginowska, A. 1998, MNRAS, 293, L52

Puchnarewicz, E. M., Mason, K. O., Siemiginowska, A., Fruscione, A., Comastri, A., Fiore, F., & Cagnoni, I. 2001, ApJ, 550, 644

Puchnarewicz, E. M., Mason, K. O., Siemiginowska, A., & Pounds, K. A. 1995, MNRAS, 276, 20

Reichard, T. A., Richards, G. T., Hall, P. B., Schneider, D. P., Vanden Berk, D. E., Fan, X., York, D. G., Knapp, G. R., & Brinkmann, J. 2003, AJ, 126, 2594

Romano, P., Mathur, S., Pogge, R. W., Peterson, B. M., & Kuraszkiewicz, J. 2002, ApJ, 578, 64

Ross, R. R., Fabian, A. C., & Mineshige, S. 1992, MNRAS, 258, 189

Różańska, A. & Czerny, B. 2000a, MNRAS, 316, 473

—. 2000b, A&A, 360, 1170

Rybicki, G. B. & Hummer, D. G. 1991, A&A, 245, 171

Sahnow, D. J., Moos, H. W., Ake, T. B., Andersen, J., Andersson, B.-G., Andre, M., Artis, D., Berman, A. F., Blair, W. P., Brownsberger, K. R., Calvani, H. M., Chayer, P., Conard, S. J., Feldman, P. D., Friedman, S. D., Fullerton, A. W., Gaines, G. A., Gawne, W. C., Green, J. C., Gummin, M. A., Jennings, T. B., Joyce, J. B., Kaiser, M. E., Kruk, J. W., Lindler, D. J., Massa, D., Murphy, E. M., Oegerle, W. R., Ohl, R. G., Roberts, B. A., Romelfanger, M. L., Roth, K. C., Sankrit, R., Sembach, K. R., Shelton, R. L., Siegmund, O. H. W., Silva, C. J., Sonneborn, G., Vaclavik, S. R., Weaver, H. A., & Wilkinson, E. 2000, ApJ, 538, L7

Schlegel, D. J., Finkbeiner, D. P., & Davis, M. 1998a, ApJ, 500, 525

—. 1998b, ApJ, 500, 525

Scott, J. E., Kriss, G. A., Brotherton, M., Green, R. F., Hutchings, J., Shull, J. M., & Zheng, W. 2004, ApJ, 615, 135

Shakura, N. I. & Sunyaev, R. A. 1973, A&A, 24, 337

Shang, Z., Brotherton, M. S., Green, R. F., Kriss, G. A., Scott, J., Quijano, J. K., Blaes, O., Hubeny, I., Hutchings, J., Kaiser, M. E., Koratkar, A., Oegerle, W., & Zheng, W. 2005, ApJ, 619, 41

Shang, Z., Wills, B. J., Robinson, E. L., Wills, D., Laor, A., Xie, B., & Yuan, J. 2003, ApJ, 586, 52

Short, C. I., Hauschildt, P. H., & Baron, E. 1999, ApJ, 525, 375

Shull, J. M., Tumlinson, J., Giroux, M. L., Kriss, G. A., & Reimers, D. 2004, ApJ, 600, 570

Sigut, T. A. A. & Pradhan, A. K. 2003, ApJS, 145, 15

Sigut, T. A. A., Pradhan, A. K., & Nahar, S. N. 2004, ApJ, 611, 81

Soria, R. & Puchnarewicz, E. M. 2002, MNRAS, 329, 456

Svensson, R. & Zdziarski, A. A. 1994, ApJ, 436, 599

Trump, J. R. et al. 2006, ApJS, 165, 1

Verner, E., Bruhwheiler, F., Tsuzuki, Y., Kawara, K., Yoshii, Y., & Oyabu, S. 2003, in Bulletin of the American Astronomical Society, Vol. 35, Bulletin of the American Astronomical Society, 1327–+

Vignali, C., Brandt, W. N., Schneider, D. P., Anderson, S. F., Fan, X., Gunn, J. E., Kaspi, S., Richards, G. T., & Strauss, M. A. 2003, AJ, 125, 2876

Voit, G. M., Weymann, R. J., & Korista, K. T. 1993, ApJ, 413, 95

Walborn, N. R., Lennon, D. J., Haser, S. M., Kudritzki, R.-P., & Voels, S. A. 1995, PASP, 107, 104

Walter, R., Orr, A., Courvoisier, T. J.-L., Fink, H. H., Makino, F., Otani, C., & Wamsteker, W. 1994, A&A, 285, 119

Wandel, A. & Boller, T. 1998, A&A, 331, 884

Wang, T.-G., Lu, Y.-J., & Zhou, Y.-Y. 1998, ApJ, 493, 1

Warner, C., Hamann, F., & Dietrich, M. 2004, ApJ, 608, 136

Weymann, R. J., Morris, S. L., Foltz, C. B., & Hewett, P. C. 1991, ApJ, 373, 23

White, R. L., Helfand, D. J., Becker, R. H., Gregg, M. D., Postman, M., Lauer, T. R., & Oegerle, W. 2003, AJ, 126, 706

Wilkes, B. J., Kuraszkiewicz, J., Green, P. J., Mathur, S., & McDowell, J. C. 1999, ApJ, 513, 76

Wilkes, B. J., Tananbaum, H., Worrall, D. M., Avni, Y., Oey, M. S., & Flanagan, J. 1994, ApJS, 92, 53

Wills, B. J., Laor, A., Brotherton, M. S., Wills, D., Wilkes, B. J., Ferland, G. J., & Shang, Z. 1999, ApJ, 515, L53

Wills, B. J., Netzer, H., & Wills, D. 1985, ApJ, 288, 94

Yaqoob, T., Ebisawa, K., Gendreau, K., & Mukai, K. 2000, in Bulletin of the American Astronomical Society, 1227–+

Zdziarski, A. A. & Gierliński, M. 2004, Progress of Theoretical Physics Supplement, 155, 99

Zdziarski, A. A., Poutanen, J., & Johnson, W. N. 2000, ApJ, 542, 703

Zheng, W., Kriss, G. A., & Davidsen, A. F. 1995, ApJ, 440, 606

Zheng, W., Kriss, G. A., Telfer, R. C., Grimes, J. P., & Davidsen, A. F. 1997, ApJ, 475, 469

Appendix A

PHOENIX

A.1 The PHOENIX Code

PHOENIX is a mature code. Development of PHOENIX began in the early 1990s and continues today. Discussions of the computational details appear in a number of publications. But since AGN astronomers are not familiar with PHOENIX, we include a short description of some of the computational details for those who are interested in understanding in more detail how the code works. This section also included relevant references. Finally, we present a flowchart of a PHOENIX computation.

A.1.1 An introduction to PHOENIX

PHOENIX is able to model astrophysical plasmas under a variety of conditions, including differential expansion at relativistic velocities (Hauschildt & Baron, 2006; Hauschildt & Baron, 2004a; Baron & Hauschildt, 2004; Hauschildt & Baron, 1999; Hauschildt et al., 1997a,b; Allard et al., 1997). PHOENIX includes very detailed model atoms constructed from the work of Kurucz (Hauschildt & Baron, 1995; Baron et al., 1997; Short et al., 1999) for a number of almost all the important species (H, He, CNO, Si, Fe, Co, etc.). In addition, the CHIANTI or APED databases may be chosen for model atoms at runtime. The code is optimized and parallelized to run on all available supercomputers. PHOENIX has a long history of modeling astrophysical objects including extra-solar giant planets (EGPs), Brown dwarfs (Allard et al., 1997, 2001), novae (Petz et al., 2005), as well as all types of supernovae (Baron et al., 1995, 1999; Nugent et al., 1997; Baron et al., 2000; Lentz et al., 2001a,b,c;

Mitchell et al., 2001; Baron et al., 2006). In the current version 14, we solve the fully relativistic radiative transport equation for a variety of spatial boundary conditions in both spherical and plane-parallel geometries for both continuum and line radiation simultaneously and self-consistently using an operator splitting technique. We also use an operator splitting technique to solve the full multi-level NLTE transfer and rate equations for a large number of atomic species (with a total of more than 10,000 energy levels and more than 100,000 primary NLTE lines), including non-thermal processes. MPI and OpenMP directives are used, so the code runs on both distributed and shared memory architectures (Baron et al., 2003; Hauschildt et al., 2001; Baron & Hauschildt, 1998; Hauschildt et al., 1997a). `PHOENIX` accurately solves the fully relativistic radiation transport equation along with the non-LTE rate equations (currently for ~ 150 ions) while ensuring radiative equilibrium (energy conservation). Typically each atom has several ionic species in NLTE and is represented by dozens to hundreds of levels for the Fe-group species. `PHOENIX` is currently around 700,000 lines of code which relies on 0.6 GB of atomic data and 12 GB of molecular data.

In the present paper, the multilevel, non-LTE rate equations are solved self-consistently for H I, He I–II, Mg I–III, Ca I-III, and Fe I–III using an accelerated lambda iteration (ALI) method (Rybicki & Hummer, 1991; Hauschildt, 1992; Hauschildt & Baron, 1999, 2004b). Simultaneously we solve for the special relativistic condition of radiative equilibrium (Nugent et al., 1997) using a modified Unsöld-Lucy temperature correction scheme. Relativistic effects, in particular the effects of advection and aberration, are important in the high velocity flows observed in these quasars.

The generalized non-LTE equation of state (EOS) is solved for 40 elements and up to 26 ionization stages per element for a total of hundreds of species. For the conditions present in the models, molecules are unimportant, and we neglect them in order reap substantial

savings in CPU time. Negative ions are always included. The numerical solution of the EOS is based on Brent's method for the solution of nonlinear equations which is very robust and fast.

In addition to the non-LTE lines, the models include, self-consistently, line blanketing of the most important ($\approx 10^6$) lines selected from the latest atomic and ionic line list of Kurucz. The entire list contains close to 42 million lines but not all of them are important for the case at hand. Therefore, before every temperature iteration, a smaller list is formed from the original list. A set of optical depths in the line-forming region of the gas is chosen, then using the density and temperature for these depths, the absorption coefficient in the line center, κ_l, is calculated for every line and compared to the corresponding continuum (LTE+NLTE) absorption coefficient, κ_c. A line is transferred to the "small list" if the ratio κ_l/κ_c is larger than a pre-specified value (in these calculations 5×10^{-6}, selecting over half a million lines). In the subsequent radiative transfer calculations all lines selected in this way are taken into account as individual lines and all others from the large line list are neglected. This selection procedure is repeated at each iteration where the pressure or temperature changes by a prescribed amount in order to always include the most important lines. We treat line scattering in these LTE lines by setting the albedo for single scattering, $\alpha = 0.95$.

A.1.2 A PHOENIX Flowchart

This section gives the reader a brief explanation of how the PHOENIX code computes a model spectrum. For a more complete understanding the authors recommend the reader peruse Hauschildt & Baron (1999). Our iteration scheme for the solution of the multi-level non-LTE problem can be summarized as follows: (1) for given population levels [n_i] and electron densities [n_e], solve the radiative transfer equation at each wavelength point and update the

radiative rates and the approximate rate operator, (2) solve the linear system for the atomic level populations for a given electron density, (3) compute new electron densities (by either fixed point iteration or the generalized partition function method), (4) if the electron density has not converged to the prescribed accuracy $\delta n_e/n_e < \epsilon$, go back to step 2, otherwise go to step 1. The iterations are repeated until a prescribed accuracy for the n_e and the n_i is reached $\Delta n_e/n_e < \epsilon$. It is important to account for coherent scattering processes during the solution of the wavelength-dependent radiative transfer equation, it explicitly removes a global coupling from the iterations.

As the first step in our outermost iteration loop (the model iteration) we use the current best guess of [T, n_i] as function of radius to solve the hydrostatic or hydrodynamic equations to calculate an improved run of P_{gas} with radius. Simultaneously, the population numbers are updated to account for changes in P_{gas}. The next major step is the computation of the radiation field for each wavelength point (the wavelength loop), which has the prerequisite of a spectral line selection procedure for LTE background lines. Immediately after the radiation field at any given wavelength is known, the radiative rates and the rate operators are updated so that their calculation is finished after the last wavelength point. In the next steps, the population numbers are updated by solving the rate equations for each NLTE species and new electron densities are computed; this gives improved estimates for [n_i]. The last part of the model iteration is the temperature correction scheme outlined above (using opacity averages etc., that were computed in the wavelength loop) which delivers an improved temperature structure. If the errors in the constraint equations are larger than a prescribed accuracy, the improved [T, n_i] are used in another model iteration. Using this scheme, about 10–20 model iterations are typically required to reach convergence to better than about 1% relative errors, depending on the quality of the initial guess of the

independent variables and the complexity of the model.

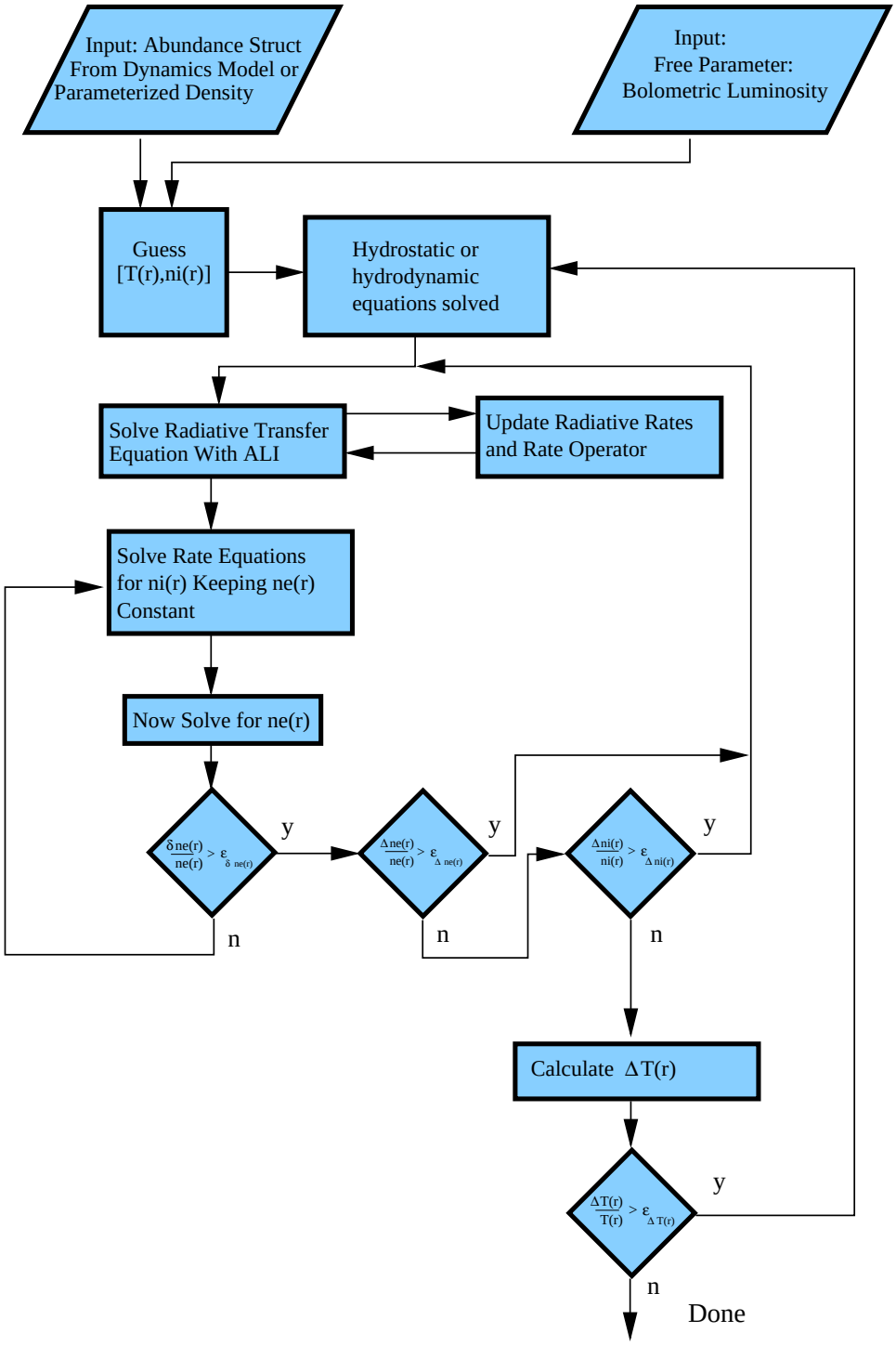

Figure A.1 Flowchart for a global iteration of PHOENIX.